AFRL-AFOSR-VA-TR-2015-0383

Determining energy distributions of HF-accelerated electrons at HAARP

Christopher Fallen
University of Alaska Fairbanks

11/18/2015
Final Report

DISTRIBUTION A: Distribution approved for public release.

Air Force Research Laboratory
AF Office Of Scientific Research (AFOSR)/ RTB1
Arlington, Virginia 22203
Air Force Materiel Command

REPORT DOCUMENTATION PAGE

Form Approved
OMB No. 0704-0188

The public reporting burden for this collection of information is estimated to average 1 hour per response, including the time for reviewing instructions, searching existing data sources, gathering and maintaining the data needed, and completing and reviewing the collection of information. Send comments regarding this burden estimate or any other aspect of this collection of information, including suggestions for reducing the burden, to the Department of Defense, Executive Service Directorate (0704-0188). Respondents should be aware that notwithstanding any other provision of law, no person shall be subject to any penalty for failing to comply with a collection of information if it does not display a currently valid OMB control number.

PLEASE DO NOT RETURN YOUR FORM TO THE ABOVE ORGANIZATION.

1. REPORT DATE *(DD-MM-YYYY)*
13-11-2015

2. REPORT TYPE
Final Performance Report

3. DATES COVERED *(From - To)*
8/15/2012 - 11/14/2015

4. TITLE AND SUBTITLE
Determining energy distributions of HF-accelerated electrons at HAARP

5a. CONTRACT NUMBER
FA9550-12-1-0424

5b. GRANT NUMBER

5c. PROGRAM ELEMENT NUMBER

6. AUTHOR(S)
Fallen, Christopher, T

5d. PROJECT NUMBER

5e. TASK NUMBER

5f. WORK UNIT NUMBER

7. PERFORMING ORGANIZATION NAME(S) AND ADDRESS(ES)
University of Alaska Fairbanks
909 Koyukuk Drive, 008 WRRB, PO Box 757880,
Fairbanks, AK 99775-7880
(907) 474-7301

8. PERFORMING ORGANIZATION REPORT NUMBER
N/A

9. SPONSORING/MONITORING AGENCY NAME(S) AND ADDRESS(ES)
Air Force Office of Scientific Research
875 N. Randolph, Ste.325
Arlington Virginia, 22203

10. SPONSOR/MONITOR'S ACRONYM(S)
AFOSR

11. SPONSOR/MONITOR'S REPORT NUMBER(S)
N/A

12. DISTRIBUTION/AVAILABILITY STATEMENT
UU: Unclassified Unlimited
A: Approved for Public Release

13. SUPPLEMENTARY NOTES
N/A

14. ABSTRACT
The main project objective was to determine energy distribution of ionosphere electrons accelerated by powerful high-frequency (HF) radio waves transmitted from the High-frequency Active Auroral Research Program (HAARP) transmitter in Alaska. For a given fixed HF-plasma interaction altitude, results from this research show that a dual source of 20 eV electrons applied at 150 km and 200 km altitudes is sufficient to reproduce the substantial artificial airglow and plasma density enhancements created and observed at HAARP during March, 2009. A new discovery resulting from this project is that significant artificial 427.8 nm wavelength airglow can result from thermal heating of the ionosphere plasma and hence is not necessarily an indicator of energetic electrons accelerated to energies exceeding 20 eV as previously assumed. There are several unresolved science issues regarding the spatiotemporal evolution of HF-enhanced airglow and ionization structures. In particular, the apparent sensitive dependence of the artificial airglow and plasma structures on pump frequency relative to electron gyroharmonic frequencies cannot yet be explained, nor can the discrepancy between measurements and calculated dependence of relative intensities of airglow emission lines on altitude.

15. SUBJECT TERMS
Ionosphere, thermosphere, radio, aurora, HAARP

16. SECURITY CLASSIFICATION OF:			17. LIMITATION OF ABSTRACT	18. NUMBER OF PAGES	19a. NAME OF RESPONSIBLE PERSON
a. REPORT	b. ABSTRACT	c. THIS PAGE			Christopher T. Fallen
UU	UU	UU	UU	80	19b. TELEPHONE NUMBER *(Include area code)* (907) 450-8687

Reset

Standard Form 298 (Rev. 8/98)
Prescribed by ANSI Std. Z39.18
Adobe Professional 7.0

INSTRUCTIONS FOR COMPLETING SF 298

1. REPORT DATE. Full publication date, including day, month, if available. Must cite at least the year and be Year 2000 compliant, e.g. 30-06-1998; xx-06-1998; xx-xx-1998.

2. REPORT TYPE. State the type of report, such as final, technical, interim, memorandum, master's thesis, progress, quarterly, research, special, group study, etc.

3. DATES COVERED. Indicate the time during which the work was performed and the report was written, e.g., Jun 1997 - Jun 1998; 1-10 Jun 1996; May - Nov 1998; Nov 1998.

4. TITLE. Enter title and subtitle with volume number and part number, if applicable. On classified documents, enter the title classification in parentheses.

5a. CONTRACT NUMBER. Enter all contract numbers as they appear in the report, e.g. F33615-86-C-5169.

5b. GRANT NUMBER. Enter all grant numbers as they appear in the report, e.g. AFOSR-82-1234.

5c. PROGRAM ELEMENT NUMBER. Enter all program element numbers as they appear in the report, e.g. 61101A.

5d. PROJECT NUMBER. Enter all project numbers as they appear in the report, e.g. 1F665702D1257; ILIR.

5e. TASK NUMBER. Enter all task numbers as they appear in the report, e.g. 05; RF0330201; T4112.

5f. WORK UNIT NUMBER. Enter all work unit numbers as they appear in the report, e.g. 001; AFAPL30480105.

6. AUTHOR(S). Enter name(s) of person(s) responsible for writing the report, performing the research, or credited with the content of the report. The form of entry is the last name, first name, middle initial, and additional qualifiers separated by commas, e.g. Smith, Richard, J, Jr.

7. PERFORMING ORGANIZATION NAME(S) AND ADDRESS(ES). Self-explanatory.

8. PERFORMING ORGANIZATION REPORT NUMBER. Enter all unique alphanumeric report numbers assigned by the performing organization, e.g. BRL-1234; AFWL-TR-85-4017-Vol-21-PT-2.

9. SPONSORING/MONITORING AGENCY NAME(S) AND ADDRESS(ES). Enter the name and address of the organization(s) financially responsible for and monitoring the work.

10. SPONSOR/MONITOR'S ACRONYM(S). Enter, if available, e.g. BRL, ARDEC, NADC.

11. SPONSOR/MONITOR'S REPORT NUMBER(S). Enter report number as assigned by the sponsoring/ monitoring agency, if available, e.g. BRL-TR-829; -215.

12. DISTRIBUTION/AVAILABILITY STATEMENT. Use agency-mandated availability statements to indicate the public availability or distribution limitations of the report. If additional limitations/ restrictions or special markings are indicated, follow agency authorization procedures, e.g. RD/FRD, PROPIN, ITAR, etc. Include copyright information.

13. SUPPLEMENTARY NOTES. Enter information not included elsewhere such as: prepared in cooperation with; translation of; report supersedes; old edition number, etc.

14. ABSTRACT. A brief (approximately 200 words) factual summary of the most significant information.

15. SUBJECT TERMS. Key words or phrases identifying major concepts in the report.

16. SECURITY CLASSIFICATION. Enter security classification in accordance with security classification regulations, e.g. U, C, S, etc. If this form contains classified information, stamp classification level on the top and bottom of this page.

17. LIMITATION OF ABSTRACT. This block must be completed to assign a distribution limitation to the abstract. Enter UU (Unclassified Unlimited) or SAR (Same as Report). An entry in this block is necessary if the abstract is to be limited.

Grant FA9550-12-1-0424

Determining energy distributions of HF-accelerated electrons at HAARP

Christopher T. Fallen
University of Alaska Fairbanks

NOVEMBER 2015
Final Performance Report

AIR FORCE OFFICE OF SCIENTIFIC RESEARCH
875 N. RANDOLPH, STE.325
ARLINGTON VIRGINIA, 22203

TABLE OF CONTENTS

Section **Page**

Table of Contents ..... **i**
List of Figures ..... **ii**
List of Tables ..... **vi**
Preface ..... **vii**
Acknowledgements ..... **viii**
1.0 ABSTRACT **1**
1.1 Background 1
1.2 Executive summary of results 2
2.0 INTRODUCTION **3**
2.1 Artificial radio-induced aurora and accelerated electrons 4
2.1.1 The 630.0 and 557.7 nm wavelength airglow emissions 5
2.1.2 The 427.8 nm wavelength airglow emission 7
2.2 Ionosphere model 11
3.0 METHODS, ASSUMPTIONS, AND PROCEDURES **15**
3.1 Simulation design 16
3.1.1 Diurnal equilibrium solutions 16
3.1.2 Modified energetic electron transport equation 19
3.2 Numerical experiments 24
3.3 Rayleigh: a unit of photon column emission rate or of apparent surface brightness 30
4.0 RESULTS AND DISCUSSION **33**
4.1 Time-dependent ionosphere response 34
4.1.1 Ionosphere critical frequency 34
4.1.2 Photon column emission rates 38
4.2 Altitude profiles 46
4.2.1 Plasma density and temperature 47
4.2.2 Photon volume emission rates 55
4.3 Discussion 62
5.0 CONCLUSIONS **64**
6.0 PUBLICATIONS **65**
7.0 REFERENCES **67**

LIST OF FIGURES

Figure **Page**

Figure 1. Diurnal variation of model airglow column emission rates above Gakona, Alaska on 12 March 2013. 7

Figure 2. Altitude profiles of airglow volume emission rates calculated over Gakona, Alaska during daytime (solid lines) and nighttime (dotted lines). The 630.0 (red), 557.7 (green), and 427.8 nm (blue) wavelength emissions are shown. Resonant scatter of sunlight above the 400 km shadow height at 0630 UTC is responsible for the notch in the nighttime 427.8 nm wavelength emission. 9

Figure 3. Altitude profile of N_2^+ ion loss frequencies calculated from an ionosphere model using chemical reactions and rates provided by *Rees* [1989]. 11

Figure 4. Illustration showing the simulation spatial domain (green line segment) of the Self Consistent Ionosphere Model (SCIM). The curved lines show the geomagnetic field extending from 80 km above Gakona, Alaska to (red) 1100 km and (blue) 11,000 km away. 12

Figure 5. Altitude profiles of ion and plasma number density calculated over Gakona, Alaska with the SCIM (bold colors) and IRI 2007 (faint colors) models..... 13

Figure 6. Altitude profiles of electron, ion, and neutral gas temperatures calculated over Gakona, Alaska with the SCIM (bold red and blue), MSIS (bold black), and IRI (faint red, blue, and black) models..... 14

Figure 7. Model initialization and diurnal variation of background ionosphere F_2-region critical frequency foF2 above Gakona, Alaska from 16 to 17 March 2009. The model begins with a "plasma-free" ionosphere at 18:00 hours and reaches "diurnal equilibrium" in approximately three hours of simulation time..... 17

Figure 8. Diurnal variation of model background ionosphere F_2-region critical frequency foF2 above Gakona, Alaska on 12 March 2013. 18

Figure 9. Diurnal variation of model background ionosphere F_2 region peak density altitude zmF2 above Gakona, Alaska on 12 March 2013. 18

Figure 10. Illustration of simulated energetic electron sources in the Self Consistent Ionosphere Model (SCIM). 21

Figure 11. Total field-aligned electron flux (black) in a natural ionosphere and (red) in an ionosphere modified by electron HF-heating at approximately the greatest plausible heating rate. The flux is calculated at the HF-heating altitude of 254 km for an ionosphere over Gakona, Alaska on 17 March 2009 at 05:15 UTC. 23

Figure 12. Total field-aligned electron flux (black) in a natural ionosphere and (red) in an ionosphere modified by HF-accelerated electrons. The flux is calculated at the HF-acceleration altitude of 154 km for an ionosphere over Gakona, Alaska on 17 March 2009 at 05:15 UTC. 24

Figure 13. Calculated ionosphere foF2 response to thermal electron heating at 250 km altitude with 0.0000, 0.0018, 0.0050, 0.0136, and 0.0368 μW/cm^2 energy flux. . 35

Figure 14. Calculated ionosphere foF2 response to suprathermal electron acceleration at 200 km altitude to 147.78 eV with 0.0000, 0.0018, 0.0050, 0.0136, 0.0368, 0.1000 μW/cm^2 energy flux. Only the two largest energy fluxes exhibited an increase in foF2, apparent in the image as step increases, while the 0.0136 μW/cm^2 flux simulation exhibited a small decrease in foF2. 37

Figure 15. Calculated ionosphere foF2 response to suprathermal electron acceleration to 147.78 eV at 150 km altitude with 0.0000, 0.0018, 0.0050, 0.0136, 0.0368, 0.1000 μW/cm^2 energy flux. Only the two largest energy fluxes exhibited an increase in foF2, apparent in the image as step increases. 38

Figure 16. Measurements of apparent surface brightness of artificial aurora, reprinted from *Hysell et al.* [2014]. The right panel shows the time series of (blue) 427.8, (green) 557.7, (red) 630.0, and 844.6 nm wavelength brightness. 39

Figure 17. First calculation of significant 427.8 nm wavelength "blue line" emissions calculated for simulated thermal electron heating over Alaska. 40

Figure 18. Calculated 427.8 nm wavelength column emission rates for nominal maximum thermal electron heating with 100 nW/cm^2 flux applied at 250 km altitude above Gakona, Alaska. 41

Figure 19. Airglow column emission rates versus time for an ionosphere modified by a 20 eV suprathermal electron source with 4 km thickness and 0.0050 μW/cm^2 of available energy flux, applied at 150, 200, and 250 km altitude above Gakona, Alaska between 0510 and 0515 hours UTC on 17 March 2009. The maximum 427.8 nm column emission rate, approximately 20 R, was obtained with a 250 km source. 43

Figure 20. Field-aligned 557.7 nm airglow (white) and HF-enhanced ion-line intensity (copper) over the HAARP facility in Gakona, Alaska. A wide-field imager located about 160 km north of HAARP measured the airglow intensity. MUIR, collocated with HAARP, measured ion-line intensity. 44

Figure 21. Airglow column emission rates versus time for a 147 eV suprathermal electron source of 4 km thickness with 0.0050 μW/cm^2 of available energy flux, applied at 150, 200, and 250 km altitude above Gakona, Alaska on 17 March 2009. 46

Figure 22. Calculated electron (solid), ion (dashed), and neutral (dotted) temperature profiles following 5 min of electron heating with 5 nW/cm^2 flux applied at 250 km (red), 200 km (green), and 150 km (blue). Black curves show the unmodified ionosphere. 48

Figure 23. Calculated electron number density profiles after 5 min of electron heating with 5 nW/cm^2 flux applied at 250 km (red), 200 km (green), and 150 km (blue) altitude. The black curve shows the unmodified ionosphere. 49

Figure 24. Calculated electron (solid), ion (dashed), and neutral (dotted) temperature profiles after 5 min of electron heating with 5 nW/cm^2 flux applied at 250 km altitude. The ion and electron temperature profiles are calculated for each power flux listed in Table 3, starting with 0 (leftmost respective curve) and ending with 100 nW/cm^2 (rightmost respective curve). 50

Figure 25. Ionograms before (left) and during (middle) heating with approximate scaling curves (right), reprinted from *Pedersen et al.* [2010], measured during the 17 March 2009 experiment at HAARP. 51

Figure 26. Calculated electron (solid), ion (dashed), and neutral (dotted) temperature profiles following 5 min of 20 eV electron acceleration with 5 nW/cm^2 flux applied at 250 km (red), 200 km (green), and 150 km (blue) altitude. Black curves show the unmodified ionosphere. 52

Figure 27. Calculated ionosphere electron number density profiles after 5 min of 20 eV electron acceleration with 5 nW/cm^2 flux applied at 250 km (red), 200 km (green), and 150 km (blue) altitude. The black curve shows the unmodified ionosphere. 53

Figure 28. Calculated ionosphere electron number density profiles after 5 min of 20 eV electron acceleration with 13.5 nW/cm^2 flux applied at 200 km (dotted) and 36.8 nW/cm^2 flux applied at 150 km (solid) altitude. The dashed curve shows the unmodified ionosphere. The power levels were chosen to result in ionosphere plasma density profiles that correspond to the scaled ionograms illustrated in the right panel of Figure 25. 54

Figure 29. Reprinted images from *Pedersen et al.* [2010] showing (top left) images of artificial airglow at 557.7 and 427.8 nm wavelengths at HAARP, (bottom left) time variation of average 427.8 apparent surface brightness, and (right) tomographic reconstruction of estimated enhancements to 557.7 nm wavelength volume emission rates at 210 s into the HF transmitter 'ON' cycle. 55

Figure 30. Calculated natural (dashed) and artificial (solid) 427.8 nm wavelength airglow volume emission rates. The artificial airglow emission is calculated for electron heating at 250 km altitude. 57

Figure 31. Calculated natural (dashed) and artificial (solid) airglow volume emission rates at (blue) 427.8 nm, (green) 557.7 nm, and (red) 630.0 nm wavelengths. The artificial airglow emission is calculated for electron acceleration to 20 eV energy with 5 nW/cm^2 flux at 250 km altitude. 58

Figure 32. Calculated natural (dashed) and artificial (solid) airglow volume emission rates at (blue) 427.8 nm, (green) 557.7 nm, and (red) 630.0 nm wavelengths. The artificial airglow emission is calculated for electron acceleration to 20 eV energy with 5 nW/cm^2 flux at 200 km altitude. 59

Figure 33. Calculated natural (dashed) and artificial (solid) airglow volume emission rates at (blue) 427.8 nm, (green) 557.7 nm, and (red) 630.0 nm wavelengths. The artificial airglow emission is calculated for electron acceleration to 20 eV energy with 5 nW/cm^2 flux at 150 km altitude. 60

Figure 34. Calculated natural (dashed) and artificial (solid) airglow volume emission rates at (blue) 427.8 nm, (green) 557.7 nm, and (red) 630.0 nm wavelengths. The artificial airglow emission was calculated for a 20 eV electron acceleration source with 13.5 nW/cm^2 flux applied at 200 km altitude. 61

Figure 35. Calculated natural (dashed) and artificial (solid) airglow volume emission rates at (blue) 427.8 nm, (green) 557.7 nm, and (red) 630.0 nm wavelengths. The artificial airglow emission is calculated for electron acceleration to 20 eV energy with 36.8 nW/cm^2 flux at 150 km altitude. The enhanced green line emission rate at 150 km altitude is approximately a factor of 10^7 larger than the background value at that altitude. 61

LIST OF TABLES

Table **Page**

Table 1. Experiments with published reports of artificial radio-induced 427.8 nm wavelength airglow. 5

Table 2. Summary of SCIM simulation inputs, parameters, and boundary conditions. 27

Table 3. Altitude-power parameters for SCIM simulations of ionosphere HF-modification experiments. Numerical experiments were performed for every combination of three parameters chosen from each column, in addition to thermal "electron heating" simulations defined by interaction altitude and RF energy flux. 28

Table 4. Suprathermal electron volume production rates (cm^{-3} s^{-1}). The RF energy flux is assumed to be absorbed uniformly over a 4 km thick interaction layer. 30

PREFACE

The main objective of this project was to estimate the energy distribution of ionosphere energetic electrons accelerated by powerful high-frequency (HF) electromagnetic waves transmitted from the High-frequency Active Auroral Research Program (HAARP) facility in Gakona, Alaska. A new discovery was made during the project. Research results described in this report substantially fulfill and expand the planned objectives. The new discovery, that accelerated electrons in the ionosphere may not be necessary to explain the artificial 427.8 nm wavelength airglow emission induced by powerful HF radio waves, expands the main research objective, in part, by providing and analyzing an alternative hypothesis to the generally accepted hypotheses that the artificial 427.8 nm wavelength emission is definitive evidence of energetic electrons accelerated by powerful HF radio waves. It should be noted no direct measurements and only a relatively small set of inferential measurements have been made in support the accepted hypothesis.

ACKNOWLEDGEMENTS

This research project, conducted between 15 August 2012 and 14 August 2015, was supported by the Air Force Office of Scientific Research (AFOSR) Young Investigator Program (YIP) grant FA9550-12-0424 "Determining energy distributions of HF-accelerated electrons at HAARP." The objective of the YIP is to "foster creative basic research in science and engineering; enhance early career development of outstanding young investigators; and increase opportunities for the young investigator to recognize the Air Force mission and related challenges in science and engineering." The Principle Investigator thanks the two AFOSR Program Officers, Dr. Cassandra Fesen and Dr. Kent Miller, who each successively supported this project; and Ms. Ellen Montgomery, who currently manages the AFOSR Young Investigator Program.

1.0 ABSTRACT

The main objective of this project was to determine the energy distribution of ionosphere suprathermal electrons accelerated by powerful high frequency (HF) electromagnetic waves transmitted from the High-frequency Active Auroral Research Program (HAARP) facility in Gakona, Alaska. Available measurements from ground-based instruments include optical imager measurements of artificial airglow brightness at various wavelengths and radar measurements of plasma density. The main methods of estimating energetic electron events in the ionosphere are inversion techniques that use physics-based ionosphere models to calculate simulated ionosphere responses to parameterizations of accelerated electron sources. Simulation results are then matched against measurements to find the set of simulation input parameters that optimize agreement with measurements. These techniques can vary from rigorous mathematical solutions to ad hoc qualitative comparisons. This research used the latter approach. The accuracy of results from both approaches is limited by relatively sparse measurements and incomplete understanding of ionosphere physics. Descriptions of the measurements and model are provided to aid with interpreting the main results.

1.1 Background

Inversion methods using ground-based optical and radar measurements of the upper atmosphere combined, with physics-based modelling, are currently the main available methods for estimating energetic electron energy distributions from aurora or other processes such as powerful high frequency (HF) electromagnetic waves incident on the ionosphere. The 427.8 nm wavelength airglow emission is a key measurement for determining energetic electron flux from optical measurements. Enhanced 427.8 nm wavelength airglow emissions have been reported during ionosphere HF modification experiments conducted during twilight and evening conditions at the EISCAT facility in Norway and the HAARP facility in Alaska. These emissions are attributed to additional production of N_2^+ ions through impact ionization with HF-accelerated electrons. The ionization potential of N_2 exceeds 18 eV, so enhanced impact ionization would indicate the presence of remarkable acceleration processes in the HF-modified ionosphere. However, powerful HF waves are also known to cause significant ionosphere thermal electron heating that has been observed to result in electron temperature enhancements exceeding 3000 K. During twilight conditions, enhanced N_2^+ ion densities above the shadow height will increase 427.8 nm emissions by resonant scattering of sunlight where N_2^+ ions can be lifted from lower altitudes by temperature-enhanced ambipolar diffusion.

Calculations from a 1-dimensional physics-based ionosphere model were performed that demonstrate electron HF-heating alone can be sufficient to produce observed enhancements in 427.8 nm emissions under certain conditions. These numerical results do not necessarily rule out the presence of HF-accelerated electrons (particularly with energy exceeding approximately 20 eV), rather that twilight measurements of airglow intensity alone made are not sufficient evidence of energetic electrons and therefore increases uncertainty in subsequent estimates of

N_2^+ ionization rates, at least not without also accounting for diffusive effects. Simulation results are presented that illustrate HF-accelerated electrons can also produce airglow emissions comparable those reported in the literature, in addition to electron heating and plasma density enhancements that are typical characteristics of many ionosphere radio modification experiments including those conducted during the daytime.

Ultimately, additional measurements are needed to definitively resolve the mechanisms responsible for radio-induced aurora, especially the 427.8 nm wavelength emissions. No incoherent scatter radar (ISR) measurements of plasma density or temperature during HAARP experiments exist, so even basic questions about the background ionosphere state and its response to radio modification cannot be answered without relying on significant assumptions and speculation. Without an ISR, two new experiments using ground-based optical measurements can potentially resolve whether artificial 427.8 nm wavelength emissions are caused by thermal electron heating, suprathermal electron acceleration, by some combination of the mechanisms considered, or perhaps by some other as of yet unknown process. First, simultaneous measurements of emissions from both the first negative bands and Meinel bands can potentially resolve the relative contributions of accelerated electron and fluorescent scattering mechanisms, as the emission rates from these bands are expected to be in strict proportion when resulting from electron impact ionization of N_2 molecules. Second, side-view altitude-resolved 427.8 nm airglow measurements of 427.8 nm airglow can potentially indicate the presence of airglow resulting from enhanced N_2 impact ionization near the HF-plasma interaction altitude separate from N_2^+ ions lifted to sunlit altitudes.

1.2 Executive summary of results

The main project objective was to determine energy distribution of ionosphere electrons accelerated by powerful high-frequency (HF) radio waves transmitted from the High-frequency Active Auroral Research Program (HAARP) transmitter in Alaska. For a given fixed HF-plasma interaction altitude, results from this research show that a dual source of 20 eV electrons applied at 150 km and 200 km altitudes is sufficient to reproduce substantial airglow and plasma density enhancements created above HAARP during March, 2009. These were among the brightest and most exceptional radio-induced airglow and plasma events ever observed. A new discovery resulting from this project is that significant artificial 427.8 nm wavelength airglow can result from thermal heating of the ionosphere plasma and hence is not necessarily an indicator of energetic electrons accelerated to energies exceeding 20 eV as previously assumed. Still, there are several unresolved science issues regarding the spatiotemporal evolution of HF-enhanced airglow and ionization structures. In particular, the apparent sensitive dependence of the artificial airglow and plasma structures on pump frequency relative to nearby electron gyroharmonic frequencies cannot yet be explained. Finally, the expected dependence on relative intensities of the airglow emission lines on emission altitude has not yet been apparent in measurements.

2.0 INTRODUCTION

The ionosphere is a partially ionized plasma generally considered to extend from approximately 80 to 2000 km altitude. The neutral molecules, ions, and electrons composing the ionosphere typically have different temperatures in the E region and above, with the electrons often the warmest of the constituents with temperatures ranging from 1000 K in the lower ionosphere to several thousand Kelvin in the topside ionosphere. A small but significant fraction of ionosphere electrons, almost always less than 0.1%, are very energetic and are said to be *suprathermal* with an energy distribution that deviates from the predominate Maxwellian distribution of velocities. However, suprathermal electrons have great importance in many thermosphere-ionosphere phenomena.

Sources of suprathermal elections in the ionosphere include photoionization processes that create photoelectrons and secondary electrons, auroral precipitation from the magnetosphere, high altitude nuclear explosions, and from high-power high-frequency (HF) electromagnetic waves incident upon the ionosphere. Energy distributions of suprathermal electrons in the ionosphere can be measured in situ with satellites or sounding rockets, as has been done for both photoelectrons and precipitating auroral electrons. With one possible exception, no such direct measurements of electron energy distributions have been made in ionosphere regions affected by powerful HF electromagnetic waves. Instead, ground based optical measurements of artificial airglow (colloquially, "artificial aurora") induced by HF modification (or, "heating") of the ionosphere have been used to both infer the existence of HF-accelerated electrons and their energy distribution.

The artificial aurora is named such as it is because it consists of airglow emissions with wavelengths that have all been observed during natural aurora, and the emissions occur in the same general region of the atmosphere. Therefore, it is reasonable to assume that, like in the aurora, energetic electron impacts with neutral molecules and ions are primarily responsible for artificial aurora airglow emissions. Ground-based optical and radar measurements of the natural aurora have been used in conjunction with inverse methods built on physics-based ionosphere models to estimate the energy distribution of precipitating suprathermal auroral electrons (e.g., see *Rees and Luckey* [1974]). These techniques have recently been applied to the artificial aurora. Key to many current inversion methods, and the strongest evidence for the existence of HF-accelerated energetic electrons, is the 427.8 nm wavelength (blue) airglow emission from N_2^+ molecular nitrogen ions.

Two factors greatly complicate the use of this artificial blue auroral airglow emission to estimate energetic electron distributions. First, molecular nitrogen and its chemistry are very complex and all relevant physical mechanisms need to be included in any inversion method that use this emission. Second, artificial radio-induced 427.8 nm wavelength emissions are very weak, with intensities that are usually barely distinguishable from the background airglow, contaminating light sources, and instrument noise. A brief review of relevant physics and

chemistry important to understanding the results of this research and also to interpreting previously published measurements is provided in this report.

2.1 Artificial radio-induced aurora and accelerated electrons

Artificial auroras can be created by high-power high-frequency (HF) electromagnetic waves beamed into the ionosphere from ground-based transmitters [*P A Bernhardt et al.*, 1988]. The first reported HF-enhanced airglow was detected at the 1.27 μm infrared wavelength at the Platteville high power transmitter facility in Colorado; this emission was surprising and attributed to impact excitation of ground state molecular oxygen $O_2(^3\sum)$ to the $O_2(^1\Delta_g)$ excited state by HF-heated thermal electrons and subsequent de-excitation through photon emission [*Evans et al.*, 1970; *Utlaut*, 1970]. Subsequent measurements at Platteville of simultaneous artificial 630.0 nm "red line" and 557.7 nm "green line" emissions from the $O(^1D)$ and $O(^1S)$ excited states of atomic oxygen with excitation energies of 1.96 and 4.17 eV, respectively, were interpreted by *Haslett and Megill* [1974] to be the result of impact-excitation from the $O(^3P)$ ground state of atomic oxygen by HF-accelerated (suprathermal) electrons. If the observed artificial 557.7 nm emissions followed from $O(^3P) \rightarrow O(^1S)$ impact-excitation by heated (thermal) electrons with a Maxwellian speed distribution, then electron temperatures were calculated to exceede 20,000 K which would have consequently resulted in red-line emissions with intensities several orders of magnitude greater than those observed. Similar measurements of artificial red-line and green-line emissions at the Arecibo Observatory in Puerto Rico [*P Bernhardt et al.*, 1989] and at the EISCAT-Heating facility in Norway [*Gustavsson et al.*, 2002] confirmed that observed ratios of 557.7 to 630.0 nm emission intensities are not consistent with impact excitation of atomic oxygen by heated thermal electrons. This, the presence of HF-accelerated electrons was assumed to be the primary causal mechanism responsible for artificial radio-induced aurora.

Based on measurements of strong HF-enhanced plasma lines that extended in altitude far beyond where HF-induced plasma instabilities were expected above the Arecibo radar and HF-heating facility, *Carlson et al.* [1982] concluded that a population of suprathermal electrons accelerated to an energy of at least 20 eV was consistent with the ISR measurements. *Gurevich et al.* [1985] proposed a theoretical mechanism for accelerating a fraction of ionosphere electrons near the HF reflection height to energies consistent with the airglow observations and power-gain available at the Platteville and Arecibo facilities. The 20 eV HF-accelerated electron energy estimated by *Carlson et al.* [1982] to be available during powerful HF modification experiments exceeds the ionization potential of N_2 molecules. Therefore, measurable 427.8 nm wavelength 'blue-line' airglow emissions from the first negative band excited state of molecular nitrogen ions were expected to occur during HF-modification experiments, especially at the much more powerful EISCAT and HAARP facilities.

Artificial blue-line emissions were subsequently measured during HF-modification experiments conducted at the EISCAT facility in Norway [*Gustavsson et al.*, 2006; *Gustavsson*

et al., 2005; *Holma et al.*, 2006] and the HAARP facility in Alaska [*Pedersen et al.*, 2010]. Measurements of artificial blue-line emission rates have even been used recently to estimate ionization rates [*Mishin and Pedersen*, 2011] and suprathermal accelerated electron energy spectra [*Gustavsson et al.*, 2005] using inversion techniques similar to those described by *Rees and Luckey* [1974]. All artificial 427.8 nm airglow emissions have been interpreted to result exclusively from impact-ionization of N_2 molecules by energetic accelerated by HF radio pump-induced plasma waves.

It is important to note, however, that there are additional potentially relevant mechanisms of 427.8 nm wavelength airglow emissions that can be affected by HF modification of the ionosphere, including resonant scatter of sunlight by N_2^+ ions. All prior experiments that measured 427.8 nm emissions have taken place during evening twilight conditions, when N_2^+ ion density-enhanced resonant scattering of sunlight is a significant source of 427.8 nm enhancements during sunlit aurora [*Remick et al.*, 2001] and therefore cannot be automatically ruled out during artificial aurora. Table 1 shows all published reports of artificial 427.8 nm wavelength airglow emissions. The focus of this work was to analyze the electron heating and electron acceleration hypotheses to explain the airglow observed during the two experiments at HAARP occurring on 17 March 2009 [*Pedersen et al.*, 2010] and 12 March 2013 [*Hysell et al.*, 2014].

Table 1. Experiments with published reports of artificial radio-induced 427.8 nm wavelength airglow.

Experiment date (YYYYMMDD)	Time (UT)	Facility	SZA range (degrees)	SH range (km)	Citation
20011112	1630-1710	EISCAT	106.9-110.4	288.0-426.3	[*Holma et al.*, 2006]
20020307	1820-1900	EISCAT	102.2-105.4	147.7-235.9	[*Gustavsson et al.*, 2006]
20021108	1524-1532	EISCAT	100.2-100.9	103.4-117.2	[*Gustavsson et al.*, 2006]
20020310	1842-1930	EISCAT	102.9-106.5	165.0-273.4	[*Gustavsson et al.*, 2005]
20090317	0513-0517	HAARP	100.3-100.7	104.8-113.4	[*Pedersen et al.*, 2010]
20130312	0610-0640	HAARP	106.7-109.6	282.2-390.8	[*Hysell et al.*, 2014]

2.1.1 The 630.0 and 557.7 nm wavelength airglow emissions

The 630.0 and 557.7 nm wavelength airglow emissions result from deactivation of the $O(^1D)$ and $O(^1S)$ excited states of atomic oxygen atoms, respectively. The primary excitation mechanisms include electron impact excitation by energetic electrons with kinetic energy exceeding the respective energies of 1.96 and 4.17 eV. Both of these excited states are *metastable* and the transition to the ground state is said to be *forbidden*. The lifetime of $O(^1D)$ is approximately 50 s, so below an approximate altitude of 200 km collisions with neutral

molecules tend to de-excite $O(^1D)$ or "quench" without emission of a 630.0 nm photon. The lifetime of $O(^1S)$ is less than 1 s so 557.7 nm emissions are not significantly quenched above an approximate altitude of 100 km.

In the natural ionosphere, energetic electrons are mainly supplied by photoionization processes or auroral precipitation. Thermal electrons from the high-energy tail of the Maxwellian distribution are sufficient to excite the $O(^1D)$ state that yields 630.0 nm wavelength emissions, especially during aurora or HF heating of the ionosphere. Thermal electrons in the ionosphere are generally insufficient to excite the $O(^1S)$ state and the associated 557.7 nm wavelength emission, at least without extreme electron temperatures exceeding 10,000 K that have not been observed in any prior ionosphere HF modification experiment. However, note the important qualification that there are no reliable electron temperature measurements from any HAARP "heating" experiment due to the lack of an ISR near the facility. Finally, it should be noted that the main quiet-time source of 557.7 nm airglow observed in the natural undisturbed nighttime ionosphere is generally agreed to result from the two-step three-body recombination reaction of atomic oxygen to molecular oxygen [*Thomas*, 1981]. This reaction occurs primarily near 100 km altitude and was not relevant to this project.

Figure 1 shows the natural diurnal variation of the column emission rates above Gakona, Alaska on 12 March 2013 at 630.0, 557.7, and 427.8 nm wavelengths, calculated with the Self-Consistent Ionosphere Model (SCIM) developed for this project and discussed in subsequent sections of this report. Column emission rates are expressed in rayleighs (R), a unit of measurement described in section 3.3 and is, in this context, the photon volume emission rate integrated in the vertical (field aligned) direction. The approximate visible threshold at 557.7 nm wavelength in astronomically dark conditions is 1000 R, or the approximate apparent brightness of the Andromeda galaxy. The effects of photoionization processes on the airglow emissions are evident from the relative magnitudes of daytime and nighttime airglow intensities. (Alaska Standard Time is nine hours behind Universal Standard Time i.e. UTC-9.) As mentioned previously, the primary source of 557.7 nm airglow at night is the three-body recombination reaction and its nighttime variation apparent in the figure is the response to semidiurnal neutral atmosphere tides.

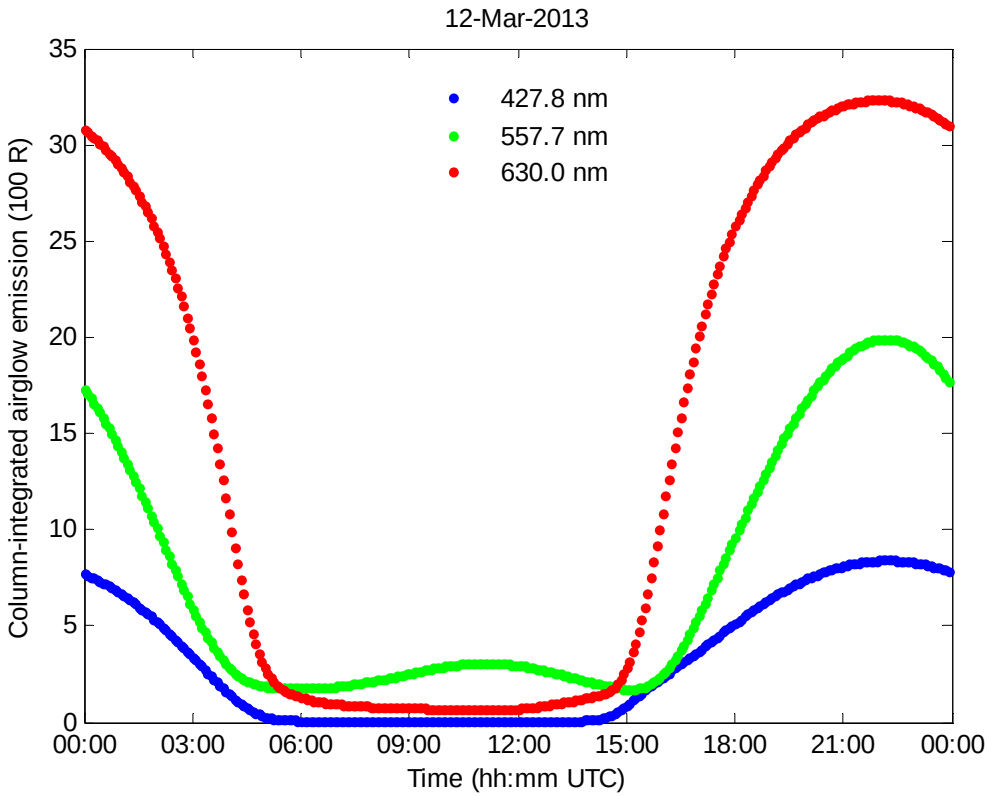

Figure 1. Diurnal variation of model airglow column emission rates above Gakona, Alaska on 12 March 2013.

2.1.2 The 427.8 nm wavelength airglow emission

Molecular nitrogen ions are a minor constituent in the ionosphere plasma due to efficient loss mechanisms, primarily through chemical reactions with atomic oxygen. Nevertheless, optical emissions from the Meinel (M) and first negative (1NG) band systems of N_2^+ ions are observable from the ground and arise from electronic transitions from the N_2^+ ion A and B excited states, respectively, to the ground state. Unlike the near-infrared emissions from the Meinel system which compete with the OH nightglow which is typically more intense, the 427.8 nm 'blue-line' emission from the 1NG system (0, 1) band is a distinct auroral feature with no significant nearby nightglow or band emission [*Henriksen*, 1984]. Molecular nitrogen ion emissions are detectable in ground-measured spectra from the aurora, day aurora, twilight glow, and dayglow [*Broadfoot*, 1967].

The 427.8 nm 'blue-line' emission from the first negative band of the molecular nitrogen ion N_2^+(B) excited state is primarily caused by ionization of molecular nitrogen through impact with energetic electrons or photons. Molecular nitrogen has an ionization potential of approximately 19 eV and a significant fraction of the resulting molecular nitrogen ions are created in excited A and B states. The de-excitation occurs almost immediately with a corresponding photon

emission. Electron impact ionization of molecular nitrogen is a significant atmospheric source of M and 1NG band emissions during auroras (see e.g., *Chamberlain* [1995]). Resonant scatter of sunlight by newly ionized N_2^+ ions, and also by N_2^+ ions lifted through temperature-enhanced ambipolar diffusion, is also a significant source of M and 1NG emissions at high latitudes during aurora occurring in the spring and fall when the ionosphere is sunlit for a significant fraction of the time the ground is in darkness [*Remick et al.*, 2001]. The prompt emission reactions of the A and B excited states of N_2^+ ions are summarized in equation (1) [*Broadfoot*, 1967; *Broadfoot and Hunten*, 1966].

$$\begin{aligned} \mathrm{N}_2^+\left(B^2\Sigma_u^+\right) &\rightleftarrows \mathrm{N}_2^+\left(X^2\Sigma_g^+\right) + h\nu\left(\lambda = 427.8\ \mathrm{nm}\right) \\ \mathrm{N}_2^+\left(A^2\Pi\right) &\rightleftarrows \mathrm{N}_2^+\left(X^2\Sigma_g^+\right) + h\nu\left(\lambda = 1104.0\ \mathrm{nm}\right) \end{aligned} \tag{1}$$

Figure 1 shows the natural diurnal variation of the column emission rates at the 427.8 nm wavelength calculated with SCIM. Similar to the 630.0 and 557.7 nm emissions, the effects of photoionization processes 427.8 nm wavelength emissions are evident. Figure 2 shows nighttime and daytime altitude profiles of the 630.0, 557.7, and 427.8 nm wavelength volume emission rates above Gakona, Alaska on 12 March 2013 at 0630 and 1830 hours UTC. The important role of impact excitation by suprathermal photoelectrons (and secondary electrons) for daytime airglow is clearly evident in the differences between the respective profiles of airglow volume emission rate at each wavelength. Note in particular that the importance of resonant scatter of sunlight by N_2^+ ions is particularly evident in the nighttime (twilight) profile of the 427.8 nm wavelength volume emission rate. Above approximately 400 km altitude, that is, above the shadow height above Gakona at 0630 UTC on 12 March 2013, the 427.8 nm wavelength emission rate increases by two orders of magnitude. This affect is only of minor importance relative to photoionization and impact ionization of N_2 molecules during the daytime.

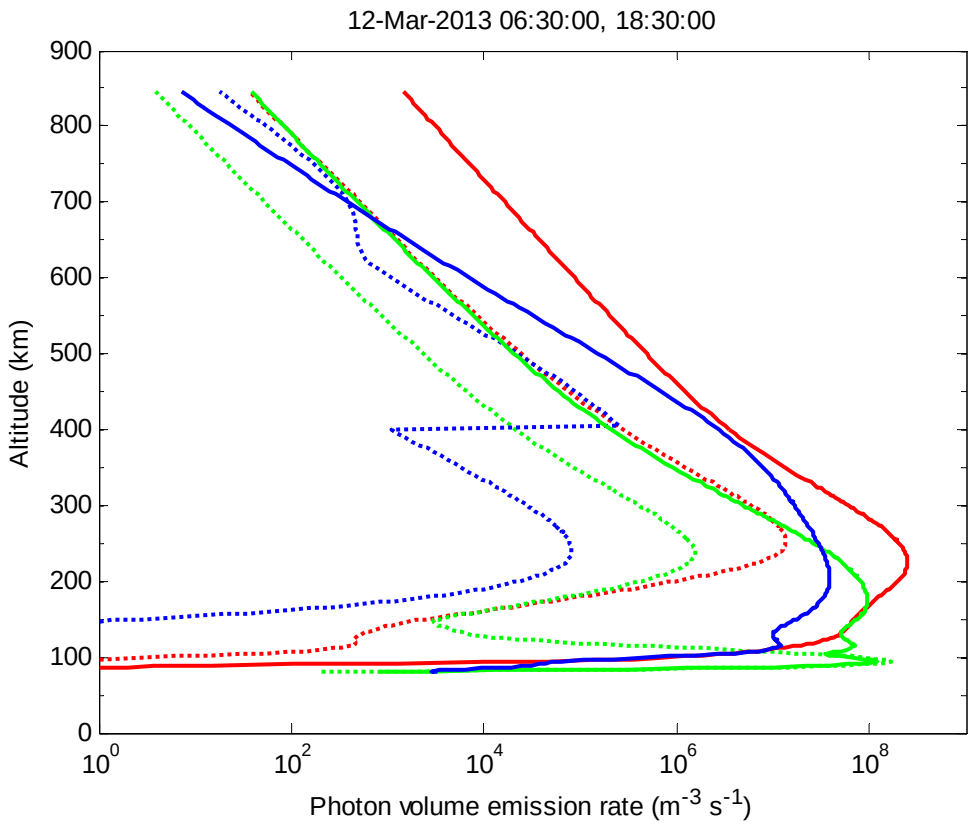

Figure 2. Altitude profiles of airglow volume emission rates calculated over Gakona, Alaska during daytime (solid lines) and nighttime (dotted lines). The 630.0 (red), 557.7 (green), and 427.8 nm (blue) wavelength emissions are shown. Resonant scatter of sunlight above the 400 km shadow height at 0630 UTC is responsible for the notch in the nighttime 427.8 nm wavelength emission.

Understanding the role of N_2^+ resonant scatter of sunlight in natural and artificial 427.8 nm wavelength aurora requires knowledge of the space- and time-dependence of N_2^+ ion density and the ionosphere plasma response to heating and new ionization. The number density of ionosphere N_2^+ at a given location is determined by the balance of production, loss, and divergent transport processes. Radio modification of the ionosphere impacts all three processes. Thermal heating of the electron gas affects temperature-dependent N_2^+ recombination rates and the divergence of ambipolar diffusion flux. Electron temperature enhancements during O-mode F-region heating above facilities such as HAARP and EISCAT can reach in excess of 3000 K, and can extend hundreds of kilometers along the geomagnetic field from the original HF-plasma interaction (heating) region.

Sources of ionosphere excited state N_2^+ ions include electron impact ionization of N_2 molecules, resonant scattering of sunlight by ground-state N_2^+ ions, chemical production, and photoionization of N_2 molecules. In the topside ionosphere, divergent transport of N_2^+ ions from lower altitudes can also be a significant source. The major local N_2^+ ion production reactions are summarized in equation (2) [*Broadfoot*, 1967; *Broadfoot and Hunten*, 1966].

$$\begin{aligned} \mathrm{N}_2 + e^* &\rightarrow \mathrm{N}_2^+\left(A^2\Pi,\ B^2\Sigma_u^+,\ X^2\Sigma_g^+\right) + 2e \\ \mathrm{N}_2^+\left(X^2\Sigma_g^+\right) + h\nu &\rightleftarrows \mathrm{N}_2^+\left(A^2\Pi,\ B^2\Sigma_u^+\right) \\ \mathrm{O}^+\left(^2D\right) + \mathrm{N}_2 &\rightarrow \mathrm{O} + \mathrm{N}_2^+\left(A^2\Pi,\ v' = 1\right) \\ \mathrm{N}_2\left(X^1\Sigma_g^+\right) + h\nu\left(\lambda < 79.6\ \mathrm{nm}\right) &\rightarrow \mathrm{N}_2^+\left(A^2\Pi,\ B^2\Sigma_u^+,\ X^2\Sigma_g^+\right) + e \end{aligned} \tag{2}$$

The primary N_2^+ loss mechanisms are through chemical reactions with atomic and molecular oxygen molecules. Reaction with nitric oxide (NO) molecules and electron recombination can be major loss mechanisms as well under certain conditions but are typically of secondary importance. In the E region and lower F region (below approximately 150 km altitude) the lifetime of an N_2^+ ion is less than approximately 0.1 s where O and O_2 molecule densities are relatively high. Therefore, transport effects can be neglected in these regions. The diffusion time τ of N_2^+ in this region can be estimated to be greater than 10,000 s from the N_2^+ ion scale height H and its ambipolar diffusion coefficient D:

$$\tau = \frac{H^2}{2D} \tag{3}$$

In the topside ionosphere at or above approximately 350 km altitude, divergent transport of N_2^+ ions from lower altitudes can be a significant source of N_2^+ ions as well as a correspondingly significant loss mechanism at the N_2^+ peak density layer altitude. At 400 km altitude above Gakona, the lifetime of an N_2^+ ion exceeds 100 s and its diffusion time is approximately 10 s. Figure 3 shows typical altitude profiles of N_2^+ ion number density and loss frequencies above Gakona, Alaska calculated with SCIM. Typical electron number density and neutral number density profiles are shown as well for reference. The relevant chemical reactions and reaction rates used in the model from *Rees* [1989] are also listed.

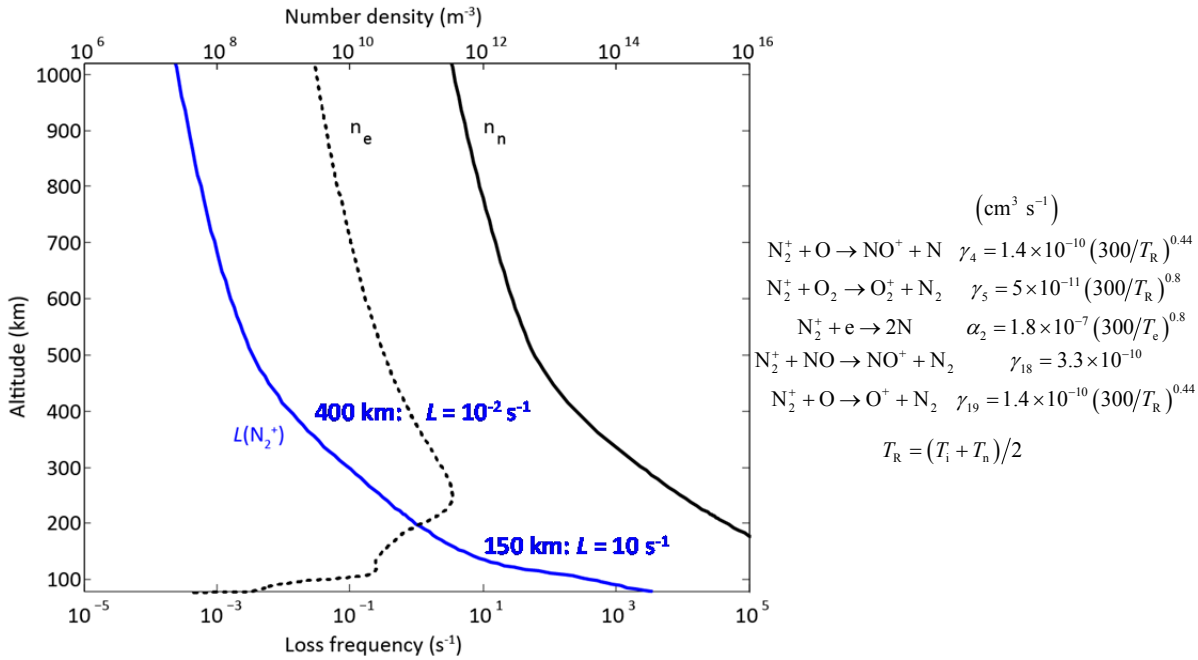

Figure 3. Altitude profile of N_2^+ ion loss frequencies calculated from an ionosphere model using chemical reactions and rates provided by *Rees* [1989].

The intensity of 427.8 nm wavelength airglow will fluctuate with N_2^+ ion density since each N_2^+ ion resonantly scatters sunlight at a constant rate [*Broadfoot*, 1967]. Therefore, plasma temperature-enhanced long-distance transport of N_2^+ ions to higher sunlit altitudes can potentially be a source of enhanced 427.8 nm wavelength airglow enhancements during ionosphere HF modification experiments, without the need for HF-accelerated suprathermal electrons with energies of approximately 20 eV or greater. However, any attempt to quantify the variation in 427.8 nm airglow intensity expected from the ionosphere response to electron heating or acceleration requires accurately describing the vertical (field aligned) composition and temperature of the high-latitude ionosphere. This task involves solving a coupled set of nonlinear partial differential equations describing the continuity and momentum of each ion species and temperatures of the plasma.

2.2 Ionosphere model

A new Self-Consistent Ionosphere Model (SCIM) was constructed to calculate the response of a one-dimensional, slab symmetric, high-latitude ionosphere to either electron heating or electron acceleration (or both) in the bottom-side ionosphere, at altitudes directly modified by powerful HF waves from facilities such as HAARP or EISCAT. Figure 4 shows the typical 80 to 1000 km vertical simulation domain (green bar) above the HAARP facility in Gakona, the corresponding length (red) along the geomagnetic field line terminating in Gakona, and the field line (blue) extending 11,000 km (approximately half the distance of the median orbit altitude for

Global Positioning System satellites) for visual context of the relevant geometry. Although SCIM simulates a vertical ionosphere with corrective terms to account for a geomagnetic field that is, in Gakona, approximately 15° off vertical, this approximation is adequate over the limited simulation domain and it allows for a number of simplifications in the model equations and simulation software code.

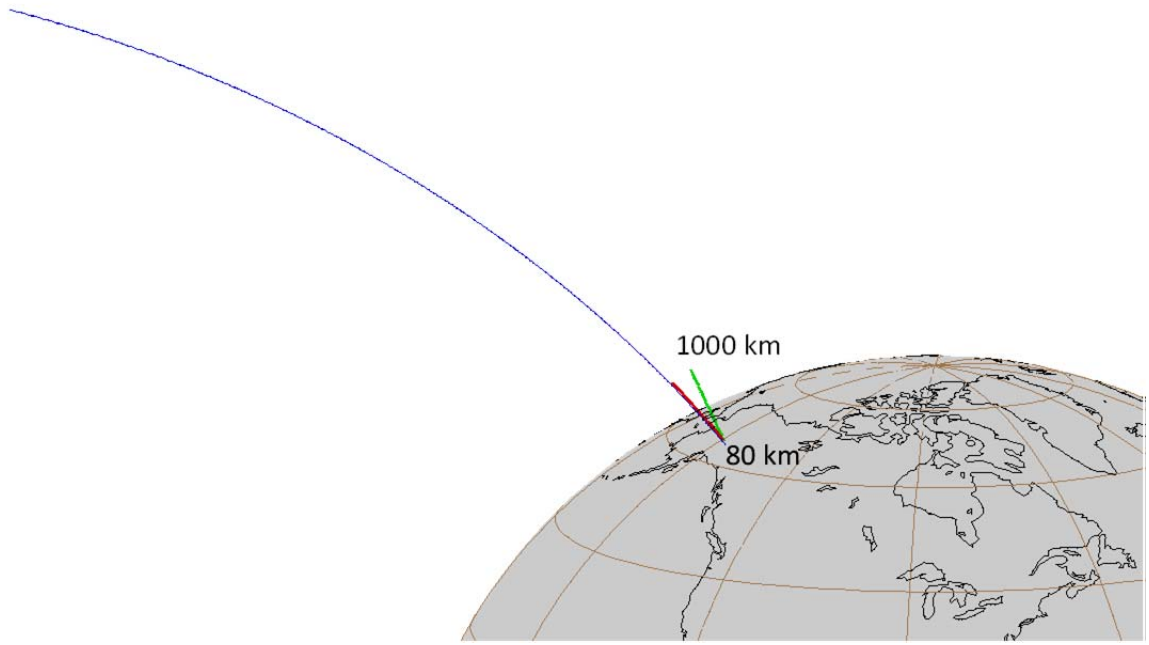

Figure 4. Illustration showing the simulation spatial domain (green line segment) of the Self Consistent Ionosphere Model (SCIM). The curved lines show the geomagnetic field extending from 80 km above Gakona, Alaska to (red) 1100 km and (blue) 11,000 km away.

The new ionosphere model was largely based on the previous version of SCIM [*C. T. Fallen and Watkins*, 2010; *Christopher T. Fallen et al.*, 2011]. In brief, the model calculates time-dependent altitude profiles of the ionosphere plasma density, composition, ionization rates, heating rates, and temperatures for a specified high-latitude location when provided with a solar ionizing photon spectra in addition to the composition, temperature, and velocity of the neutral atmosphere. For this research, the solar ionizing spectra was provided by the EUVAC empirical model and neutral atmosphere parameters were provided by the NRLMSISE-00 (MSIS) [*Picone et al.*, 2002] and HWM93 [*Drob et al.*, 2008] empirical models.

Changes were made to the base software source code to: 1. Accommodate an additional energetic electron transport calculation that allowed for acceleration sources to be placed at arbitrary locations in the domain, 2. Implement ion excited-state chemistry calculations, and 3. Implement airglow volume emission rate calculations. The specific physical mechanisms added to the model for this research are described in section 3.1 (Simulation design). New simulation

data products include time- and altitude-dependent energetic electron energy distributions and airglow volume emission rates at a variety of wavelengths.

Figure 5 and Figure 6, reprinted from *Fallen* [2010], show typical daytime ionosphere plasma composition and temperature profiles calculated over Gakona, Alaska. Results are shown from both the original physics-based SCIM model and the IRI 2007 [*Bilitza and Reinisch*, 2008] empirical model. A physics-based model was required for this research to calculate the ionosphere response to the input of thermal electron heat or accelerated suprathermal electrons, which is not possible with empirical or "table lookup" models such as IRI. Note in particular from the ion composition profiles that N_2^+ ions are an extremely minor constituent of the ionosphere plasma at all altitudes. However, measurements of the airglow emissions from excited states of N_2^+ ions provide one of the major experimental techniques for increasing the current understanding of physical processes involved in the natural and artificial aurora.

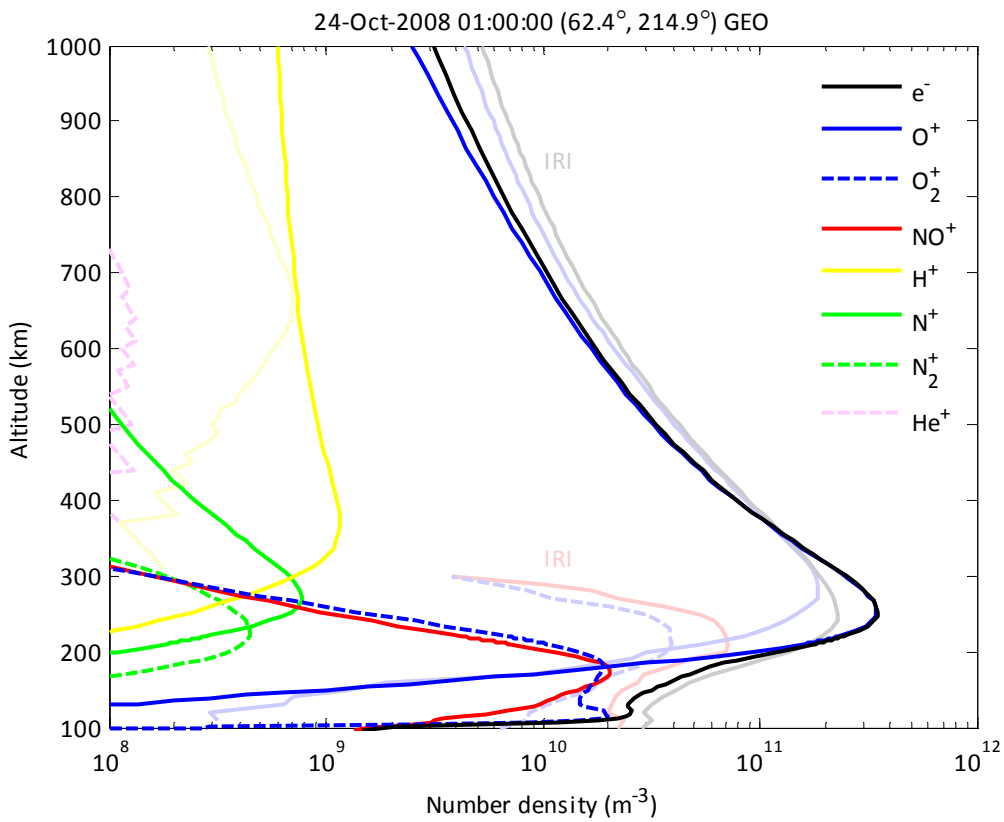

Figure 5. Altitude profiles of ion and plasma number density calculated over Gakona, Alaska with the SCIM (bold colors) and IRI 2007 (faint colors) models.

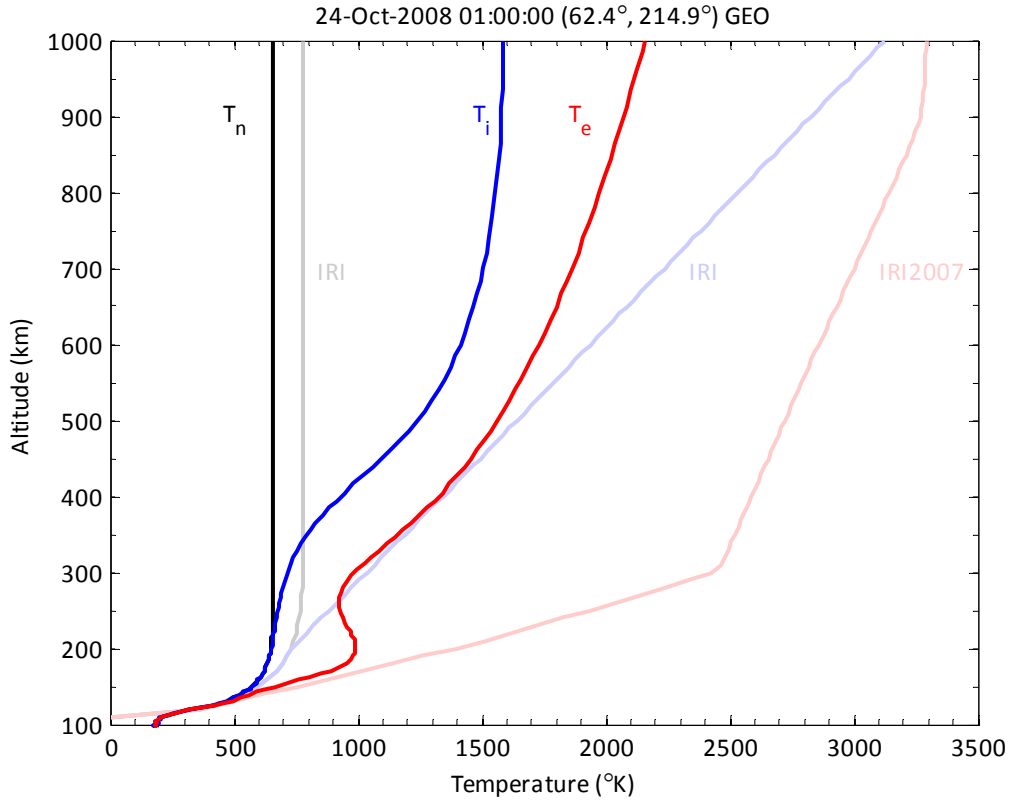

Figure 6. Altitude profiles of electron, ion, and neutral gas temperatures calculated over Gakona, Alaska with the SCIM (bold red and blue), MSIS (bold black), and IRI (faint red, blue, and black) models.

3.0 METHODS, ASSUMPTIONS, AND PROCEDURES

The main objective of this project was to estimate the energetic electron distribution during ionosphere modification experiments at the HAARP facility in absence of in-situ measurements. Inverse problem methodology is generally the main remaining tool available, which in this problem domain, used detailed physical modeling of the ionosphere response to a source of energetic electrons which was then compared to available measurements. The sudden shutdown of the HAARP facility during this project and the temporary prolonged loss of data access was fortuitous in some ways. It allowed for a more detailed modelling effort and analysis that led to discovery of an additional potentially important physical mechanism for modulating the 427.8 nm wavelength airglow emission: resonant scatter of sunlight from N_2^+ ions lifted from lower altitudes through temperature-enhanced ambipolar diffusion. Calculations and simulation case studies were made to analyze its possible contribution to HF-enhanced 427.8 nm wavelength airglow observed at the HAARP and EISCAT facilities.

The 427.8 nm blue-line emission is of critical importance to most inversion techniques for determining suprathermal electron energy distributions from spectroscopic measurements in natural aurora [*Rees and Luckey*, 1974; *Rees and Lummerzheim*, 1989; *Rees et al.*, 1988] and artificial aurora [*Hysell et al.*, 2012; *Hysell et al.*, 2014; *Mishin and Pedersen*, 2011]. Including all relevant contributing physical mechanisms to the 427.8 nm wavelength emission is necessary for the inversion technique results to have accuracy and relevance. Therefore, in light of the new discovery regarding an additional plausible artificial 427.8 nm emission mechanism, the focus of this project pivoted somewhat from determining detailed structure of HF-enhanced suprathermal electron distributions in the ionosphere above HAARP, as was already provided anyway by *Hysell, Miceli et al.* [2014] during the timeline of this project, to providing better understanding of the physical processes involved, at least in the aeronomy sense.

In this section, first, the Self Consistent Ionosphere Model (SCIM) will be described in brief, with emphasis on the new energetic electron transport calculation developed for this project. (Section 2.1 describes the relevant airglow emission mechanisms implemented in the model for this project.) Second, the specific numerical experiments performed and their relevant parameters will be discussed. Results from these numerical experiments are presented in section 4.0. Third, the unit of column photon emission rate, the rayleigh (R), calculated by SCIM is briefly discussed and compared with the rayleigh (R) unit of apparent surface brightness. These two units have the same name and, under a specific set of assumptions, the theoretical rayleigh unit (of column photon emission rate) is numerically equivalent to the measurement rayleigh unit (of apparent surface brightness). However, it is crucially important to be aware of the different interpretations of these units when comparing theoretical calculations of photon emission rates to measurements of apparent surface brightness, and to critically evaluate whether the assumptions made in each case are largely compatible.

3.1 Simulation design

The Self Consistent Ionosphere Model (SCIM) software code is, fundamentally, a loop in simulation time that repeatedly solves sequential set of equations. Each iteration consists of a "time step" that is usually set between 1 and 600 s. The equations, described by *Fallen* [2010], determine the response of the model ionosphere from the previous time step to external "drivers" such as the MSIS neutral atmosphere and solar zenith angle that are usually advanced each time step. There are two sets of equations that are solved sequentially in time as in a "leapfrog method."

The first set of equations solved each time step, immediately following updates to the simulation drivers and boundary conditions, define the "fast" response of the ionosphere, that is, to the ionosphere responses that typically reaches equilibrium over the entire simulation domain in a time much than a second. These fast quantities include photoionization and excitation rates, suprathermal electron energy transport, electron impact ionization and excitation rates, and airglow volume emission rates. The majority of the simulation development for this project went toward the code that solved for fast ionosphere responses.

The second set of equations solved each time step define the "slow" responses of the ionosphere that occur on time scales greater than seconds that are also, in many cases, altitude dependent. These slow quantities include number density of the various ion species, ion temperature, and electron temperature. A fully coupled set of nonlinear parabolic differential equations is numerically solved to calculate the ionosphere slow responses.

3.1.1 Diurnal equilibrium solutions

Simulations of the ionosphere response to high-power HF radio waves or other disturbances such as aurora, including those described in this report, were constructed by first calculating a "diurnal equilibrium" solution of the ionosphere under typical drivers that vary diurnally such as solar zenith angle (SZA), MSIS neutral atmosphere composition and temperature, and downward electron heat flux from the magnetosphere. Subsequent simulations of ionosphere "modification events" such as aurora or powerful HF pump-wave effects use smaller time steps starting from a diurnal equilibrium solution used for supplying initial conditions. Figure 7 shows the ionosphere F_2-region critical frequency (foF2) calculated as a function of time from a diurnal equilibrium simulation, initialized from a plasma-free neutral atmosphere provided by MSIS. The location was chosen to be above Gakona, Alaska and the time ranged from 16 to 17 march 2009, covering the experiment reported by *Pedersen, Gustavsson et al.* [2010]. Approximately three hours of simulation time are required for the calculated ionosphere plasma density to reach diurnal equilibrium in the F_2 region.

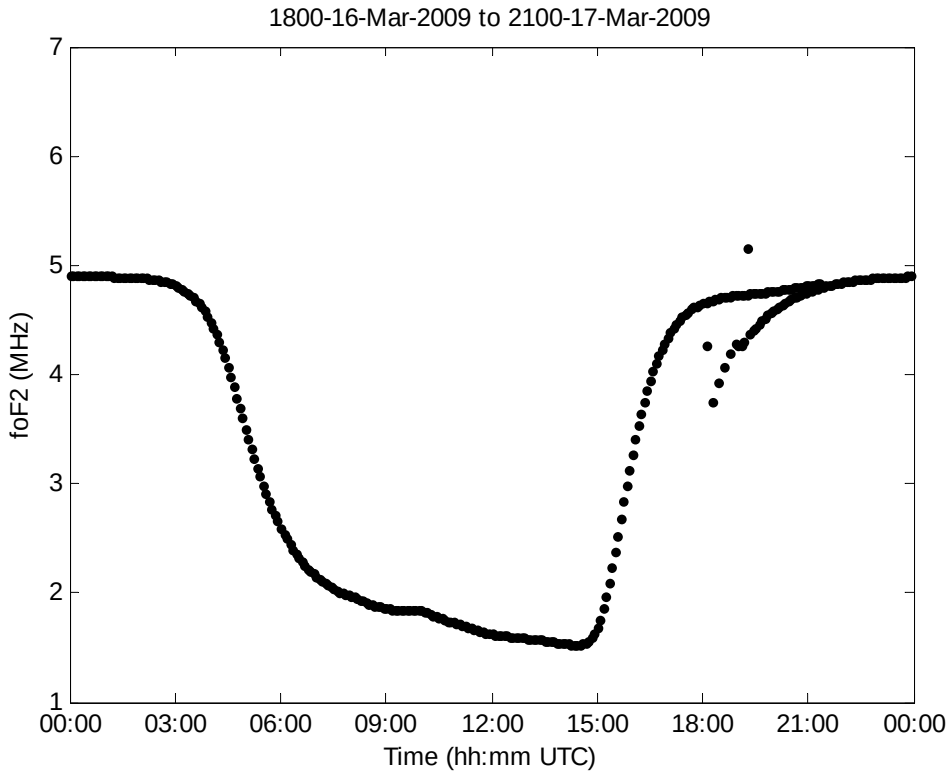

Figure 7. Model initialization and diurnal variation of background ionosphere F_2-region critical frequency foF2 above Gakona, Alaska from 16 to 17 March 2009. The model begins with a "plasma-free" ionosphere at 18:00 hours and reaches "diurnal equilibrium" in approximately three hours of simulation time.

Figure 8 and Figure 9 show the critical frequency foF2 and the F_2-region peak density height zmF2, respectively, of an ionosphere over the same Gakona location on 12 March 2013. The total simulation duration is greater than 24 hours but the diurnally-varying neutral atmosphere parameters are set to repeat the conditions for 12 March 2013 instead of advancing to 13 March 2013. Repeated values of foF2 and zmF2 are overlaid with the previous values in each figure. Both figures demonstrate stability of the simulation solution beyond 24 hours beyond the initialization time. Variations in foF2 and, particularly, zmF2 that cannot be attributed to changing SZA are caused by semidiurnal variations in neutral atmosphere density and variations in neutral atmosphere wind velocities. Section 3.2 describes specific simulation parameters used in the diurnal equilibrium simulations.

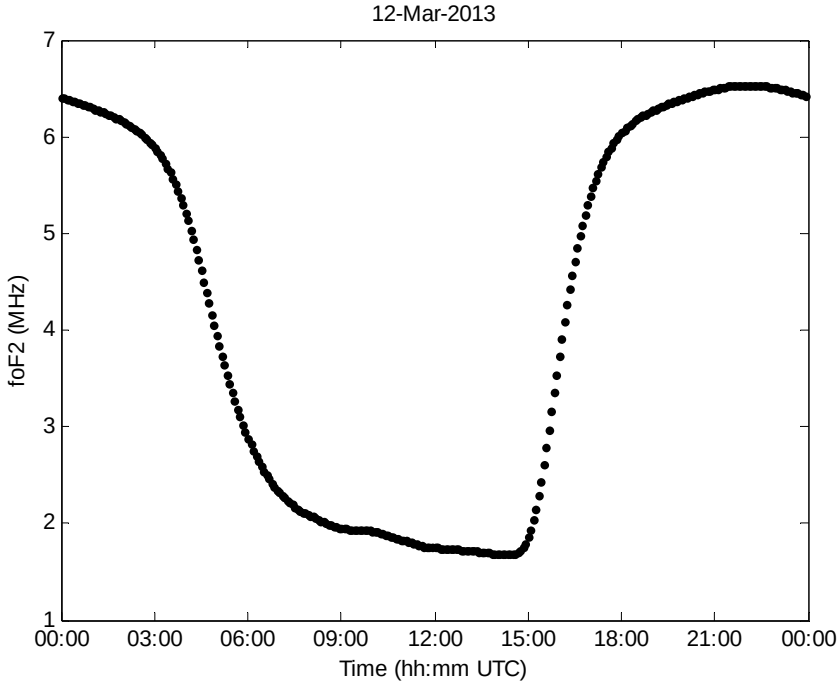

Figure 8. Diurnal variation of model background ionosphere F_2-region critical frequency foF2 above Gakona, Alaska on 12 March 2013.

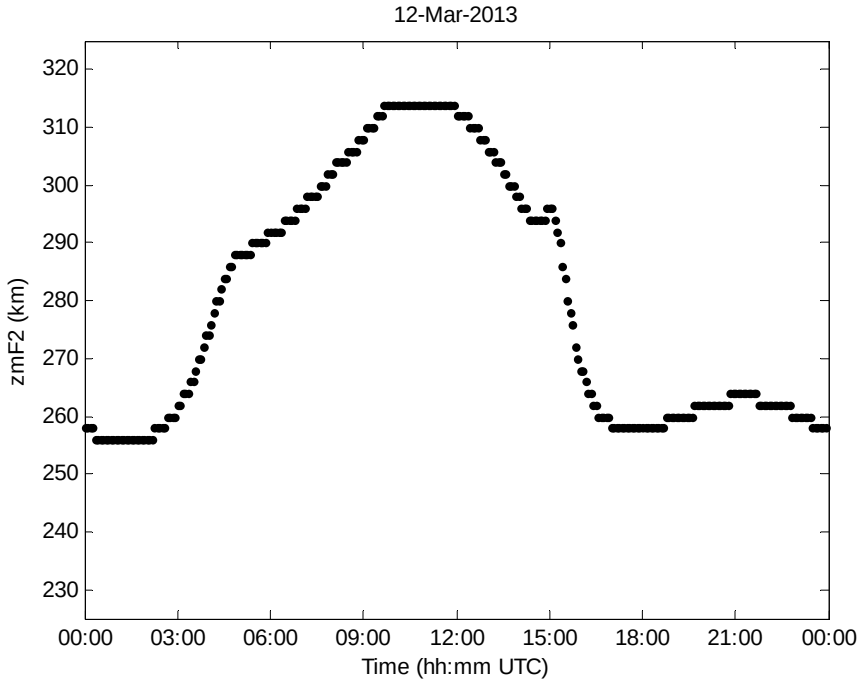

Figure 9. Diurnal variation of model background ionosphere F_2 region peak density altitude zmF2 above Gakona, Alaska on 12 March 2013.

3.1.2 Modified energetic electron transport equation

Physics-based ionosphere models must account for the effects of energetic electron transport, particularly for the transport of photoelections and secondary electrons. Photoelectrons and secondary electrons cause impact ionization, impact excitation, and electron heating effects. Several of these effects have can be approximated by empirical parameters, such as those used in the original SAMI2 mid-latitude ionosphere model [*Huba et al.*, 2000]. However, in order to calculate the effects of energetic auroral electron precipitation or HF-accelerated energetic electrons, an energetic electron transport equation must be solved for the energy distribution at each point along the geomagnetic field. For this project, code that solved the two-stream electron energy transport equation [*Nagy and Banks*, 1970] was adapted to allow for sources of energetic electrons specified by altitude, energy, production or acceleration rate. The SAMI-PE model uses a full multi-stream energetic electron calculation [*Varney et al.*, 2012] but the effects are not expected to differ substantially from the classical two-stream method.

Figure 10 illustrates the field-aligned geometry of the new energetic electron energy transport equation. The boundaries at 100 and 1000 km altitude were chosen for the purpose of this illustration but are not the exact model boundary altitudes used. The two-stream electron transport equations, specifically equations (1) and (2) from *Nagy and Banks* [1970], solve for upward and downward electron flux along the geomagnetic field as functions of altitude and energy throughout the simulation domain. The differential equations were then solved using the Crank-Nicolson finite-difference numerical method. An upper boundary condition such as the downward energetic electron flux $\phi_0(\epsilon, t)$ as a function of energy ϵ and time t in Figure 10, can be set arbitrarily. Most common choices include a null spectrum, the precipitating electron flux from upward traveling photoelectrons from the hemispheric conjugate point, an auroral electron energy precipitation distribution, or, typically in SCIM, a soft electron precipitation with a Maxwellian energy distribution and characteristic energy of 50 eV as has been assumed in other physics-based high-latitude ionosphere models such as *Min* [1993]. The lower boundary condition is typically set to a null spectrum.

Prior to this research, and that of *Hysell, Miceli et al.* [2014], simulations of ionosphere modification experiments were made by adding an HF-electron volume heating rate to the thermal electron energy equation over an altitude region of several kilometers to tens of kilometers in the E or F regions, depending on the HF-modification experiment to be simulated. (The bottom-side F region, between about 150 and 250 km altitude at the HAARP facility, is typically modified in “O-mode” experiments and the E region is typically modified in “X-mode” experiments.) The HF-enhanced electron volume heating rate itself is still not a well understood quantity. One reasonable approach is to start with the available HF electromagnetic energy flux at the interaction altitude and assume that this power is absorbed uniformly throughout the interaction region. While uniform power absorption throughout the interaction region is probably not a good assumption, repeated ionosphere modification simulations made with SCIM have demonstrated that the ionosphere response is not sensitive to the size of the interaction region,

only to the total energy flux and the altitude of the interaction region itself (e.g., see *Fallen* [2010]). Consequently, suppose the HF energy flux at the interaction altitude is ϕ_{HF} (expressed, say, in units of watts per square meter), a dimensionless "efficiency factor" ε is introduced where $0 \le \varepsilon < 1$ indicates net absorption of the pump wave and $\varepsilon > 1$ indicates plasma self-focusing of the pump wave, and the interaction layer thickness is set at Δs meters, then the simulated HF-electron volume heating rate in the interaction layer can be expressed as:

$$Q_{\mathrm{HF}} = \varepsilon \frac{\phi_{\mathrm{HF}}}{\Delta s} \tag{4}$$

However, the value of that energy flux itself is difficult to estimate as it can be lower than that expected from the net HF transmitter power and antenna gain due to high D-region absorption. Alternately, in some cases the energy flux can be larger than the nominal absorption-free value due to plasma self-focusing effects. Consequently, this is a quantity that is extremely difficult to estimate without repeated measurements made remotely with radar or in situ with sounding rockets or satellites. Consequently, the transfer rate of electromagnetic energy from the HF pump wave to the ionosphere plasma must be a "tunable" model parameter that is estimated from reasonable assumptions about the pump wave and adjusted until the calculated ionosphere response matches available measurements.

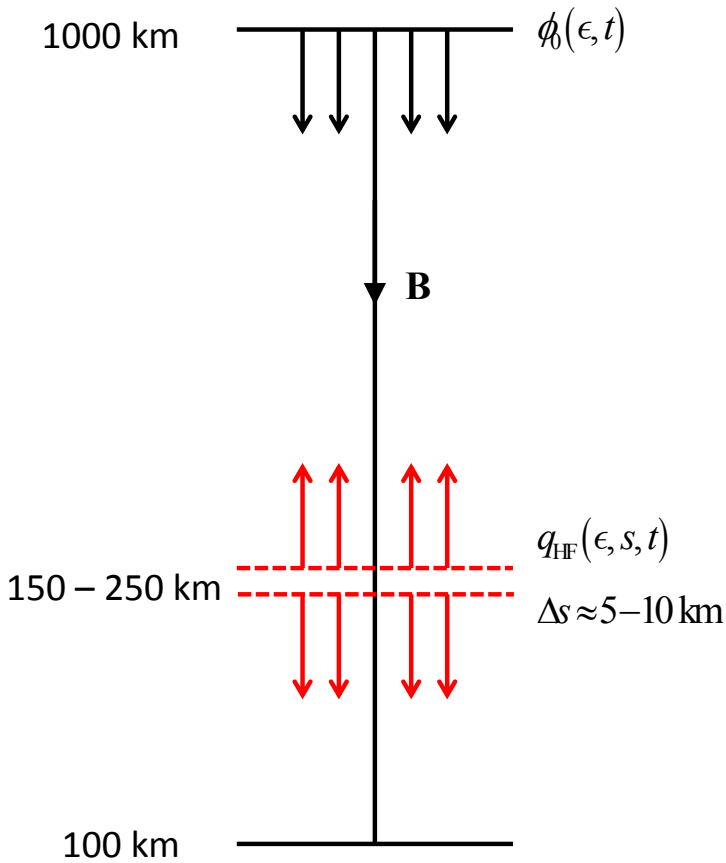

Figure 10. Illustration of simulated energetic electron sources in the Self Consistent Ionosphere Model (SCIM).

To estimate the suprathermal electron HF-acceleration rate (the number of electrons accelerated to energy ϵ per unit volume by the pump wave) at a given altitude s, the HF pump wave energy flux ϕ_{HF} is again assumed to be absorbed uniformly throughout the interaction layer of thickness Δs. Since the population of thermal electrons in the ionosphere generally has kinetic energy of only a few tenths of an electron volt, and the suprathermal electron energies of interest range from several electron volts to tens of electron volts, it is assumed here that the energy required to accelerate a thermal electron to energy ϵ is the same as ϵ. Consequently the simulated HF-electron acceleration rate, with the efficiency factor ε, can be expressed as:

$$q_{HF}(\epsilon) = \varepsilon \frac{1}{\epsilon} \frac{\phi_{HF}}{\Delta s} \tag{5}$$

Figure 11 shows an example of the calculated combined upward and downward energetic electron flux in the interaction region for a simulated ionosphere HF-modification experiment where the electrons were heated via equation (4). The numerical experiment that produced the

image is from a simulation case study of the HF-modification experiment at HAARP on 17 March 2009 at 05:15 UTC [*Pedersen et al.*, 2010]. Simulated electron temperatures in the interaction region at 254 km altitude, near the F-region peak density height, were elevated approximately 8000 K, which is perhaps an upper bound of possible heating at HAARP (recall that no definitive electron temperature measurements have been made yet at HAARP), resulting in a significant increase in energetic electrons with energies below approximately 5 eV.

The suprathermal electron flux shown in Figure 11 is sufficient to cause a measurable enhancement of 630.0 nm wavelength airglow emissions since the difference between the corresponding ground state and 1D excited state of atomic oxygen is approximately 2 eV, but not the 557.7 nm wavelength emission since the difference between corresponding the ground and 1S excited states of atomic oxygen is approximately 5 eV. (The 427.8 nm wavelength emission is a more complicated case, as described in section 2.1.) This particular "electron heating" ionosphere modification simulation, discussed by *Fallen and Watkins* [2014] and in section 4.0 of this report, represents the maximum 427.8 nm wavelength emissions expected to be possible by HF-heating of the thermal electrons without any suprathermal electron acceleration processes during the ambient geophysical conditions at the time of the experiment.

Figure 12 shows an example of the calculated combined upward and downward energetic electron flux for a simulated mono-energetic 20 eV electron acceleration source, with volume production rate estimated with equation (5) to be consistent with power available during a typical HAARP O-mode experiment. The suprathermal electron energy distribution does not appear to contain a Dirac delta function "spike" as might initially be naively expected due to the mono-energetic electron acceleration source. However, the solution of the electron transport calculation is steady-state, so the increase in flux at all energies less than the acceleration energy is a consequence of inelastic collisions of the accelerated electrons with the ambient atmospheric constituents.

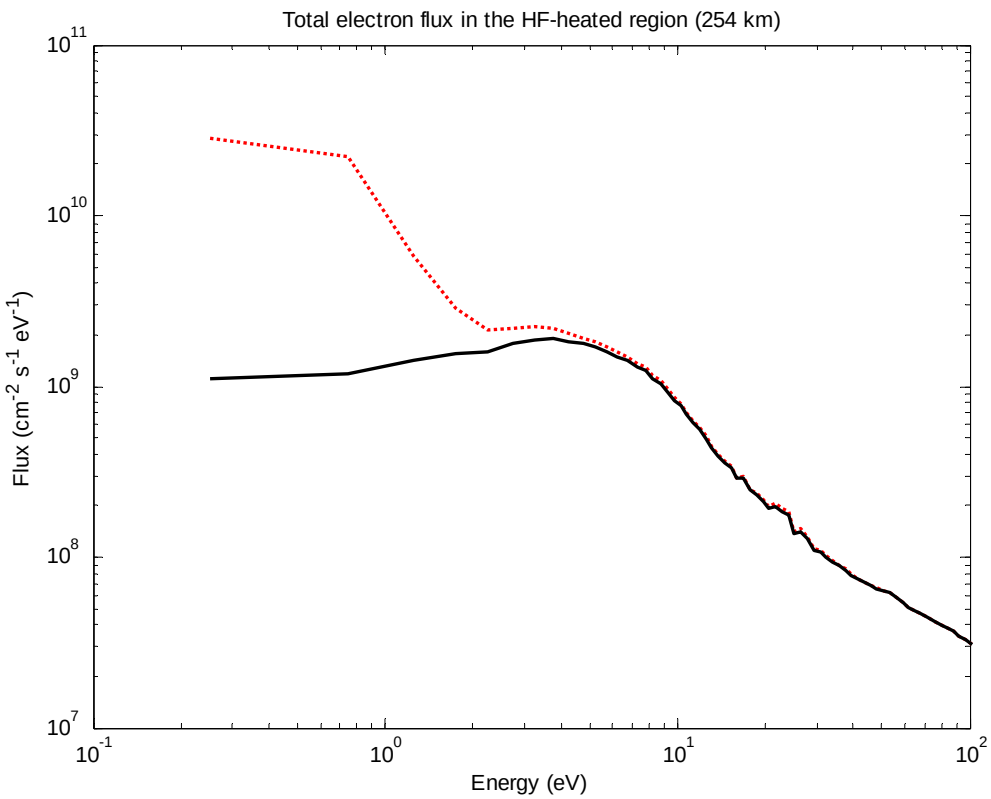

Figure 11. Total field-aligned electron flux (black) in a natural ionosphere and (red) in an ionosphere modified by electron HF-heating at approximately the greatest plausible heating rate. The flux is calculated at the HF-heating altitude of 254 km for an ionosphere over Gakona, Alaska on 17 March 2009 at 05:15 UTC.

Finally, it should be noted that the energetic electron transport calculation developed and used for this research was partially validated for natural auroral precipitation. Preliminary examples of these calculations and comparisons with measurements for soft electron precipitation events were performed [*C. T. Fallen*, 2013; *C. T. Fallen and Watkins*, 2013a; b; c]. A more detailed validation involving inversion of electron density profiles measured with the EISCAT radar and airglow measured with ground-based photometers during two different auroral events are provided by *Oyama, S. I., Shiokawa, K., Miyoshi, Y., Hosokawa, K., Watkins, B. J., Kurihara, J., Tsuda, T., and Fallen, C. T.* [Submitted to JGR Space Physics, 2015JA022129].

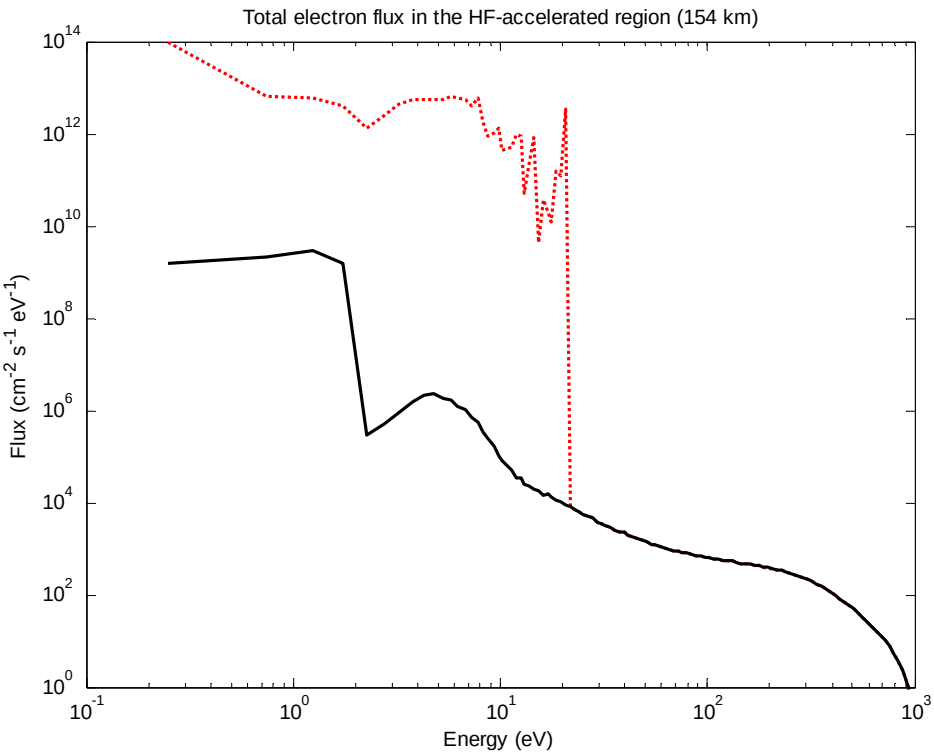

Figure 12. Total field-aligned electron flux (black) in a natural ionosphere and (red) in an ionosphere modified by HF-accelerated electrons. The flux is calculated at the HF-acceleration altitude of 154 km for an ionosphere over Gakona, Alaska on 17 March 2009 at 05:15 UTC.

3.2 Numerical experiments

Numerical experiments were performed to map the simulated ionosphere modification parameter space calculations of airglow volume emission rates, plasma composition, and plasma temperatures as functions of altitude. Each simulation is time dependent over a set of time-dependent geophysical conditions and simulated ionosphere HF-modification parameters, so the parameter space represents variations in interaction type (HF-heating of thermal electrons or HF-acceleration of suprathermal electrons), interaction layer altitude, and volume power transfer density (equivalently, uniform energy transfer flux over identical-thickness interaction layers). The specific ionosphere modification experiments simulated include both the two HAARP experiments listed in Table 1. The parameter space of the EISCAT experiments listed in the table was also partially explored, but it was found the results described in section 4.0 appeared to also apply without loss of generality to the simulated EISCAT experiments provided altitudes and calculated airglow emissions are scaled according to the more active geophysical conditions occurring during the EISCAT experiments.

Table 2 lists the main simulation parameters for the diurnal equilibrium and HF-modification numerical experiment parameters that are common to all simulations. In particular, the results reported here are for an ionosphere over Gakona, Alaska (location of the HAARP facility) on either 17 March 2009 or 12 March 2013. Each of the two finalized diurnal equilibrium solutions were initialized from an ionization-free atmosphere and the initial conditions for the HF-modification simulations were drawn from the diurnal equilibrium solutions. The time-step for the diurnal equilibrium solutions was 300 s and the time-step for the HF-modification simulations was 10 s.

Simulation altitude boundaries were set at 80 and 845 km. The altitude grid used piecewise-uniform spacing to allow fine resolution at low altitudes where large spatial gradients of ionosphere state variables occur and coarse resolution at high altitudes with small spatial gradients. Grid spacing was chosen so that the total power transferred to the ionosphere through the simulated HF "source" was constant in both the electron HF-heating and HF-acceleration experiments. Previous ionosphere HF-modification simulations with SCIM allowed for a variable-altitude and variable-thickness HF-interaction region in attempt to simulate the time-dependent HF-plasma interaction altitude that are believed to depend on the plasma and upper-hybrid resonance frequencies which can change in response to ionosphere radio modification. When the heater frequency is held constant, electron heating or suprathermal electron acceleration causes variations in ionosphere plasma density which in-turn cause variations in HF-plasma interaction altitude and thickness. However, simulations that maintain constant total power transfer from the pump wave to the ionosphere plasma, typically specified in simulated power volume density rates (say, watts per cube meter), while maintaining expected HF-plasma interaction constraints—that still are not yet well understood—greatly increases simulation coding complexity.

The neutral atmosphere provided by the MSIS and HWM empirical models varied diurnally according to the F107, F107A, and Ap indices recorded for each experiment day. Neutral atmosphere parameters and the solar zenith angle were updated with each time step. The solar ionizing photon spectra was held constant for each numerical experiment and was provided by the EUVAC empirical model initialized to the F107 index for the specified experiment day. A constant perpendicular electric field magnitude of 5 millivolts per meter was imposed on all simulations to provide a source of ion joule heating appropriate for modest $\mathbf{E}\times\mathbf{B}$ ion drift speeds typical of the quiet geophysical conditions present during the experiments. Finally, a diurnally-varying downward electron thermal heat flux appropriate for the month of March over Alaska was applied to the upper boundary condition for the thermal electron energy equation. This downward thermal electron heat flux from the magnetosphere was derived from International Polar Year (IPY) long-duration low duty-cycle Advanced Modular Incoherent Scatter Radar (AMISR) measurements made at Poker Flat, Alaska [*C. T. Fallen and Watkins*, 2013b]. The empirical heat flux model boundary condition was developed in part for this project to improve accuracy of the SCIM electron density and temperature calculations for nighttime conditions,

when artificial airglow experiments are typically performed and when the ionosphere is particularly sensitive to electron heat flux from the magnetosphere.

Table 3 lists the parameter space for each the simulations of ionosphere HF-modification experiments at the HAARP facility occurring on 17 March 2009 and 12 March 2013. An electron HF-acceleration simulation was performed for each combination of interaction altitude, HF energy flux, and accelerated electron energy (mono-energetic accelerated electrons) specified in each column of the table. Corresponding classical electron HF heating simulations were performed for combination of interaction altitude and HF energy flux values in the left two columns of the table. Additionally, a "control" experiment of the natural ionosphere for each HAARP experiment listed in Table 1 was performed so that the HF modification simulations could be compared to the natural background ionosphere. More than 100 simulations were performed to map the altitude-power-energy-mechanism parameter space for each of the two HAARP modification experiments (i.e. more than 200 final numerical experiments in total)[1]. Additionally, the parameter space of simulated ionosphere modification experiments at EISCAT, also listed in Table 1, was partially explored but did not appear to yield substantially different results from the HAARP simulations.

Interaction altitudes listed in the first column Table 3 were chosen to range from the approximate typical F-region peak electron density altitude above HAARP down to the approximate lowest altitude of airglow emissions observed during O-mode experiments. Typically the interaction region descends in tens of seconds by several kilometers altitude, and sometimes tens of kilometers. This phenomena was discovered and described by *Watkins, Fallen et al.* [2013]. The rate and extent of the HF wave-plasma interaction region descent depends on the ionosphere plasma frequency resonance altitude corresponding to the pump frequency relative to the electron gyroharmonic frequency near that altitude. No attempt was made in this project to model the descending interaction region which allowed for more simple numerical experiment design and interpretation of results. The interaction layer thickness in all modification experiments was assumed to be 4 km which consisted of three altitude grid points in the model.

[1] Only simulations with the three largest energy fluxes each paired with the 130-134 km interaction region were performed, and several of the simulation solutions did not converge due to the difficulty in simultaneously simulating the transport-dominated F region and the upper E region where ion densities are determined by photochemical equilibrium. Exceptionally steep density and temperature gradients occurred at the 130 – 134 km altitude interaction region so a more refined spatial grid, and correspondingly greater simulation time, would have been required for simulation convergence.

Table 2. Summary of SCIM simulation inputs, parameters, and boundary conditions.

Parameters	Values
GEOSPATIAL	
Time dependence	24 hour cyclic diurnal cycle
Location	Gakona, Alaska (62.4°, 214.9°) GEO
Time step	300 s for diurnal equilibrium simulations to calculate initial conditions 10 s for ionosphere modification simulations
Vertical grid	240 points distributed as follows: 1 km spacing between 80 and 90 km altitudes 1.5 km spacing between 91.5 and 130 km 2 km spacing between 132 and 330 km 5 km spacing between 335 and 845 km
ION AND ELECTRON LOWER BOUNDARY CONDITIONS	
Altitude	80 km
Number density	Photochemical equilibrium
Temperature	MSIS neutral gas temperature
ION AND ELECTRON UPPER BOUNDARY CONDITIONS	
Altitude	845 km
Number density flux	0.0 $m^{-2}\,s^{-1}$ (all species)
Electron thermal energy flux	Time dependent, based on *Fallen and Watkins* [2013b]
Ion thermal energy flux	0.0 μW m^{-2} (ion gas)
Energetic electron flux	Non-auroral simulations include soft 50 eV Maxwellian electron precipitation with flux 20 μW m^{-2}
AMBIENT GEOPHYSICAL CONDITIONS	
$\lvert \mathbf{E}_{\perp} \rvert$	5 mV m^{-1}
Solar parameterization	EUVAC [*Richards et al.*, 1994] based on the F107 index
Neutral atmosphere composition, temperature, and winds	MSIS00 and HWM93 based on Ap, F107, and F107A indices

Table 3. Altitude-power parameters for SCIM simulations of ionosphere HF-modification experiments. Numerical experiments were performed for every combination of three parameters chosen from each column, in addition to thermal "electron heating" simulations defined by interaction altitude and RF energy flux.

Interaction altitudes (km)	RF energy fluxes ($\mu W/cm^2$)	Accelerated electron energies (eV)
250 to 254	0.1 exp(-4) = 0.0018	20 exp(-2) = 2.71
200 to 204	0.1 exp(-3) = 0.0050	20 exp(-1) = 7.36
150 to 154	0.1 exp(-2) = 0.0135	20 exp(0) = 20.00
130 to 134	0.1 exp(-1) = 0.0368	20 exp(1) = 54.37
	0.1 exp(0) = 0.1000	20 exp(2) = 147.78

HF energy fluxes listed in the second column Table 3 defined the simulated power transfer rates from the HF pump wave to the ionosphere in the interaction region, either through electron acceleration or thermal electron heating. Equation (4) defined the thermal electron volume heating rate from the HF pump wave energy flux for the thermal electron HF-heating numerical experiments. For the suprathermal electron HF-acceleration numerical experiments, both the pump wave energy flux and accelerated electron energy in Table 3 define the volume production rate for mono-energetic suprathermal electrons with energy ϵ through equation (5). The suprathermal electron volume production rates are also calculated on the assumption of uniform absorption of RF energy flux throughout the 4 km interaction layer to arrive at an HF-plasma energy volume transfer rate $\phi_{\mathrm{HF}}/\Delta s$.

There is another complication in choosing the RF power fluxes and associated volume energy transfer rate, in addition to those mentioned in section 3.1. The "interaction altitude" during ionosphere modification experiments is generally near the altitude where the ionosphere plasma frequency matches the chosen pump frequency (say, 2.8 MHz). However, the HAARP antenna gain changes significantly with the chosen pump frequency and the net transmitted power is typically chosen to be the maximum power available. The net transmitted power does not significantly change with pump frequency. Furthermore, the actual RF energy flux from HAARP, like all sources of electromagnetic flux, varies with the inverse square of the distance to the interaction region, or approximately, the altitude. Both of these complications are tractable, albeit somewhat cumbersome to program, but were not addressed in the model created for this research as the solution further complicates interpretation of the model results. Instead the RF

energy flux parameters were systematically chosen to range from the approximate maximum possible HAARP electromagnetic power flux in the F region (without absorption or plasma self-focusing effects), a tenth of a microwatt (or 100 nanowatts) per square centimeter, with each lessor power flux set to be a factor of Euler's number *e* less than the previous flux. It should be noted that very little is actually known about the effective energy transfer rate from the pump beam to the ionosphere plasma during any ionosphere HF-modification experiment.

The monoenergetic suprathermal accelerated electron energy values in Table 3 were chosen in a similarly systematic mathematical method as the energy flux values. Each energy value differs from the next largest or smallest value by a factor of Euler's number. The base value of 20 eV was chosen because it is slightly greater than the ionization energy of molecular nitrogen and electron impact ionization of N_2 molecules is one of the physical mechanisms responsible for 427.8 nm wavelength airglow. The next smallest values of suprathermal electron energy, 7.36 and 2.71 eV, are each slightly larger than the excitation energies for the 1S and 1D excited states from the ground state of atomic oxygen responsible for the 557.7 and 630.0 nm wavelength airglow emissions, respectively. The next largest energy value above the base value is 54.37 eV and is somewhat greater than the approximate 30 eV characteristic energy of the auroral electron precipitation estimated to be responsible for the famous type A intense "blood red" aurora occurring during the great geomagnetic storm of 10 February 1958 [*Robinson et al.*, 1985]. The next greater and largest energy value is 147.78 eV and generally represents an approximate upper bound of suprathermal electron energy believed obtainable with ground-based HF radio transmitters.

Table 4 shows the resulting accelerated electron production rates, for each choice of accelerated electron energy and available RF energy flux, applied uniformly to the 4 km interaction layer. Note that the maximum production rate of the highest energy electrons is numerically equal to the minimum production rate of the lowest energy electrons, etc., through the systematic choice of parameterization. The two HAARP experiments simulated in detail were "on-off" experiments with duty cycles of a few minutes. Without loss of generality, the simulated experiments consist of a single electron HF-heating or HF-acceleration "on" time with a duration of five minutes.

Table 4. Suprathermal electron volume production rates (cm^{-3} s^{-1}). The RF energy flux is assumed to be absorbed uniformly over a 4 km thick interaction layer.

		Suprathermal electron energy (eV)				
		2.7067	**7.3576**	**20**	**54.3656**	**147.7811**
RF Energy flux ($\mu W/cm^2$)	**0.0018316**	7039.137	2589.554	952.644	350.458	128.926
	0.0049787	19134.358	7039.137	2589.554	952.644	350.458
	0.013534	52012.578	19134.358	7039.137	2589.554	952.644
	0.036788	141384.845	52012.578	19134.358	7039.137	2589.554
	0.1	384323.856	141384.845	52012.578	19134.358	7039.137

3.3 Rayleigh: a unit of photon column emission rate or of apparent surface brightness

Theoretical or numerical model calculations must be compared with measurements in order to evaluate understanding of physical processes believed responsible for a given phenomenon. For this research, the modelled and measured airglow intensity was compared. However, this comparison is not as straightforward as might be expected, despite the use of apparently equivalent units for expressing and relating two distinct physical phenomena: the photon emission rates emitted by a column of gas (calculated by the model) and photon collection rates measured by an instrument (reported as a surface brightness). These two physical units are equivalent under certain conditions and assumptions.

The rayleigh (R) was originally defined as a unit of measure for the total column emission rate from an optically thin gas species in the upper atmosphere [*D. J. Baker and Romick*, 1976]. This is a convenient unit to calculate when the isotropic volume emission rate φ is known as a function of distance along a line defining the view of an "observer." Symbolically, let r be the distance along this path, $\Delta\varphi$ be the isotropic volume emission rate at some specified wavelength or wavelengths from volume ΔV at position r, and $\phi = \lim_{\Delta V \to 0} \Delta\phi / \Delta V$. Then the isotropic column emission rate η is the line-of-sight column integral of the volume emission rate:

$$\eta = \int_{\text{column}} \phi(r)\, dr \tag{6}$$

The *rayleigh* is thus defined as a unit of this column emission rate to be:

$$1 \text{ rayleigh} = 1 \text{ R} = 10^{10} \ \frac{\text{photons}}{\text{sec}\left(\text{m}^2 \text{ col}\right)} \tag{7}$$

This is the rayleigh unit of column photon emission rate used in this report to describe the simulated intensity of airglow emissions from a column of the upper atmosphere along the magnetic zenith.

The rayleigh is also a unit of measured apparent surface brightness, and this dual definition can be used without any loss of generality under specific circumstances [*D. J. Baker and Romick*, 1976]. Specifically, the two definitions are equivalent when "the field of view of a photometric instrument is completely and uniformly filled by an extended isotropic radiation source" [*Doran J. Baker*, 1974]. However, even if this criterion is met, this equivalence still requires careful calibration of the instrument, beyond the tacit understanding that scattering and reabsorption of the emission along the line of sight are unknown. For artificial aurora resulting from ionosphere HF modification experiments, there are several additional points of note that cloud the comparison of calculated column emission rates and measurements of apparent spatial brightness.

First, in order to assume equivalence of the two rayleigh units of measurement, spatial inhomogeneities in the column emission are assumed to occur only on much larger scales relative to the field of view of the instrument [*J. W. Chamberlain*, 1961]. This is often not the case with artificial airglow emissions observed at the HAARP or EISCAT facilities (e.g., decameter-scale structures were observed by *Kendall, Marshall et al.* [2010]). Second, ground-based measurements of artificial airglow intensity enhancements, expressed in rayleighs, often involve subtracting out the background intensity. However, as can be seen in plots of simulated diurnal airglow intensity variation such as Figure 1, the background intensity can change significantly over time scales of minutes during evenings when typical artificial airglow measurements are taken. Even after astronomical twilight, the upper atmosphere may still be sunlit with the column density of sunlit gas species changing with time. Third, measured artificial airglow intensity enhancements, particularly the 427.8 nm wavelength emission, are weak and enhancements are comparable to the background intensity. Fourth and finally, the vertical extent of ionosphere modifications including airglow enhancements during cases where the modification occurs near the F-region peak density layer, calculated to extend several hundreds of kilometers along the geomagnetic field. There are conflicting observations and assumptions regarding this in the literature, particularly in regards to "spherical" [*Gustavsson et al.*, 2001] or "filamentary" [*Kosch et al.*, 2007; *Pedersen et al.*, 2010] regions of artificial airglow extent.

Therefore, caution should be used when making direct numerical comparisons between the column emission rates calculated from modeled volume emission rates and column emission rates inferred from measurements of apparent surface brightness. When possible, relative quantities should be used for comparisons, such as the relative change in intensity from the background or the ratios of intensities measured at different wavelengths. General conclusions on physical processes can still be drawn from calculated or observed changes of airglow intensity (or the lack thereof).

The uncertainties in the available optical measurements of apparent surface brightness are substantial, including: 1. the dynamic small-scale structures observed in the optical measurements, particularly of the 427.8 and 557.7 nm wavelength emissions; 2. the uncertainty of the appropriate altitude range to integrate without altitude-resolved optical measurements; and, 3. the artificial 427.8 nm wavelength intensities are extremely weak and are only slightly more than the instrument noise. Therefore, in light of the optical measurement uncertainties, rigorous inversion techniques for calculating energetic electron spectra was not performed with the simulation calculations. Instead, the results presented in section 4.0 represent a qualitative estimation of plausible electron heating rates, acceleration rates, and energies. Graphs of parameterized ionosphere profiles and airglow column emission rates are used to provide intuitive illustrations of the ionosphere effects from heated or accelerated electrons, the effects of which are very sensitive to the altitude where the electron heat or acceleration sources are applied.

4.0 RESULTS AND DISCUSSION

Overall results include more than 200 time-dependent and altitude-dependent simulations of plasma composition, temperature, and airglow volume emission rates at various wavelengths for both EISCAT and HAARP experiments, particularly those conducted on 17 March 2009 [*Mishin and Pedersen*, 2011; *Pedersen et al.*, 2010] and 23 March 2013 [*Hysell et al.*, 2014] at HAARP. First, the time dependent response of the ionosphere in terms of O-mode critical frequency foF2 and photon column emission rates are presented for selected modification mechanisms (electron heating or electron acceleration energy), total RF-plasma energy transfer flux, and modification source altitude. Constraints on accepted modelling results include the following reported observations during experiments when artificial 427.8 nm wavelength airglow was measured:

17 March 2009 [*Mishin and Pedersen*, 2011; *Pedersen et al.*, 2010]

1. The onset of artificial 427.8 nm wavelength emissions occurred almost immediately after the pump wave transmissions began.
2. The maximum artificial 427.8 nm wavelength intensity of ~20 R occurred approximately 20 s after start of the pump wave and then steadily descended to ~5 R at 240 s.
3. The artificial aurora was reported to be faintly visible to the unaided eye, indicating that the 555.7 nm wavelength apparent surface brightness was approximately 1000 R, or the 630.0 nm wavelength intensity was approximately 3000 R, or probably some combination of both emissions.
4. Artificial plasma "layers" at 150 km and 200 km altitude were reported with plasma density of approximately 10^5 cm^{-3}, comparable to the F-region peak density nmF2 at the time of the experiment. The pump frequency was maintained near foF2, which was not observed to change in response to heating, so the layers are interpreted as "descending" ionization starting at 250 km altitude.
5. The most intense 557.7 nm wavelength airglow was estimated to have a volume emission rate of approximately 10 cm^{-3} s^{-1} at the ~150 and 200 km altitude plasma density enhancements.

23 March 2013 [*Hysell et al.*, 2014]

6. The average artificial airglow apparent surface brightness measured by *Hysell, Miceli et al.* [2014] was also ~20 R but was described as "barely" statistically significant.
7. The average 557.7 and 630.0 nm wavelength intensities were measured to be approximately 500 and 2000 R, respectively.
8. The 557.7 nm wavelength airglow was spatially inhomogeneous and time varying, with local maxima intensities of approximately 5 times the average intensity.
9. Artificial airglow was described to be "clearly visible" to the unaided eye.
10. Modest plasma density enhancements of approximately 10^4 cm^{-3} were reported at approximately 210 km altitude.

4.1 Time-dependent ionosphere response

The simulated ionosphere modification simulations described in this section use a 10 s time step. The figures illustrate the simulated ionosphere response to electron heating or electron acceleration, applied to an interaction region at various altitudes with various energy transfer rates and characteristic energies. Constraints on possible driven energetic electron energies and fluxes are developed through a two-step process of first eliminating simulations where the calculated time dependent electron density characterized by time-dependent foF2 show substantial increases over the background values.

The calculated ionosphere plasma density response to electron heating and acceleration altitude dependent. One characteristic the two target experiments share is that neither reported changes in the ionosphere foF2 which was continuously measured with an ionosonde co-located with the main HF transmitter at HAARP. There is some evidence that O-mode HF pumping can cause decreases in foF2, however. Multiple previous heating experiments conducted at the EISCAT reported measuring a decrease in F-region peak ionosphere plasma volume density nmF2 of up to 20% during O-mode transmissions during pumping with radio frequencies near foF2 [*Rietveld et al.*, 2003].

The simulated airglow intensity at each wavelength was calculated by numerically integrating the respective photon volume emission rates from the lower to upper simulation boundaries. Again, it is not clear that this calculated column emission rate, expressed in units of rayleighs, is directly comparable to measurements of apparent surface brightness, also expressed in units of rayleighs. (These two units of measurement are equivalent only under a very specific set of circumstances, as mentioned in section 3.3). Artificial radio-induced aurora are richly structured, dynamic, and often do not even fill the field of view of the instrument. The comparison between model and measurement is especially unclear when the emissions from a wide range of altitudes extending hundreds of kilometers are significant, as opposed to being concentrated in a small range of altitudes.

4.1.1 Ionosphere critical frequency

No apparent significant difference was noted in calculated foF2 between corresponding simulations of the two experiments. Therefore, without loss of generality, only results from the simulated 17 March 2009 are shown here. Also, since no observations of O-mode HF modification at altitudes of 130 km altitude are available, those simulations conducted for model development purposes were not analyzed in detail.

Figure 13 shows the ionosphere critical frequency versus time for the simulated 17 March 2009 experiment with thermal electron heating applied at 250 km altitude near the F-region peak plasma density altitude (zmF2). The ionosphere critical frequency drops significantly during heating due to temperature-enhanced ambipolar diffusion which relaxes plasma density altitude gradients. Atomic oxygen ions are the principle ionic constituent in the F region and heating

increases diffusive flux up the geomagnetic field line where it can linger for several minutes to tens of minutes, and down the geomagnetic field line where it is destroyed through chemical reactions with the increasingly dense neutral atmosphere. The magnitude of the induced drop in foF2 decreases with decreasing altitude of the heat source due to increasing cooling by inelastic collisions and decreased electron thermal conductivity with decreasing altitude. The calculated dramatic drops in simulated foF2 due to electron heating is unphysical, however, since a drop in critical frequency below the (typically fixed) pump frequency will tend to arrest the HF-electron heating process. Therefore electron heating was not eliminated from consideration on the basis of foF2 effects alone. The simulations with the heat source applied at 150 km altitude did not converge due to excessive electron temperature altidue gradients. Also, the simulations with the maximum heat flux of 0.1 μW/cm^2 applied at 200 and 250 km altitude did not converge due to excessive electron temperature enhancements exceeding 10,000 K.

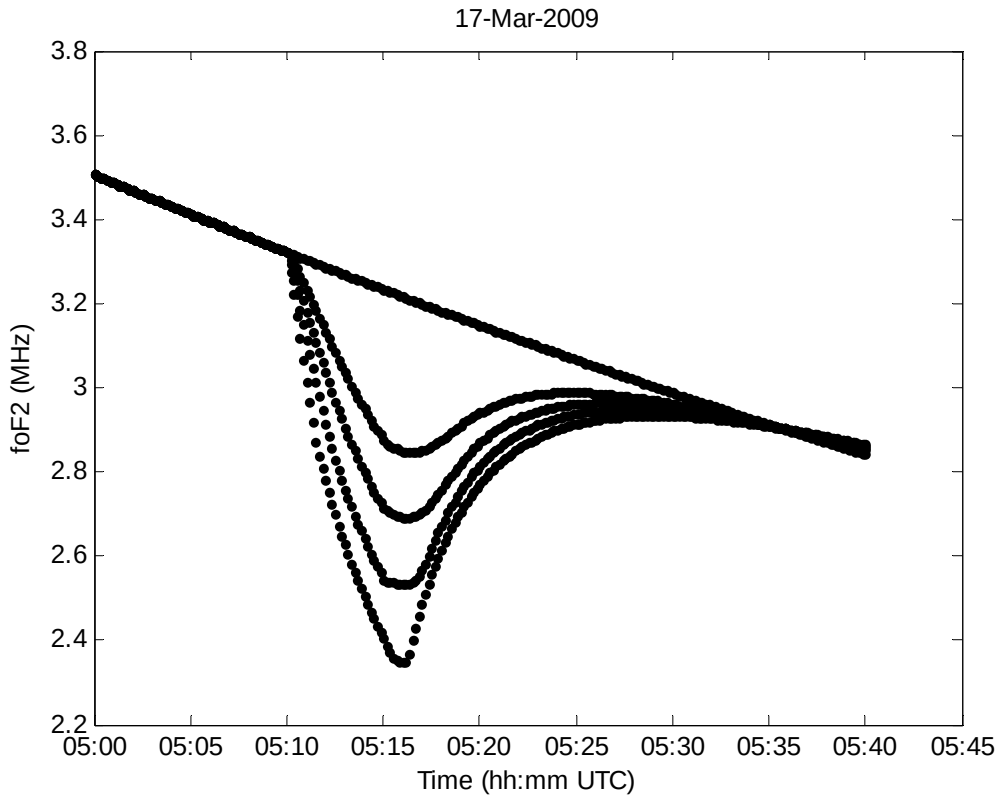

Figure 13. Calculated ionosphere foF2 response to thermal electron heating at 250 km altitude with 0.0000, 0.0018, 0.0050, 0.0136, and 0.0368 μW/cm^2 energy flux.

For the suprathermal electron acceleration simulations, the ionosphere modification as measured by foF2 varied with accelerated electron energy and volume number production rate. Sources that accelerated electrons to energies of 2.71 eV and 7.36 caused decreases in ionosphere foF2 similar in some aspects to the thermal heating simulations. This is expected

since both energies are beneath the ionization energies of the major neutral atmosphere constituent molecules. One notable difference between the low-energy acceleration simulations and the electron thermal heating simulations was that very little dependence on energy transfer flux was exhibited in the low-energy electron acceleration simulations. Otherwise, the decrease in foF2 was approximately 0.2 MHz below the (decreasing) background foF2 of approximately 3.2 MHz. The magnitude of the foF2 decrease resulting from 7.36 eV electron acceleration was even less than the 2.71 eV acceleration for equivalent choices of energy transfer flux. None of the 2.71 eV and 7.36 electron acceleration simulations were eliminated from consideration on the basis of foF2 effects.

Figure 14 shows the ionosphere critical frequency versus time for simulations of electron acceleration to 147.78 eV applied at 200 km altitude. The results are also generally representative of the 20.00 eV and 54.37 eV acceleration simulations. Significant increases in foF2 are apparent for large values of energy transfer flux, when significant numbers of electrons approach the F region peak density layer with energies exceeding the 8.32 eV ionization energy of atomic oxygen atoms. For low values of energy transfer flux applied at 200 km altitude, a small decrease in foF2 occurred because the effect from enhanced ambipolar diffusion via electron heating by elastic collisions with the accelerated suprathermal electrons was greater than ionization effects by the few suprathermal electrons capable of approaching the F-region peak density layer with energy greater than 8.32 eV.

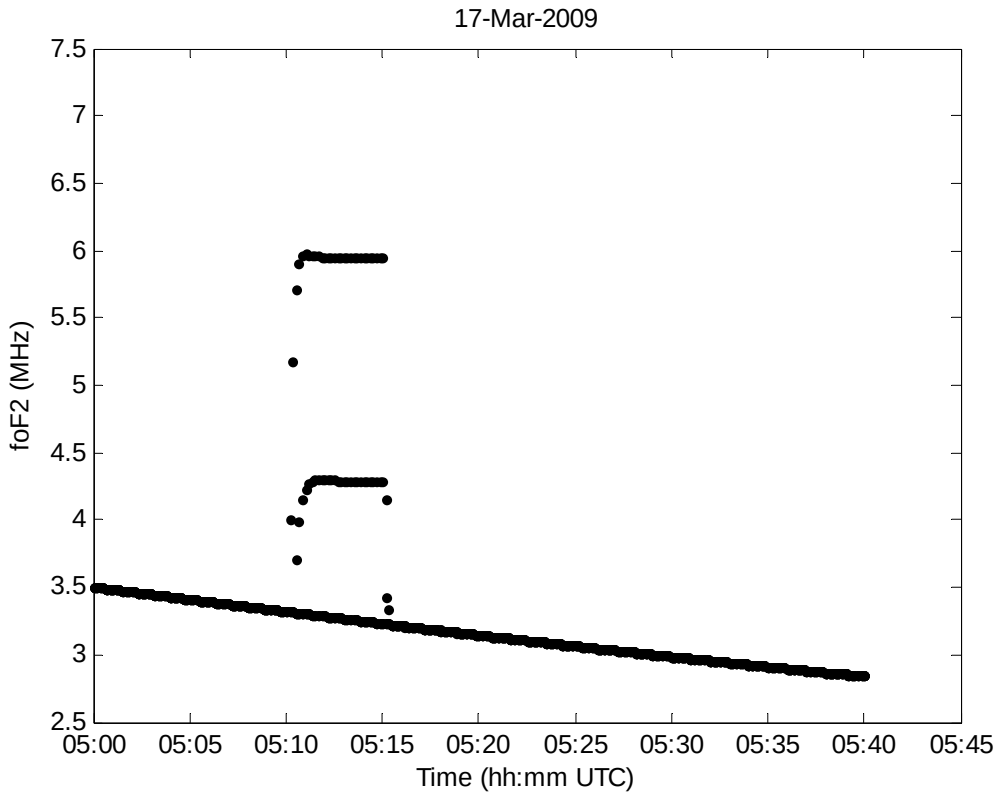

Figure 14. Calculated ionosphere foF2 response to suprathermal electron acceleration at 200 km altitude to 147.78 eV with 0.0000, 0.0018, 0.0050, 0.0136, 0.0368, 0.1000 μW/cm^2 energy flux. Only the two largest energy fluxes exhibited an increase in foF2, apparent in the image as step increases, while the 0.0136 μW/cm^2 flux simulation exhibited a small decrease in foF2.

Figure 15 shows that 147.78 eV electron acceleration sources applied at 150 km altitude, where the neutral atmosphere is relatively dense and has significant accelerated electron stopping power, can still result in detectable increases in foF2 provided sufficient total RF energy flux and associated accelerated electron production. On the basis of the calculated changes to foF2, the simulations with the largest two values of RF energy flux applied at 200 and 250 km altitude were eliminated, in addition to the simulation with the largest RF energy flux applied at 150 km altitude. Consequently, the only electron acceleration simulations considered potentially viable have sources between 0.0018 or 0.0136 μW/cm^2 flux applied at 200 or 250 km altitude, and sources with energy equal to or below 0.0368 μW/cm^2 flux applied at 150 km altitude. Recall that these values of available energy flux roughly correspond to 2% to 40% of the nominal RF energy flux at the center of the pump beam, traveling through a vacuum a distance of 200 km.

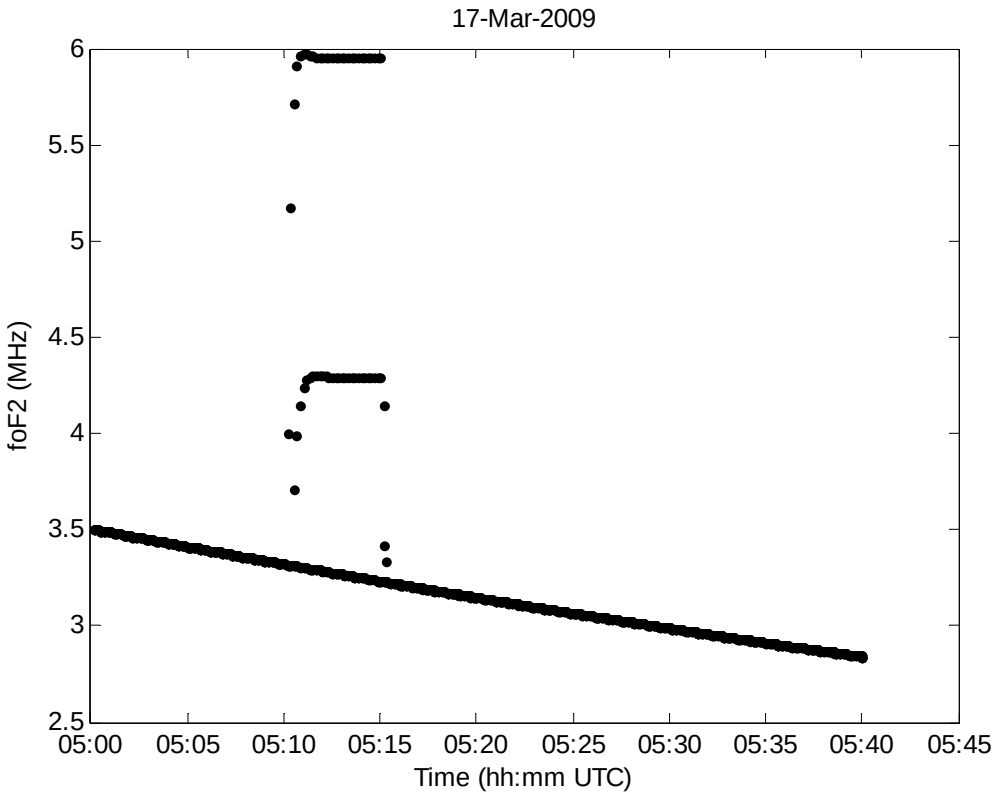

Figure 15. Calculated ionosphere foF2 response to suprathermal electron acceleration to 147.78 eV at 150 km altitude with 0.0000, 0.0018, 0.0050, 0.0136, 0.0368, 0.1000 μW/cm^2 energy flux. Only the two largest energy fluxes exhibited an increase in foF2, apparent in the image as step increases.

4.1.2 Photon column emission rates

Simulations that were not rejected due to unobserved artificial changes in ionosphere critical frequency foF2 were screened for cases where the column emission rate at 427.8 nm wavelength was approximately 20 R. Additional necessary criteria for selection were 557.7 nm column emission rates of approximately 500 to 1000 R and 630.0 nm emission rates of approximately 2000 to 3000 R. Simulations with calculated column emission rates that fell far outside these parameters were rejected from further consideration. The spectrographic apparent surface brightness time series measurements shown in Figure 16 reprinted from *Hysell et al.* [2014], provided the main foundation for comparison with the calculations of airglow column emission rates. A target of approximately 20 R column emission rates at 427.8 nm wavelength was also derived from estimates of apparent surface brightness reported by *Pedersen et al.* [2010].

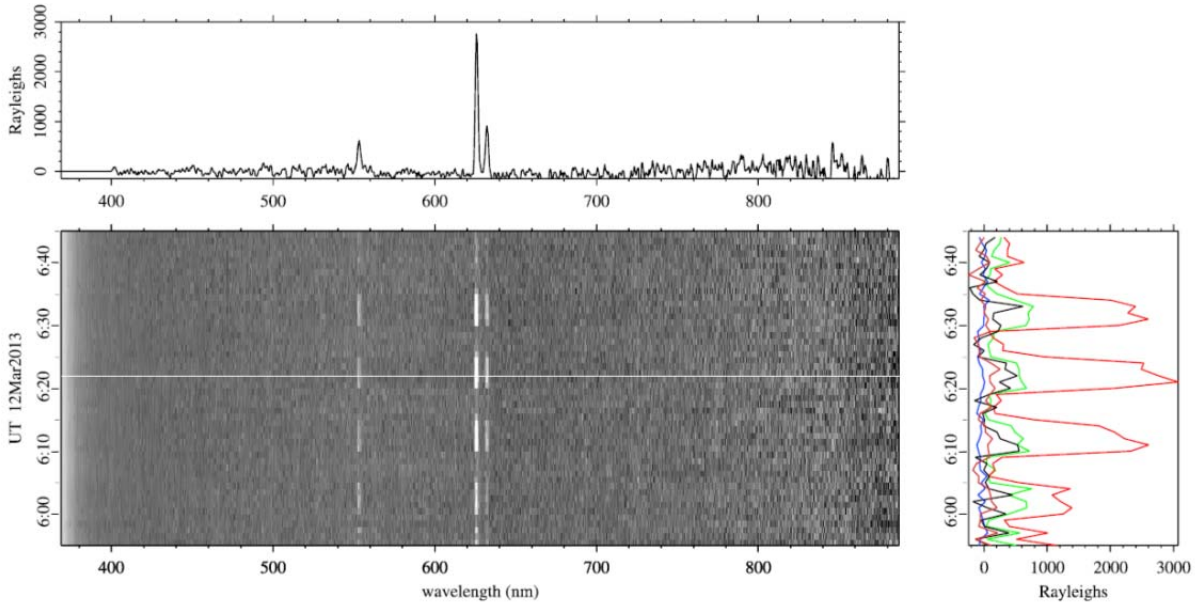

Figure 16. Measurements of apparent surface brightness of artificial aurora, reprinted from *Hysell et al.* [2014]. The right panel shows the time series of (blue) 427.8, (green) 557.7, (red) 630.0, and 844.6 nm wavelength brightness.

Figure 17 shows the first simulation of an ionosphere thermal electron heating experiment that resulted in a 16 R enhancement of 427.8 nm wavelength emissions without a suprathermal electron acceleration source [*C. T. Fallen and Watkins*, 2013a]. Subsequent heating simulations, including those conducted during this research, exhibited somewhat smaller 427.8 nm airglow enhancements. Figure 18 shows the calculated 427.8 nm wavelength airglow column emission rate during 250 km thermal electron heating at the maximum nominal heating rate of 0.1 $\mu W/cm^2$ for the 17 March 2009 HAARP experiment. This particular case maximizes the artificial 427.8 nm enhancement which is approximately 10 R or 100% greater than the background intensity. Since there is no significant enhancement in electron energy above the 18 eV ionization threshold of N_2^+, the cause of this 427.8 nm airglow enhancement is due solely to enhanced resonant scatter of sunlight by N_2^+ molecules lifted to higher altitudes. The intensity is comparable to the measured 427.8 nm emission and also follows the steady decrease in intensity due to increasing solar zenith angle that is comparable to that reported by *Pedersen, Gustavsson et al.* [2010]. This is somewhat less (approximately 50%) than the observed value but is still comparable to calculated 16 R blue line emissions for a simulated experiment on 15 November 2012 in Alaska that initially led to the discovery of the potential importance of resonant scatter of sunlight on the artificial 427.8 nm wavelength emission (see Figure 17) [*C. T. Fallen and Watkins*, 2013a; d]. However, two notable features may exclude this hypothesis from further consideration given current knowledge of ionosphere physics.

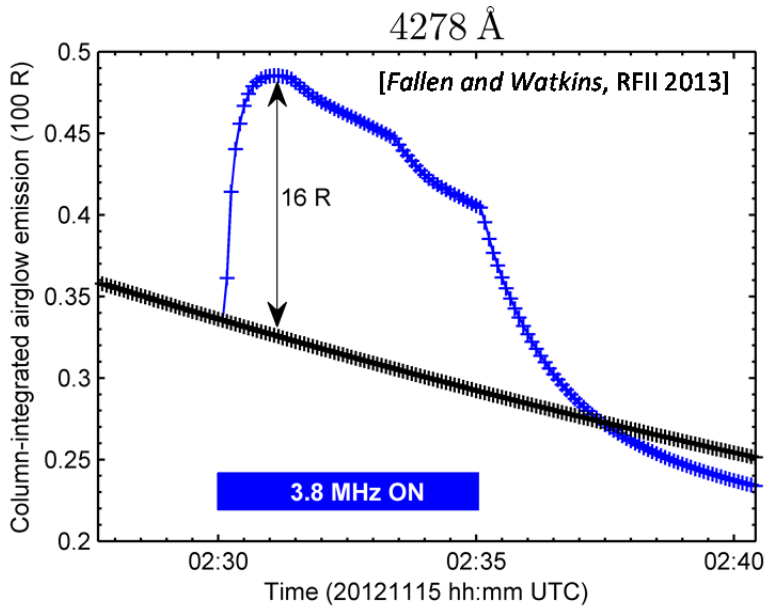

Figure 17. First calculation of significant 427.8 nm wavelength "blue line" emissions calculated for simulated thermal electron heating over Alaska.

First, extreme electron temperature enhancements of greater than 5000 K were calculated to extend hundreds of kilometers up the geomagnetic field line and this magnitude of electron temperature enhancement has not been measured and reported, at least not at EISCAT. While HAARP is a much more powerful HF transmitter than the EISCAT HF transmitter and no ISR measurements of electron temperature enhancements have been made at HAARP, there is no evidence yet that such temperature enhancements are reasonable. Second, the calculated 630.0 nm enhancements are enormous, nearly 50,000 R, which definitely have never been observed during any ionosphere radio modification experiment. The cause of the 630.0 nm enhancements is electron temperature-enhanced impact excitation of atomic oxygen to the 1D excited state ranging from the 250 km altitude HF-plasma interaction region to the top simulation boundary. This calculated enhancement may be an overestimate of the actual effect, even provided the electron heating location and available RF energy flux were accurate, as there are some indications that the electron thermal conductivity expression used in SCIM and other models may overestimate thermal conductivity at high altitudes in the high latitude ionosphere. Regardless, the 630.0 nm enhancement expected with such intense thermal electron heating at the F-region peak density height provides reason to eliminate this particular simulation hypothesis for the 17 March 2009 experiment.

Simulated thermal electron heating at 200 km altitude with a flux of 0.0368 $\mu W/cm^2$ (roughly 40% of the nominal RF energy flux available at HAARP) resulted in artificial 427.8 nm wavelength airglow enhancements of approximately 5 R, or 50% above the background value. The corresponding enhancements at 630.0 nm wavelength were 2500 R and no significant 557.7

nm wavelength enhancements were calculated. Under the assumption that observed radio-induced airglow can result from a combination of electron thermal heating and suprathermal electron acceleration, it is reasonable to suppose that, at least for the 17 March 2009 experiment at HAARP, up to 5 R of the observed artificial 427.8 nm wavelength emission can result from heated thermal electrons alone. This has important consequences for studies that use inversion techniques to estimate energetic electron distributions or ionization rates from the artificial 427.8 nm wavelength emission that assume electron impact ionization of N_2 is the sole source of 427.8 nm emissions [*Hysell et al.*, 2012; *Mishin and Pedersen*, 2011]. Thermal electron heating at 150 km altitude resulted in no significant 427.8 nm wavelength emission and only a modest 10 R enhancement of the 630.0 nm wavelength emission.

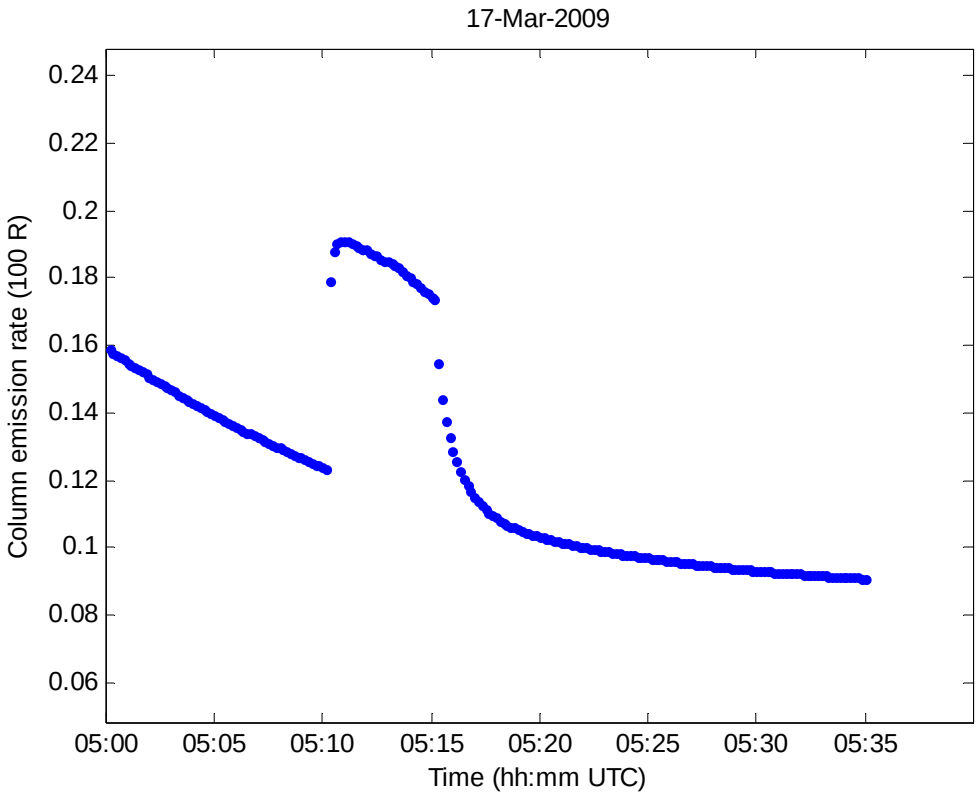

Figure 18. Calculated 427.8 nm wavelength column emission rates for nominal maximum thermal electron heating with 100 nW/cm^2 flux applied at 250 km altitude above Gakona, Alaska.

Simulations with a 2.71 eV suprathermal electron acceleration source at 250 km altitude produced a nearly 2 R enhancement of the 427.8 nm wavelength emissions in addition to a 30 R enhancement of the 630.0 nm emission (no enhancements of the 557.7 nm emission resulted). Again, this contribution to the artificial blue aurora is due to increased resonant scatter of sunlight since the electrons accelerated by the artificial source have energy far less than the required 18 eV ionization energy of N_2 molecules. This effect is not very sensitive to the

available energy flux. Consequently, any estimates of electron energy distributions based on spectroscopic measurements that do not account for resonant scatter of sunlight by N_2^+ ions lifted above the shadow height by temperature-enhanced ambipolar diffusion are over-estimating the acceleration rate of electrons with energy greater than ~20 eV. Sources that accelerate suprathermal electrons to 2.71 eV energy applied at 150 km altitude did not produce any significant changes in airglow at 427.8, 557.7, or 630.0 nm wavelengths.

Interestingly, the 7 eV suprathermal electron acceleration source did not significantly change the 557.7 nm wavelength emission when applied at any altitude or with any power flux. One explanation is that the electron impact cross section for excitation of the atomic oxygen O(1S) state peaks at approximately 10 eV and diminishes rapidly with energy to the 5 eV threshold. The overall effects on the airglow emissions at the three wavelengths considered here were similar to the effects resulting from a 2.71 eV suprathermal electron source.

When a 20 eV suprathermal electron acceleration source is applied, the approximate minimum energy required for 427.8 nm wavelength airglow emissions resulting from ionization of N_2 molecules, emissions at 557.7 nm and 630.0 nm are also present. The ratios of the column emission rates change with the altitude of the acceleration source. Also, the energy flux required to maintain a constant 427.8 nm wavelength column emission rate increases with decreasing altitude of the acceleration source. These two general characteristics are shared with the ionosphere responses to 54 and 148 eV suprathermal electron acceleration sources which are briefly reviewed in this section. However, there is little observational or theoretical evidence yet that supports the hypothesis that HF-plasma interactions have accelerated electrons to energies significantly greater than 20 eV.

Figure 19 shows the calculated airglow column emission rates resulting from a 20 eV suprathermal electron acceleration source applied at either 150, 200, and 250 km altitude. The available energy flux (applied uniformly over a 4 km thick layer) was held constant at 0.0050 $\mu W/cm^2$ and was chosen so that the calculated altitude dependence of the artificial 427.8 nm wavelength airglow enhancement approximately followed the time dependence exhibited by *Pedersen, Gustavsson et al.* [2010], assuming the source of the emissions descended from 250 km altitude to 150 km altitude. The altitude of the HF-enhanced ion line (HFIL) measured with the Modular UHF Ionosphere Radar (MUIR) co-located with the HAARP transmitter is believed to correspond with the source of accelerated electrons presumably responsible for artificial airglow emissions. Figure 20, reprinted from *Fallen* [2010] and adapted from *Pedersen, Gustavsson et al.* [2010], shows the altitude-dependence of the artificial 557.7 nm wavelength airglow intensity and the HFIL measured during the HAARP experiment conducted on 17 March 2009.

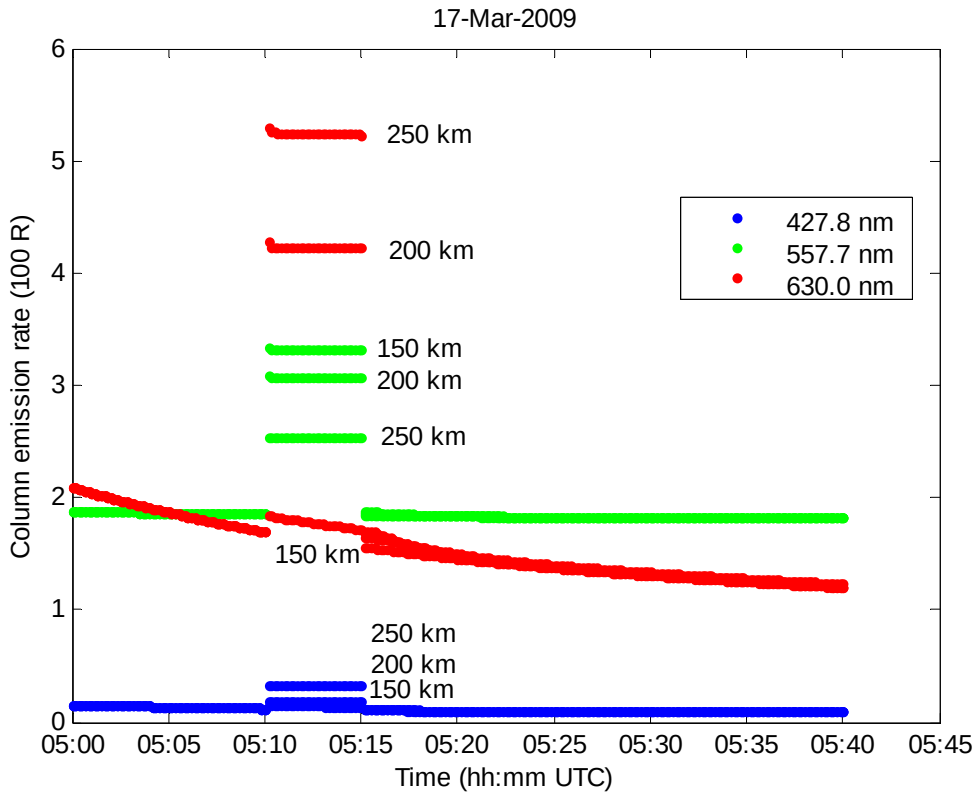

Figure 19. Airglow column emission rates versus time for an ionosphere modified by a 20 eV suprathermal electron source with 4 km thickness and 0.0050 μW/cm^2 of available energy flux, applied at 150, 200, and 250 km altitude above Gakona, Alaska between 0510 and 0515 hours UTC on 17 March 2009. The maximum 427.8 nm column emission rate, approximately 20 R, was obtained with a 250 km source.

The calculated enhancement of the 427.8 nm wavelength airglow column emission rate decreases from approximately 20 R at 250 km altitude to 7 R at 200 km, and then to 3 R at 150 km. Meanwhile, the enhancement of the 557.7 nm wavelength airglow column emission rate increases from approximately 70 R at 250 km altitude to 120 R at 200 km, and then to 150 R at 150 km. Finally, the enhancement of the 630.0 nm wavelength airglow column emission rate decreases from approximately 360 R at 250 km altitude to 250 R at 200 km, and then to 10 R at 150 km. The increase in the artificial 557.7 nm emission with decreasing altitude of the accelerated electron source is not surprising given that the number density of atomic oxygen atoms increases with decreasing altitude throughout the simulation domain. The decrease in the artificial 630.0 nm emission would generally be expected under the assumption that the source of accelerated electrons is descending with altitude. Curiously, the calculated time-dependence of the of the artificial 557.7 and 630.0 nm wavelength enhancements with changing source altitude are not apparent in the experiments reported by *Hysell, Varney et al.* [2012] and *Hysell, Miceli et*

al. [2014], including the 13 March 2002 experiment despite available MUIR measurements showing descent of the HFIL from 250 to 200 km altitude.

A suprathermal 54 eV electron acceleration source at 250 km altitude causes enhancements of the 427.8 nm wavelength airglow emission between approximately 10 and 30 R for energy fluxes between 0.0018 and 0.0050 μW/cm^2 (about 5% of the nominal available RF energy flux available at HAARP). However, enhancements in the 557.7 and 630.0 nm wavelength intensities range from 15 to 40 R and 85 R to 230 R, respectively. These values of energy flux are significantly less intense than measured values during experiments exhibiting a ~20 R airglow enhancement at 427.8 nm wavelength.

A 20 R enhancement in the 427.8 nm wavelength emission was calculated when the suprathermal 54 eV electron source is placed at 200 km altitude with energy flux of 0.0050 μW/cm^2. However, similar to the 250 km source, the calculated enhancements at 530.0 and 630.0 nm wavelengths of 80 and 180 R, respectively, are less than those observed during a comparable event with 20 R enhancements at 427.8 nm wavelength. If the source is moved down to 150 km altitude, then a flux between 0.0050 and 0.0135 μW/cm^2 causes enhancements of 10 to 30 R in the 427.8 nm wavelength emission with corresponding enhancements of 80 to 215 R and 10 to 20 R in the 557.7 and 630.0 nm wavelength emissions, respectively.

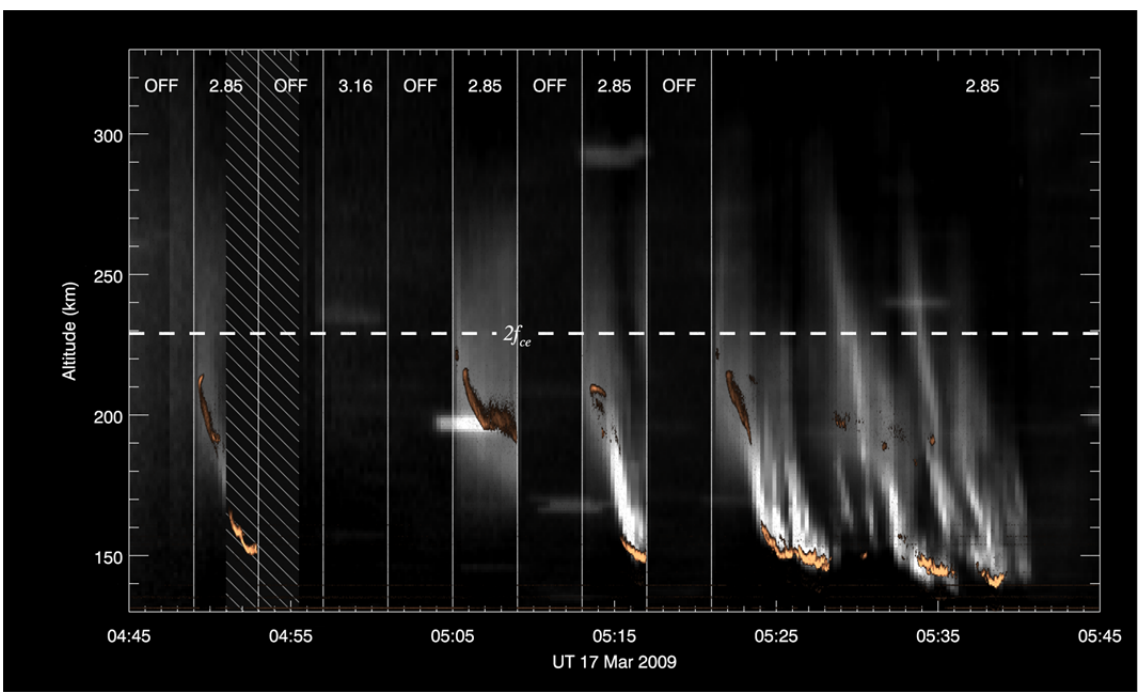

Figure 20. Field-aligned 557.7 nm airglow (white) and HF-enhanced ion-line intensity (copper) over the HAARP facility in Gakona, Alaska. A wide-field imager located about 160 km north of HAARP measured the airglow intensity. MUIR, collocated with HAARP, measured ion-line intensity.

Note that the intensity of the 630.0 nm emission maximizes when the electron acceleration source is applied at 200 km altidue rather than 150 or 250 km altitude. Part of this result is expected from theoretical arguments based on increased quenching of the 1D excited state of atomic oxygen. Curiously, this characteristic decrease of 630.0 nm wavelength emission with decreasing interaction altitude has not been reported, not even during experiments where the interaction altitude drops by approximately 50 km, presumably due to significant pump-induced ionization. Therefore the simulated 54 eV electron acceleration sources at 250, 200, and 150 km altitudes were rejected from further consideration.

Finally, the 148 eV suprathermal electron acceleration source yields airglow intensities broadly comparable to the 54 eV source at all altitudes and energy fluxes. Also, similar to the 54 eV source, the 557.7 and 640.0 nm wavelength column emission rates caused by the 148 eV suprathermal electron source are significantly less than the measured values when the available energy flux was set to 0.0050 $\mu W/cm^2$. This value was sufficient to produce an approximate 20 R enhancement in the 427.8 nm wavelength emission. Figure 21 shows the calculated column emission rates resulting from the 148 eV acceleration source placed at 250, 200, and 150 km altitudes with an available energy transfer flux of 0.0050 $\mu W/cm^2$.

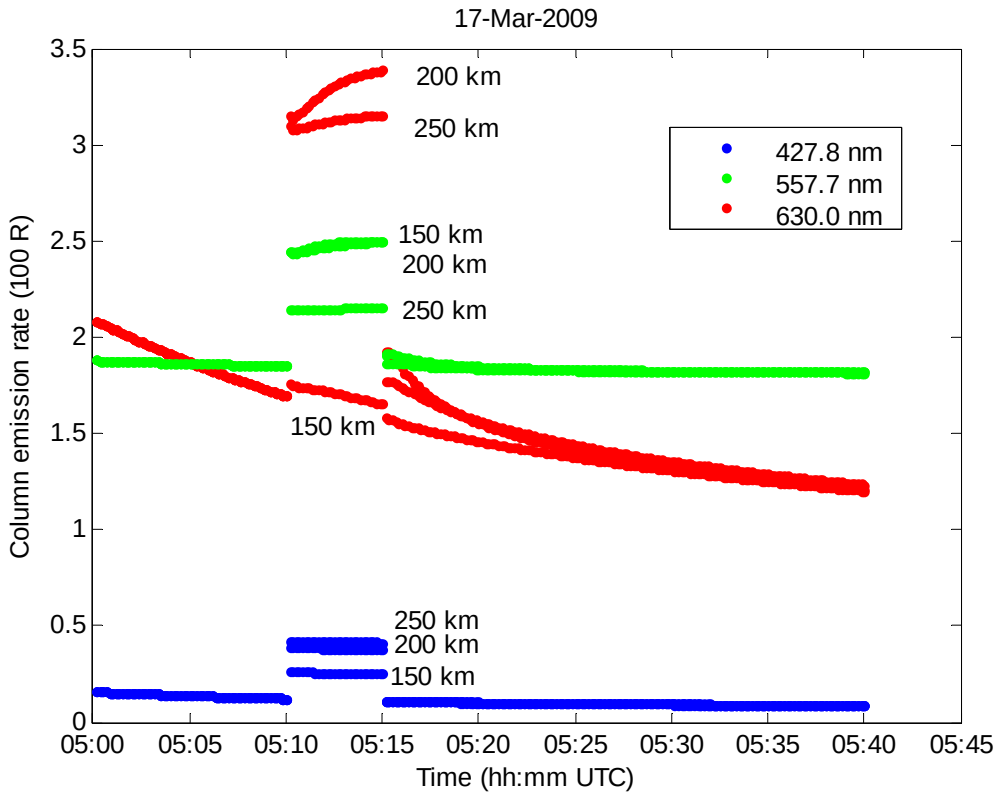

Figure 21. Airglow column emission rates versus time for a 147 eV suprathermal electron source of 4 km thickness with 0.0050 μW/cm^2 of available energy flux, applied at 150, 200, and 250 km altitude above Gakona, Alaska on 17 March 2009.

4.2 Altitude profiles

Altitude profiles of electron number density during simulated electron heating or acceleration can be used to further bound the hypothesized accelerated electron distribution. Given that the calculated time-dependent column emission rates shown in section 4.1.2 generally matched the surface brightness of artificial aurora created by HAARP, the choices of plotted altitude profiles of plasma density, plasma temperature, and airglow volume emission rates shown in sections 4.2.1 and 4.2.2 were generally restricted to the 20 eV electron acceleration.

The calculated plasma density profiles below the F-region peak density altitude were compared and validated with ionosonde measurements made at HAARP. In principle, plasma temperature calculations could also be validated provided ISR measurements, but no such measurements have ever been made at HAARP. Consequently, only rough comparisons can be made with EISCAT and, possibly, Arecibo measurements.

Very few side-view measurements of artificial aurora surface brightness exist so it is not yet possible to significantly validate the altitude profiles of calculated airglow volume emission

rates. However, the calculated altitude profiles are important to understanding the physical processes involved in the artificial aurora. The airglow volume emission rate calculations provide predictions that can be validated against side-view airglow measurements made during future ionosphere radio modification experiments. Altitude profiles of artificial airglow, particularly the 427.8 nm emission, provide a key indicator for the presence of artificially accelerated electrons. The presence of artificial 427.8 nm aurora alone is not necessarily sufficient to infer the presence of accelerated electrons.

4.2.1 Plasma density and temperature

Both ionosphere electron heating and electron acceleration are expected to change the plasma temperature and density along the geomagnetic field during radio modification experiments, based on theory and previous ISR measurements made at Arecibo and EISCAT. Electron heating can cause density increases or decreases, and sometimes both simultaneously, depending on the altitude where the heat source is applied. If the heat source is applied in the lower F region, then heating tends to decrease temperature-dependent molecular ion recombination rates which can lead to plasma density enhancements in the lower F region. If the heat source is applied near the F region peak density altitude, electron heating increases temperature-dependent ion ambipolar diffusion which leads to density decreases near the F region peak density layer and density increases in the topside ionosphere.

Figure 22and Figure 23 show the plasma temperature and density response, respectively, of the ionosphere above Gakona to electron heating with 5 nW/cm^2 flux at 150, 200, and 250 km altitude. The high-latitude ionosphere response to an artificial heat source has strong dependence on the altitude of the heat source. At low altitudes, collisions with neutral constituents provide a significant heat sink and also inhibit conduction of heat away from the source region. This is evident in Figure 22 as low altitude-heating produces a larger temperature enhancement that is more restricted in altitude range than heating with the same energy flux at high altitudes near the F-region peak density layer.

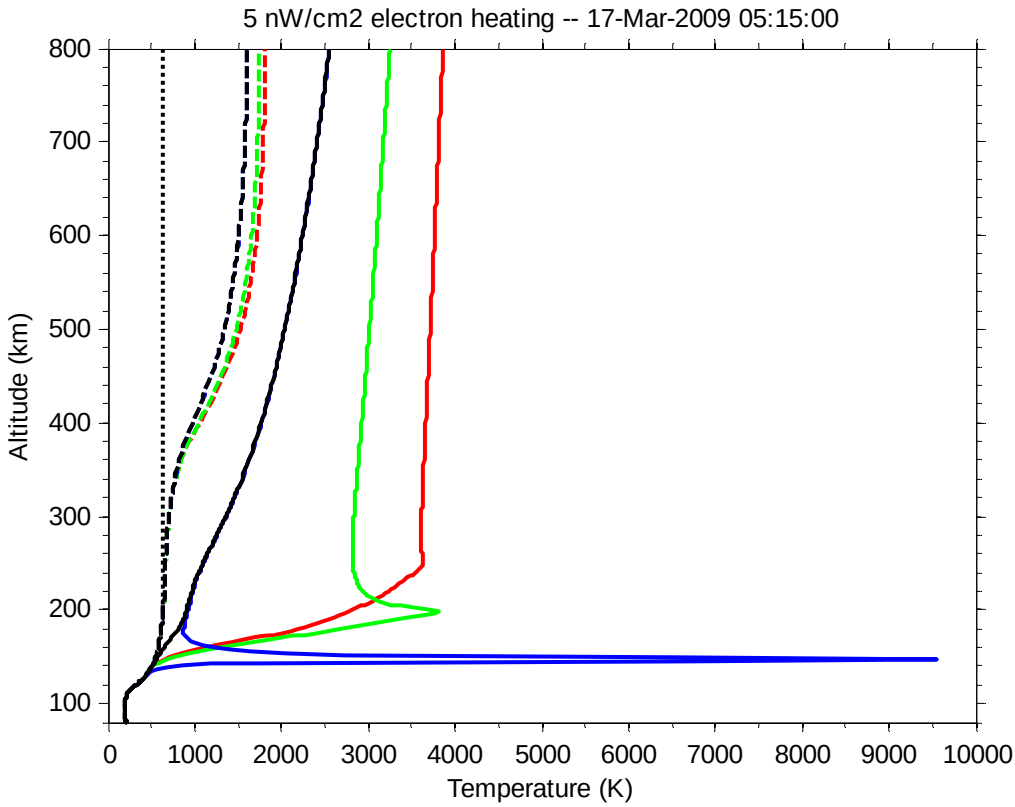

Figure 22. Calculated electron (solid), ion (dashed), and neutral (dotted) temperature profiles following 5 min of electron heating with 5 nW/cm^2 flux applied at 250 km (red), 200 km (green), and 150 km (blue). Black curves show the unmodified ionosphere.

The plasma density response to artificial thin-layer heating is also altitude dependent. Figure 23 shows that heating at higher altitudes, generally 200 km and above, results in depletion of the F-region peak density plasma. This effect has not generally been observed at HAARP with ionosonde or GPS slant TEC measurements. However, indirect measurements made with MUIR at HAARP are consistent with this depletion [*C. T. Fallen*, 2010] and a depletion of up to 20% have been reported from ISR measurements made at EISCAT [*Rietveld et al.*, 2003]. The depletion is caused by enhanced ambipolar diffusion that relaxes density gradients by enhancing diffusion of ions both up and down the field lines. Heating at lower altitudes such as 150 km, or sometimes even up to 250 km altitude also results in plasma density enhancements at lower altitudes. This effect results from decreased molecular ion recombination due to enhanced electron temperatures. Note that the plasma density enhancement from temperature-inhibited molecular ion recombination was found to be far less significant than the artificial layers measured with the HAARP ionosonde by *Pedersen et al.* [2010].

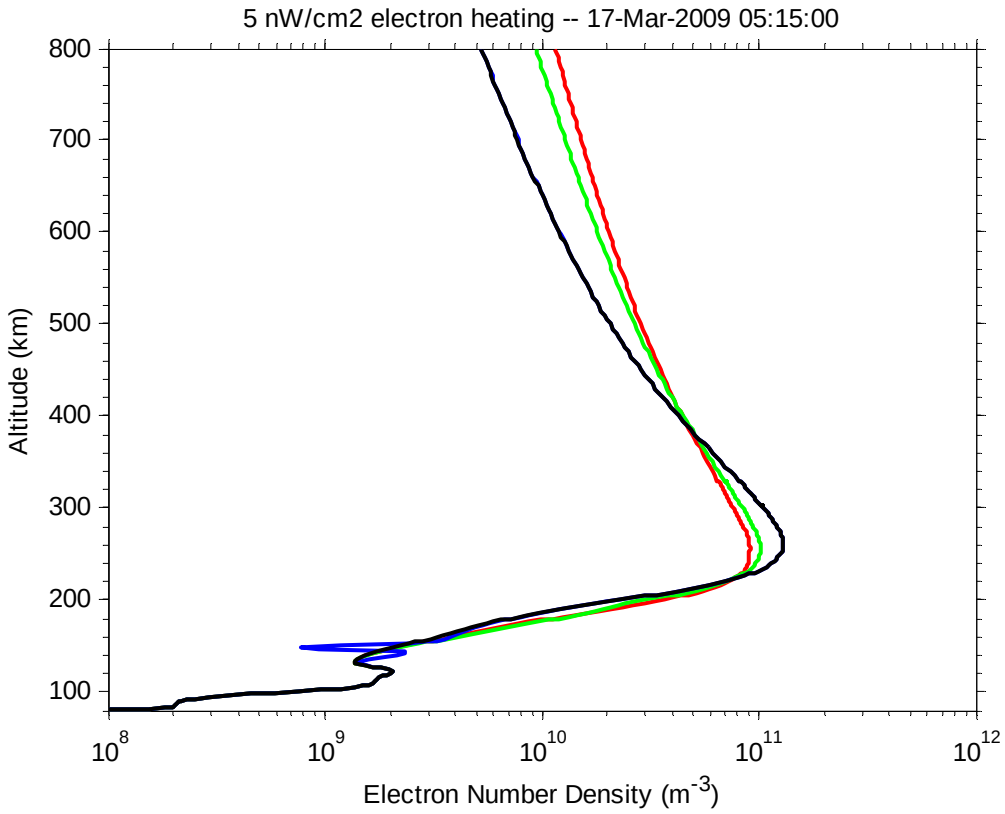

Figure 23. Calculated electron number density profiles after 5 min of electron heating with 5 nW/cm^2 flux applied at 250 km (red), 200 km (green), and 150 km (blue) altitude. The black curve shows the unmodified ionosphere.

Figure 24 shows the plasma temperature response at all power fluxes listed in Table 3, from 0 to maximum nominal electron heating with 100 nW/cm^2 flux, at 250 km altitude. The maximum flux of 100 nW/cm^2 flux was sufficient to generate artificial 427.8 nm wavelength airglow with comparable intensity to the brightest artificial airglow observed at that wavelength. The calculated electron temperatures, exceed any radio-modified ionosphere electron temperatures observed to date by at least a factor of 2. However, no ISR measurements of electron temperature have ever been made at HAARP, where the HF transmitter is more powerful transmitter than that at any other ionosphere heating facility, past or present.

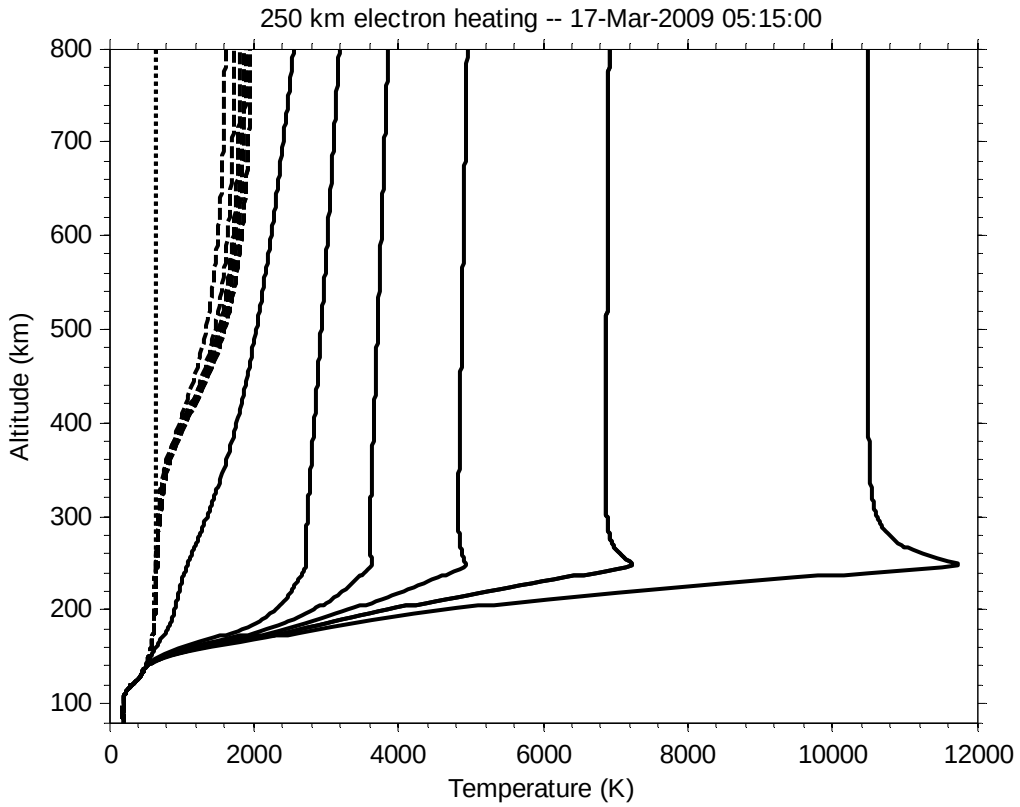

Figure 24. Calculated electron (solid), ion (dashed), and neutral (dotted) temperature profiles after 5 min of electron heating with 5 nW/cm^2 flux applied at 250 km altitude. The ion and electron temperature profiles are calculated for each power flux listed in Table 3, starting with 0 (leftmost respective curve) and ending with 100 nW/cm^2 (rightmost respective curve).

Since no ISR measurements have ever been made at HAARP, the only direct altitude-resolved plasma density measurements available have been made from the on-site Lowel DPS4D "Digisonde" ionosonde. Inferential measurements have been made at selected altitudes with the Modular UHF Ionosphere Radar (MUIR). Brief in-situ measurements have been made with spacecraft such as from the Defense Meteorological Satellite Program (DMSP) orbiting at approximately 840 km altitude. Scaled ionograms from the 17 March 2009 HAARP experiment, reprinted from *Pedersen et al.* [2010] in Figure 25, were used to determine which artificial accelerated electron production sources result in calculated ionosphere electron density profiles that closely match the scaled ionograms measured during the experiment.

The calculated plasma density and temperature profiles presented in this section were selected to illustrate the processes involved and certain limiting cases resulting from ionosphere modification by thermal electron heating at HAARP. The following plots of simulation results show the ionosphere response to electron acceleration sources for two distinct cases. First, results are shown for 20 eV electron acceleration sources with 5 nW/cm^2 energy flux applied at different

altitudes. The highest altitude source generates airglow column emissions that are generally consistent with measurements of apparent surface brightness of the artificial aurora made by *Pedersen et al.* [2010] or *Hysell et al.* [2012]. Second, results are shown for 20 eV electron acceleration sources that generate artificial plasma density enhancements that most closely match corresponding ionosonde measurements of plasma density shown in Figure 25.

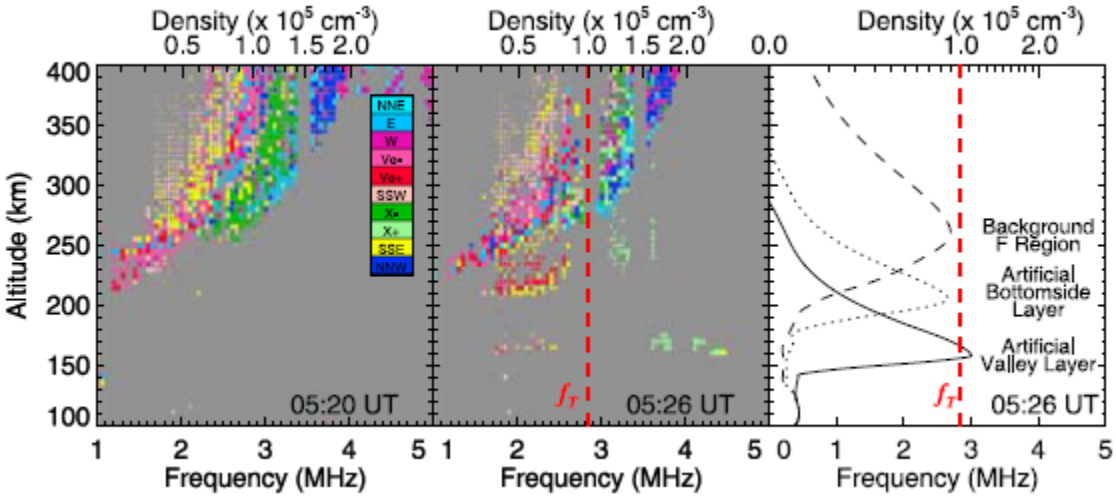

Figure 25. Ionograms before (left) and during (middle) heating with approximate scaling curves (right), reprinted from *Pedersen et al.* [2010], measured during the 17 March 2009 experiment at HAARP.

Figure 26 shows the plasma temperature response to a 20 eV electron acceleration source with 5 nW/cm^2 energy flux applied at 150, 200, and 250 km altitudes. Unlike artificial electron heating, the electron temperature enhancements due to electron acceleration decreases with decreasing altitude despite constant RF-plasma power transfer flux. Similar to electron heating, the affected region is generally smaller in altitude extent when the source is applied at lower altitudes than at higher altitude, though electron acceleration affects a larger region along the field line since accelerated high-energy electrons travel further between collisions than thermal or low-energy electrons due to decreasing collision cross section with increasing electron energy. Electron temperature enhancements are less than 1000 K for all cases, significantly less than the 3000 K or greater electron temperature enhancements believed to occur at HAARP. This would be consistent with substantial electron heating or low-energy electron acceleration effects occurring in addition to high-energy electron acceleration.

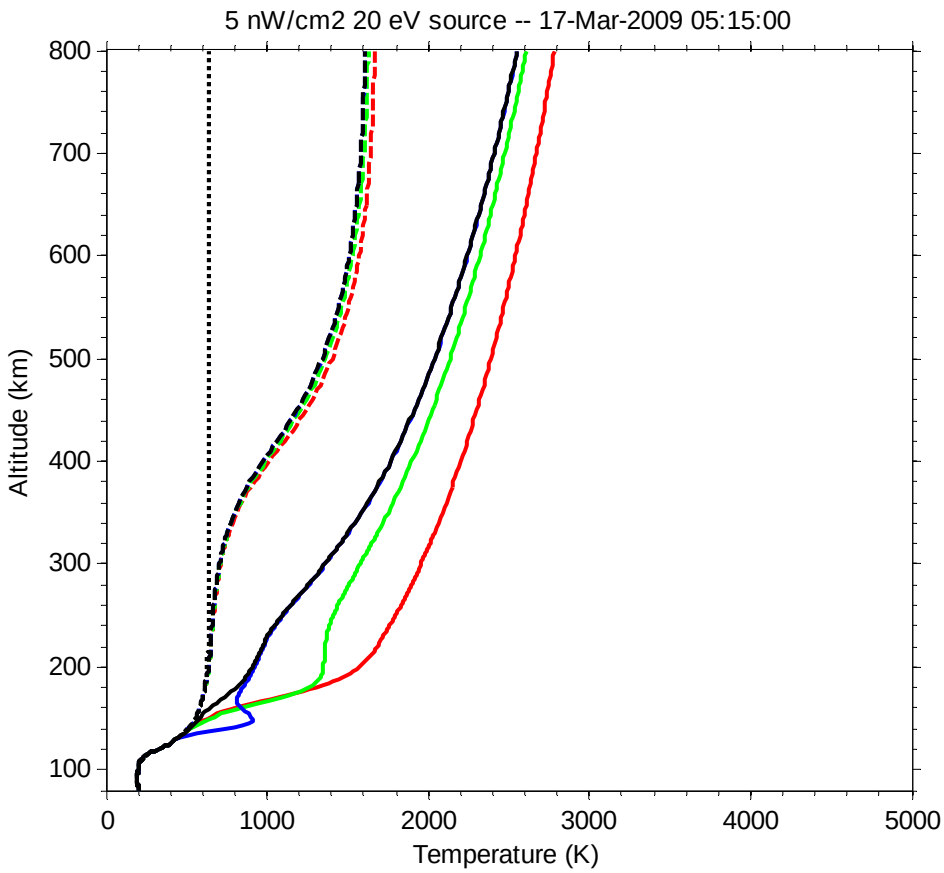

Figure 26. Calculated electron (solid), ion (dashed), and neutral (dotted) temperature profiles following 5 min of 20 eV electron acceleration with 5 nW/cm^2 flux applied at 250 km (red), 200 km (green), and 150 km (blue) altitude. Black curves show the unmodified ionosphere.

Figure 27 shows the plasma density response to a 20 eV electron acceleration source with 5 nW/cm^2 energy flux applied at 150, 200, and 250 km altitudes. In an absolute sense, the plasma density response is not significantly altitude dependent despite apparent differences in the density profiles of ionospheres modified by electron acceleration sources placed at different altitudes. In each case, however, the plasma density enhancement is approximately 3×10^{10} m^{-3} but is only apparent at lower altitudes where the background electron density is comparable or less in magnitude to the enhancement and is more readily apparent on the logarithmic scale of the plot axis. None of the three cases result in plasma density enhancements or "layers" observed in the ionosonde data.

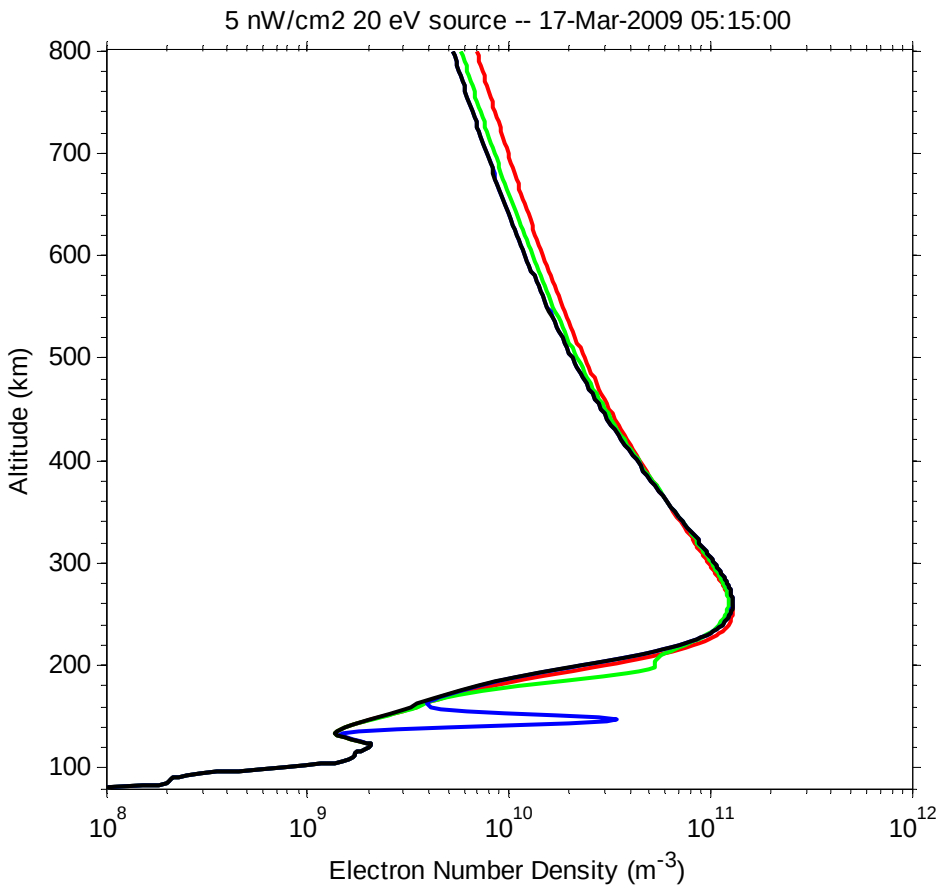

Figure 27. Calculated ionosphere electron number density profiles after 5 min of 20 eV electron acceleration with 5 nW/cm^2 flux applied at 250 km (red), 200 km (green), and 150 km (blue) altitude. The black curve shows the unmodified ionosphere.

The resulting catalog of simulated ionosphere density profiles were searched to find the cases where 20 eV electron acceleration sources produced plasma density enhancements that most closely matched the artificial "layers" apparent in the scaled ionograms (Figure 25) measured during the HAARP experiment on 17 March 2009. Calculated plasma density results from two separate simulations illustrated in Figure 28 show calculated artificial layers that were in good agreement with the scaled ionograms. The simulations both used 20 eV electron acceleration sources, one with 13.5 nW/cm^2 flux applied at 200 km altitude and the other with 36.8 nW/cm^2 flux applied at 150 km altitude. In principle, a third 20 eV source at 250 km altitude also could have been included without much apparent effect on the calculated plasma density profile. As shown in Figure 27 the resulting relative density change from a 5 nW/cm^2 flux at 250 km is minimal and would not likely be measurable with the ionosonde.

Diffusion is not an effective ion transport mechanism near 150 km altitude so the superposition of the two modified ionosphere density profiles illustrated in Figure 28 is a

reasonable representation of an ionosphere modified by two electron acceleration sources applied at 150 and 200 km altitude. The side view tomographic reconstruction of 557.7 nm airglow emissions, reprinted in Figure 29 from *Pedersen et al.* [2010], provides optical evidence that ionosphere radio modification can have rich structure and may be composed of multiple "sources" of heating and election acceleration (or other modification effects). In light of the airglow tomographic reconstruction in Figure 29, the different values of accelerated electron flux used to bring the simulated enhanced ionosphere plasma density layers into agreement with the ionosonde measurements are reasonable for two reasons. First, the "$1/r^2$" dependence of free space radio frequency energy flux suggests greater flux at lower altitudes than higher altitudes. Second, the apparent higher altitude "donut" optical structure has a radius from beam center of approximately 20 km, a significant fraction of the beam width at that altitude so the radio frequency energy flux is expected to be significantly less than at the beam center.

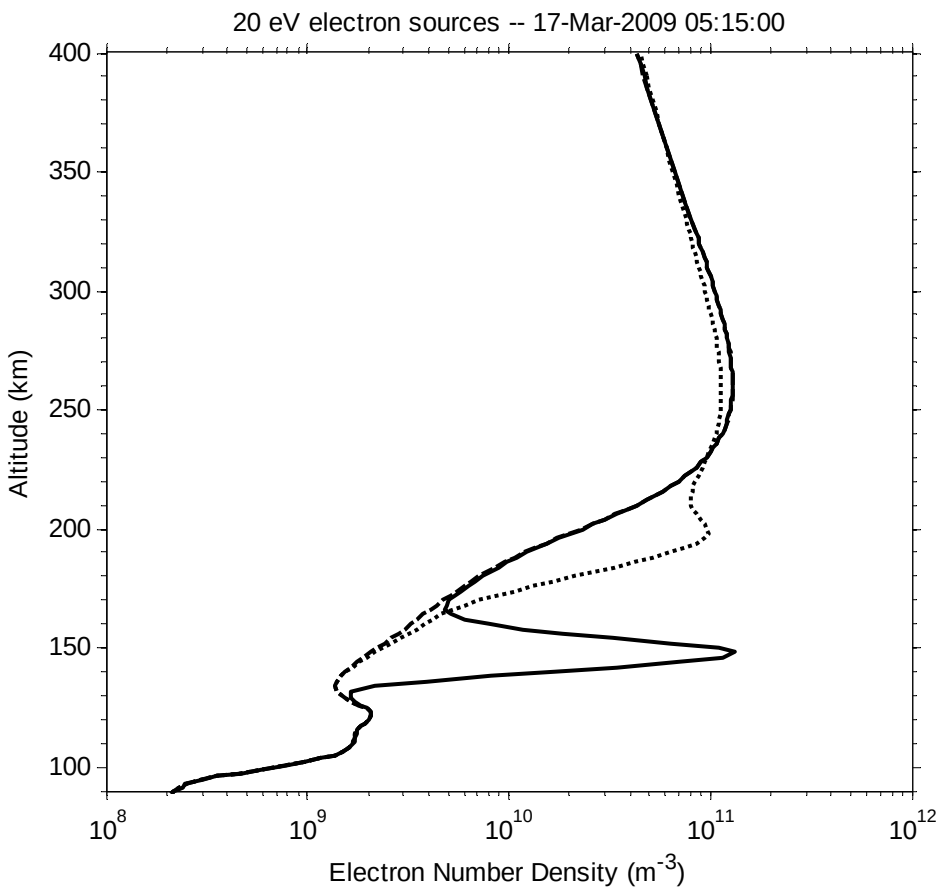

Figure 28. Calculated ionosphere electron number density profiles after 5 min of 20 eV electron acceleration with 13.5 nW/cm^2 flux applied at 200 km (dotted) and 36.8 nW/cm^2 flux applied at 150 km (solid) altitude. The dashed curve shows the unmodified ionosphere. The power levels were chosen to result in ionosphere plasma density profiles that correspond to the scaled ionograms illustrated in the right panel of Figure 25.

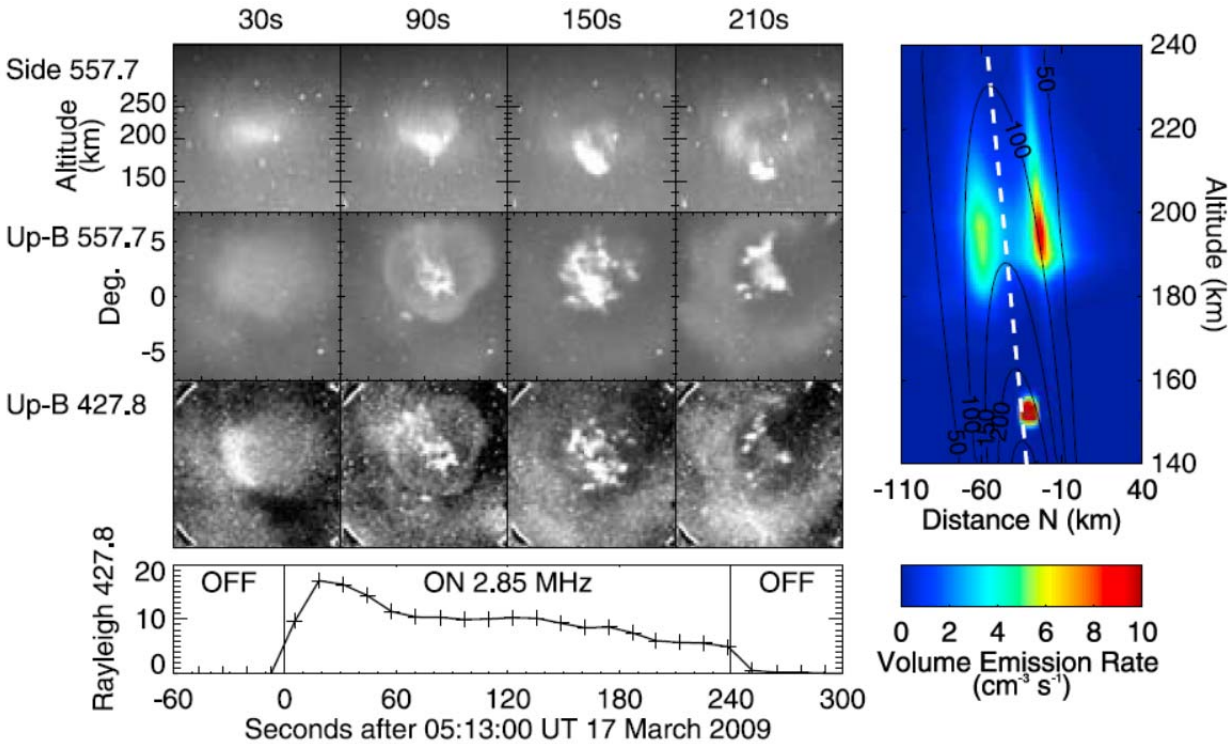

Figure 29. Reprinted images from *Pedersen et al.* [2010] showing (top left) images of artificial airglow at 557.7 and 427.8 nm wavelengths at HAARP, (bottom left) time variation of average 427.8 apparent surface brightness, and (right) tomographic reconstruction of estimated enhancements to 557.7 nm wavelength volume emission rates at 210 s into the HF transmitter 'ON' cycle.

4.2.2 Photon volume emission rates

Photon volume emission rates were calculated as functions of altitude and time. As shown in section 4.1.2, the simulated radio-modified photon column emission rate enhancements relative to the background values were largely independent of time and this was also generally true of the volume emission rates. The background volume emission rates and column emission rates (volume emission rates integrated with respect to distance along the magnetic zenith) typically decrease with time in the evenings, the time of most ionosphere radio-induced aurora experiments, as the solar zenith angle increases. The plots in this section show calculated altitude profiles of 427.8, 557.7, and 630.0 nm wavelength volume emission rates at 05:15 hours UTC on 17 March 2009 following five minutes of simulated radio modification. The plots also show the respective background unmodified volume emission rates at 05:15 UTC.

Artificial electron heating is not sufficient to cause artificial 427.8 nm wavelength airglow through direct electron impact ionization of N_2 molecules. However, field-aligned conduction of electron heat causes redistribution of ionosphere plasma through enhanced ambipolar diffusion which can result in enhanced N_2^+ ion densities at higher sunlit altitudes which in turn causes enhanced 427.8 nm emissions through resonant scatter of sunlight. Figure 30 shows calculated

427.8 nm airglow volume emission rate altitude profiles of the background ionosphere and the modified ionosphere resulting from a 100 nW/cm^2 flux electron heat source applied at 250 km altitude. In this case, the majority of artificial 427.8 nm airglow occurs above 300 km altitude. Significant high-altitude 630.0 nm airglow enhancements and minor changes to the 557.7 nm wavelength emission profile (not shown) also occur. This calculation represents the maximum expected 427.8 nm airglow enhancement due to thermal electron heating by high-power radio waves. Also, this result is generally representative of ionosphere modification via low-energy (less than 20 eV) artificial electron acceleration. Note that electron thermal conductivity decreases with decreasing altitude so artificial 427.8 nm emission rates also decrease as the artificial electron heat source is moved to lower altitudes.

Electron acceleration to energies of 2.71 and 7.36 eV resulted in modest calculated 427.8 nm emissions qualitatively similar to the electron heating case. As those electron energies are less than the 18.1 eV ionization threshold for impaction ionization of N_2 molecules and subsequent first negative band emissions from excited state N_2^+ ions, the mechanism is also attributed to enhanced resonant scatter of sunlight due to N_2^+ ions lifted to higher sunlit altitudes through plasma heating by elastic collisions with suprathermal electrons. As noted in section 4.1.2, the calculated enhancement in 557.7 nm airglow emissions was insignificant for 7.36 eV accelerated electron heating and this is likely because the O(^{1}S) impact excitation cross section peaks at approximately 10 eV and decreases sharply for energies below that value.

Calculated airglow volume emission rates resulting from accelerated electrons generally are maximized near but not necessarily within the electron acceleration region. Figure 31 shows 427.8, 557.7, and 630.0 nm wavelength volume emission rates calculated for both the background ionosphere at 05:15:00 UT and the modified ionosphere after a source of 20 eV accelerated electrons with 5 nW/cm^2 flux was applied at 250 km altitude for a duration of 300 s. The following Figure 32 and Figure 33 show the corresponding volume emission rates for the same artificial electron source applied at 200 and 150 km altitude, respectively. The three plots illustrate the altitude variation of airglow volume emission rates responsible for the integrated column emission rates shown in Figure 19. In particular, the plots demonstrate that the 557.7 nm wavelength emission intensity increases with decreasing source altitude, for the same power flux, while both the 427.8 and 630.0 nm emissions decrease significantly in intensity with decreasing source altitude. These characteristics should be apparent in artificial aurora experiments at HAARP, such as those described by *Hysell et al.* [2014], where the presumed accelerated electron source region, as indicated by radar, descends from approximately 250 to 200 km altitude during several minutes of radio modification. However, the observed airglow intensities, except perhaps the 630.0 nm emission, did not apparently show this expected variation throughout each modification cycle.

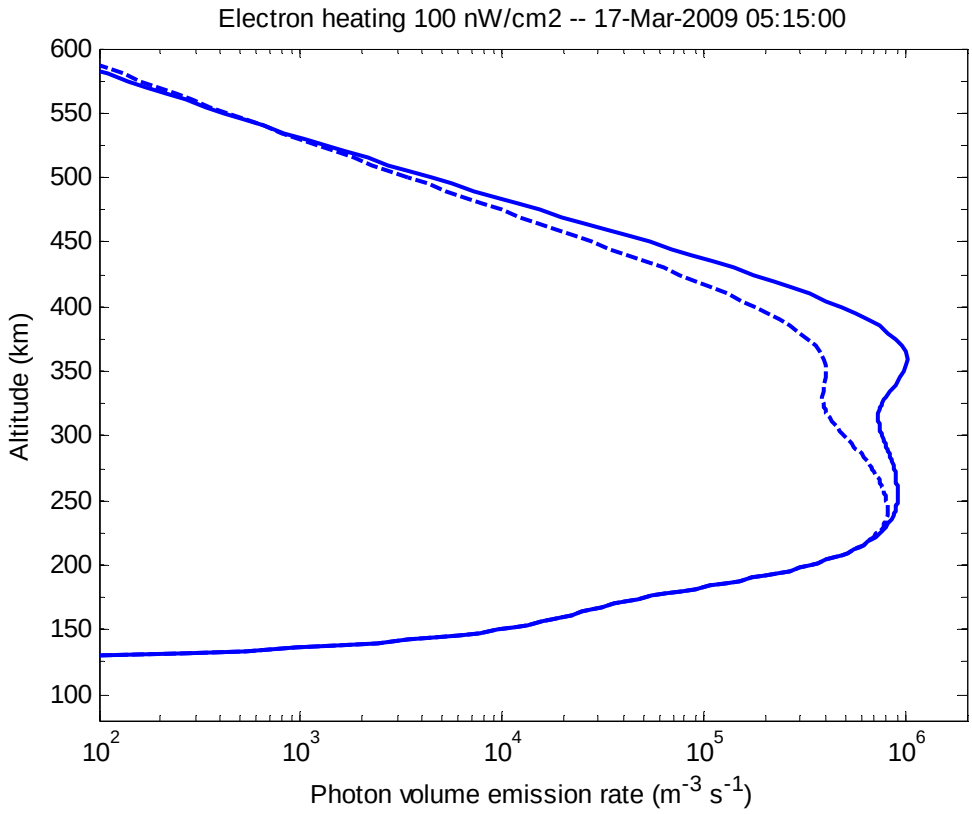

Figure 30. Calculated natural (dashed) and artificial (solid) 427.8 nm wavelength airglow volume emission rates. The artificial airglow emission is calculated for electron heating at 250 km altitude.

Figure 31 clearly shows that the calculated airglow emission enhancements at all calculated wavelengths occur over a broad range of altitudes extending hundreds of kilometers from the source at 250 km altitude. This occurs in part because accelerated electrons can travel greater distances between collisions with the neutral atmosphere at higher altitudes. In the case of the 630.0 nm emission, collisional quenching of the $O(^1D)$ excited state is minimized at higher altitudes. In the case of the 427.8 nm emission, resonant scatter of sunlight by lifted and newly created N_2^+ ions is still a significant contributing mechanism. Figure 32 shows that as the accelerated electron source was lowered to 200 km altitude, airglow enhancements were confined to a much narrower altitude region surrounding the source due to reduced travel distance of the accelerated electrons. The 630.0 nm emission decreased in total intensity because of increased quenching at lower altitudes and the 427.8 nm emission decreases in total intensity because increased collisions between the accelerated electron population and other constituent gasses immediate decrease the fraction of accelerated electrons with energies above the ionization threshold of N_2 molecules. The 427.8 nm emission also decreased because of reduced resonant scatter of sunlight at higher altitudes.

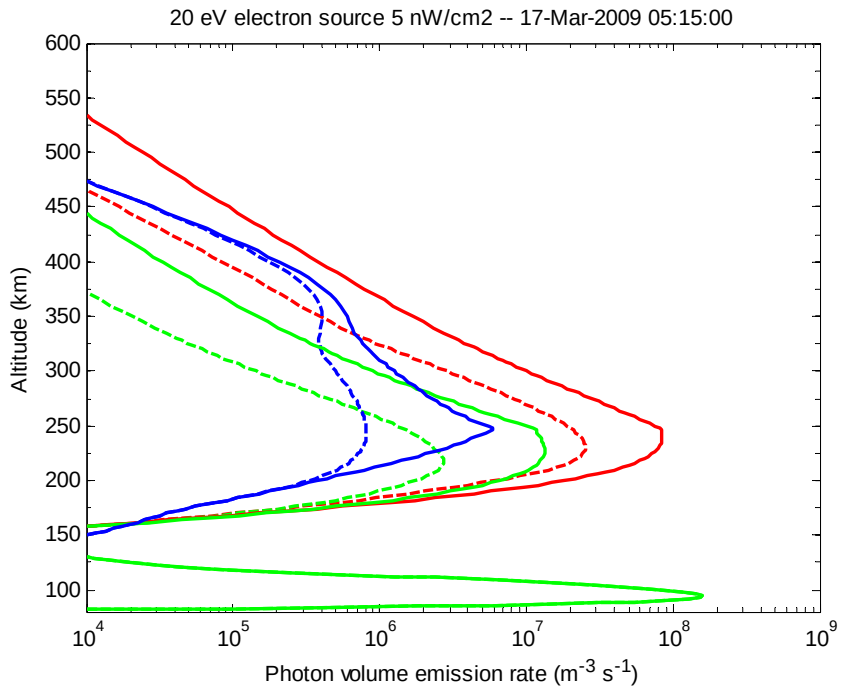

Figure 31. Calculated natural (dashed) and artificial (solid) airglow volume emission rates at (blue) 427.8 nm, (green) 557.7 nm, and (red) 630.0 nm wavelengths. The artificial airglow emission is calculated for electron acceleration to 20 eV energy with 5 nW/cm^2 flux at 250 km altitude.

Finally, Figure 33 shows that calculated airglow emissions were sharply peaked at the 150 km accelerated electron source region. The 557.7 nm emission was clearly the most intense, particularly over the 427.8 emission, due to the relatively low excitation energy of O(^{1}S) atoms relative to the impact ionization threshold energy of N_2 molecules. Accelerated electrons quickly lost energy through impacts with a greater number of neutral atmosphere constituents, so a greater fraction of accelerated electrons were available to excite the O(^{1}S) atomic state than to ionize N_2 molecules. The 630.0 nm emission was suppressed, as expected, due to significant quenching of the O(^{1}D) excited state. However, this calculated significant decrease in 630.00 nm apparent intensity with time has not been reported, even during experiments when the HF-plasma interaction source is observed with radar to descend 10s of kilometers altitude. One possible explanation is that the HF-plasma interaction region has rich spatial structure extending 50 km or more along the geomagnetic field line. *Pedersen et al.* [2010] provides some evidence of this structure, reprinted in Figure 29.

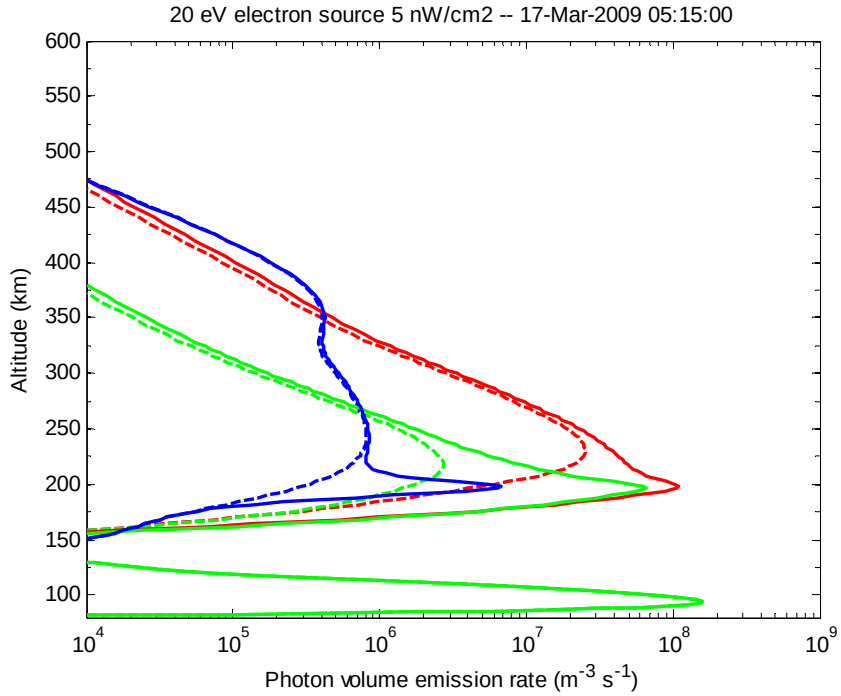

Figure 32. Calculated natural (dashed) and artificial (solid) airglow volume emission rates at (blue) 427.8 nm, (green) 557.7 nm, and (red) 630.0 nm wavelengths. The artificial airglow emission is calculated for electron acceleration to 20 eV energy with 5 nW/cm^2 flux at 200 km altitude.

The electron density effects from two 20 eV electron acceleration sources with two different energy fluxes, 13.5 nW/cm^2 at 200 km altitude and 36.8 nW/cm^2 at 150 km altitude, were reconstructed as shown in Figure 28 to simulate and match the artificial layers shown in Figure 29 measured reprinted from *Pedersen et al.* [2010]. The resulting airglow column intensity enhancements were calculated to be 31 R at 427.8 nm, 1300 R at 557.7 nm, and 2700 R at 630.0 nm wavelengths. These enhancements are 220%, 870%, and 440% greater than the the background values, respectively. The absolute enhancements generally agreed well with the measurements reported by *Pedersen et al.* [2010] given the experimental uncertainties involved.

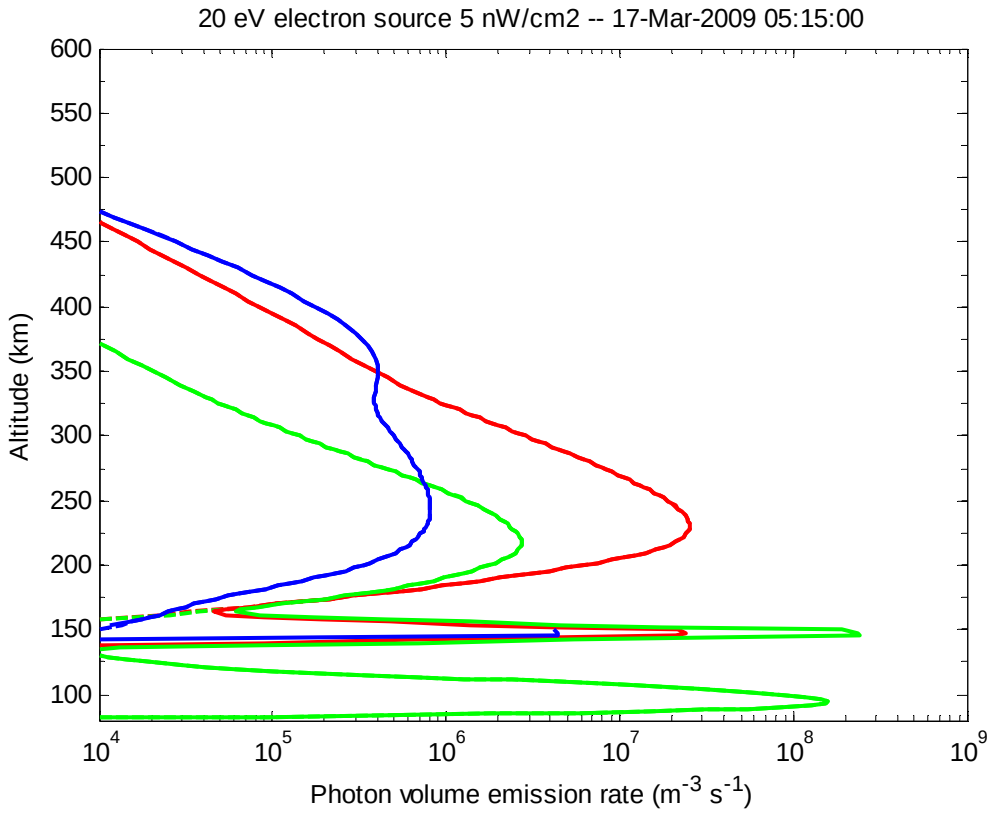

Figure 33. Calculated natural (dashed) and artificial (solid) airglow volume emission rates at (blue) 427.8 nm, (green) 557.7 nm, and (red) 630.0 nm wavelengths. The artificial airglow emission is calculated for electron acceleration to 20 eV energy with 5 nW/cm^2 flux at 150 km altitude.

Resulting calculated altitude-resolved airglow volume emission rates are shown in Figure 34 and Figure 35 for the 20 eV 13.5 nW/cm^2 flux source applied at 200 km altitude and for the 20 eV 36.8 nW/cm^2 flux source applied at 150 km altitude, respectively. The airglow volume emission rates were qualitatively consistent with the prior calculations, with greater emission rates corresponding to greater applied power fluxes, and higher altitude sources creating artificial airglow at a greater range in altitudes surrounding the source, as expected. In particular, these properties of the simulated bi-altitude electron acceleration source appear to be in good agreement with the side-view 557.7 nm airglow measured by *Pedersen et al.* [2010]. Unfortunately, few side-view measurements of radio-induced aurora have been made that would invite more substantial comparison of theoretical and observational results.

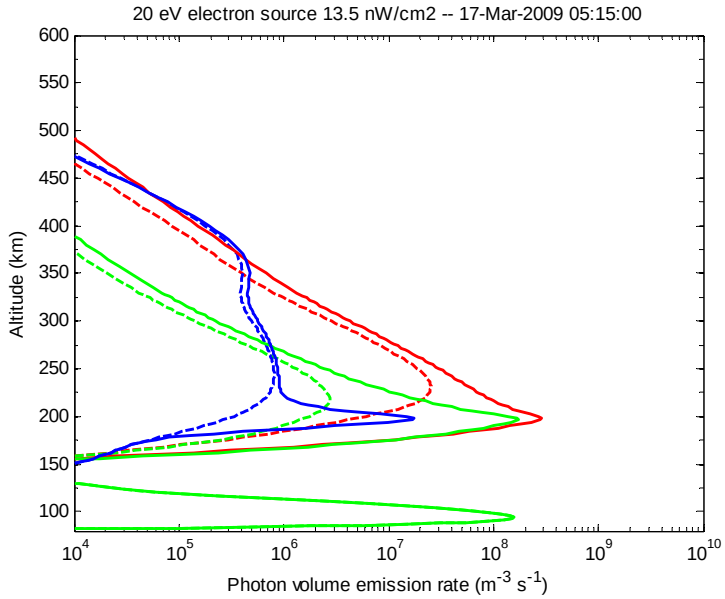

Figure 34. Calculated natural (dashed) and artificial (solid) airglow volume emission rates at (blue) 427.8 nm, (green) 557.7 nm, and (red) 630.0 nm wavelengths. The artificial airglow emission was calculated for a 20 eV electron acceleration source with 13.5 nW/cm^2 flux applied at 200 km altitude.

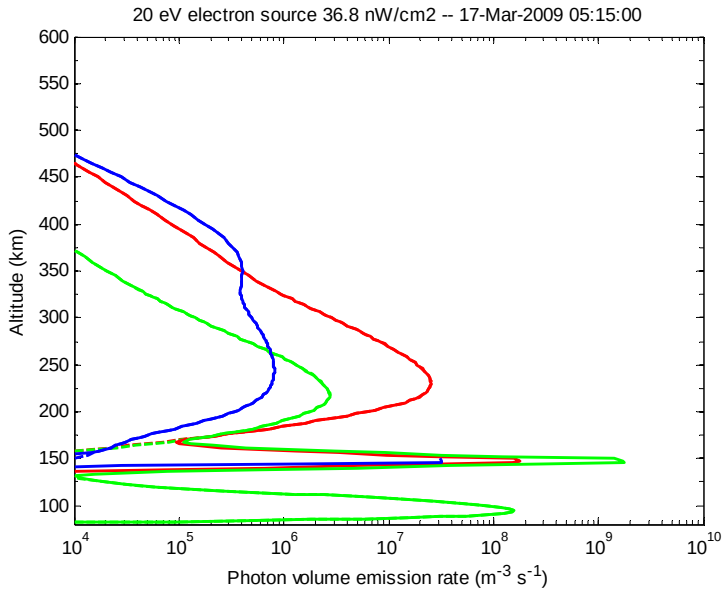

Figure 35. Calculated natural (dashed) and artificial (solid) airglow volume emission rates at (blue) 427.8 nm, (green) 557.7 nm, and (red) 630.0 nm wavelengths. The artificial airglow emission is calculated for electron acceleration to 20 eV energy with 36.8 nW/cm^2 flux at 150 km altitude. The enhanced green line emission rate at 150 km altitude is approximately a factor of 10^7 larger than the background value at that altitude.

4.3 Discussion

For a given fixed-altitude source of accelerated electrons placed between 150 and 250 km altitude it is clearly possible, either through an ad hoc inversion process such as the one used in this project or through a more mathematically rigorous inversion processes used by *Hysell et al.* [2012] and *Hysell et al.*[2014], to construct a continuous electron production energy distribution that results in airglow emissions that match observations reasonably well. However, when the spatiotmporal variation of the HF-plasma electron acceleration source is included in model calculations, it is much more difficult to reach agreement between model calculations and observations. None of the simulated ionosphere column airglow emission rates resulting from an artificial thermal electron heat source or suprathermal mono-energetic electron acceleration source accurately reproduced the measured apparent surface brightness of the corresponding artificial aurora created at HAARP, at least not at the source altitudes considered.

The 20 eV suprathermal electron acceleration source was sufficient to generate arbitrary 427.8 nm column emission rates when applied at any altitude under consideration simply by modifying the available energy flux. The resulting 557.7 and 630.0 nm column emission rates were significantly less than those measured and calculated by [*Hysell et al.*, 2012] and [*Hysell et al.*, 2014], but could in principle be accounted for by adding additional lower-energy suprathermal electron acceleration sources and a thermal electron heating source. Since resonant scatter of sunlight by N_2^+ ions lifted above the shadow height by temperature-enhanced ambipolar diffusion can account for up to approximately 10 R of artificial 427.8 nm wavelength column emission rates (and in some cases almost 20 R), or about 50% of the greatest apparent surface brightness measured at that wavelength, a suprathermal electron production source that accelerates or produces approximately 1300 electrons per second per cubic centimeter with 20 eV energy is sufficient to produce the additional airglow enhancements to bring agreement between the modeled column emission rate and the measured apparent surface brightness. Suprathermal electrons accelerated to lesser energies produced at a comparable but perhaps somewhat higher rate are also likely to produce the observed 557.7 nm emissions. Thermal electron heating alone is sufficient to produce all observed column emission rates of 630.0 nm wavelength emissions.

Additional optical measurements from ground sites co-located with the HF transmitter can still potentially resolve ambiguities such as the relative importance of electron impact ionization of N_2 molecules or resonant scatter of sunlight by N_2^+ ions in artificial 427.8 nm wavelength emissions. For example, simultaneous measurements of the first negative 1-0 and Meinel 0-0 emissions are expected to remain be in proportion from impact-ionization of N_2 molecules since the respective cross-sections are not sensitive to electron energies greater than 20 eV [*Remick et al.*, 2001]. If the relative intensities of both bands remain constant before and during radio-enhanced airglow, then this provides strong evidence consistent with impact-ionization of N_2 molecules by HF-accelerated electrons. If the relative intensities of both bands vary from their

background values during radio modification, then mechanisms other than electron impact ionization must be considered.

Given the history of ionosphere radio modification research, it is likely that additional unexpected results or discoveries will result from further attempts to resolve the issues addressed in this report. At a minimum, without measurements made in situ with sounding rockets or low-altitude satellites, altitude-resolved side-view optical measurements of artificial airglow emissions combined with full ISR measurements of electron density and temperature are needed to clarify the role of HF-accelerated electrons in generating artificial aurora. As made evident in section 4.2, altitude-resolved measurements of artificial airglow, plasma density, and plasma temperature provide key information regarding the relevant mechanisms involved. However, it is also clear that the complex spatiotemporal structure of artificial airglow emissions observed during recent experiments cannot be reproduced by current theory or models.

There are several very significant uncertainties and inconsistencies that make these results, and the results of all prior efforts to estimate energy distributions of ionosphere electrons accelerated by the interaction of powerful HF electromagnetic waves and the ionosphere plasma, considerably speculative and should not be used to reject alternate hypotheses that do not rely on HF-electron heating or acceleration. Particular observations where theory and measurements do not agree: temporal variation in airglow intensity and emission altitude. For example, calculated green line intensities increase with decreasing altitude while red line intensities decrease with decreasing altitude, yet neither of these effects are evident even in reported experiments where the HF-plasma interaction source (as indicated by ion- and plasma-line radar measurements) was seen with radar to descend by 50 km or more. Finally, recent experiments have shown unexpected sensitivity of the interaction region descent to small variations of pump frequency to the electron gyroharmonics [*Watkins et al.*, 2013; 2014a; b]. Not only is this phenomenon poorly understood, but no theory can currently account for the asymmetric effects observed from using pump frequencies slightly above versus slightly below each gyroharmonic. Comparable experiments testing the sensitivity of artificial airglow intensity to comparable variations in pump frequency have not yet been performed.

5.0 CONCLUSIONS

The following conclusions resulted from this research:

- Artificial airglow and plasma density enhancements reported by *Pedersen et al.* [2010] can be adequately explained by a dual-layer source of 20 eV accelerated electrons applied at 150 km and 200 km altitudes. The sources were each assumed to have thickness of 4 km.
    - The corresponding power fluxes were calculated to be 36.8 nW/cm^2 at 150 km and 13.5 nW/cm^2 at 200 km altitude.
    - The corresponding accelerated 20 eV electron volume production rates were 19,000 cm^{-3} s^{-1} at 150 km and 7000 cm^{-3} s^{-1} at 200 km altitude.
    - Estimating accelerated electron energy distributions with additional precision is probably not appropriate at this time given experimental uncertainties and observed HF-plasma dynamics that are beyond modeling and observational assets that have been used to date for ionosphere radio modification experiments.
- Artificial heating of thermal electrons can cause significant enhancements of the 427.8 nm emission which has previously been assumed to result solely from impact-ionization of N_2 molecules by HF-accelerated electrons with energy greater than 20 eV.
    - The responsible mechanism is enhanced resonant scatter of sunlight by N_2^+ ions lifted above the shadow height through electron temperature-enhanced ambipolar diffusion.
    - The greatest effect was predicted to be achieved at twilight while O-mode HF pumping at a frequency near foF2.
    - Resonant scatter of sunlight can potentially account for up to 50% of previously reported artificial 427.8 nm emission intensity.
- Current theories describing ionosphere modification by HF electron heating and acceleration are not adequate to describe the spatiotemporal evolution of artificial airglow sources.
    - No current model explains the significant asymmetric sensitivity of the airglow and HF-enhanced ion and plasma line source descent altitudes to minor variations of the pump frequency above or below electron gyro-resonance frequencies.
    - Variations of artificial airglow intensity at 427.8, 537.7, and 630.0 nm wavelengths with artificial airglow source altitude variations, predicted with standard model calculations of artificial electron heating or electron acceleration effects, do not agree well with measurements.
    - Reports of artificial airglow describe both artificial airglow that is localized within approximately 10 km of the source regions and airglow that extends hundreds of kilometers along the geomagnetic field from the source region but current theories cannot explain why one structure occurs rather than the other for any particular experiment.

6.0 PUBLICATIONS

1. Fallen, C. T., and B. J. Watkins (2015), Altitude-power simulations of enhanced 427.8 nm wavelength airglow observed during ionosphere HF-modification experiments at HAARP and EISCAT, paper presented at CEDAR Workshop 2015, Seattle, Washington, 24 June 2015.

2. Fallen, C. T. (2015), The artificial blue 427.8 nm aurora: an indicator of enhanced N2+ ion densities but not necessarily of enhanced impact ionization, edited.

3. Hysell, D. L., M. J. McCarrick, C. T. Fallen, and J. Vierinen (2015), First artificial periodic inhomogeneity experiments at HAARP, *Geophys. Res. Lett.*, 2015GL063064.

4. Fallen, C. T., W. A. Bristow, M. J. Nicolls, and R. A. Viereck (2014), Forecasting the Ionosphere Response to Solar Flares from Satellite Measurements of X-ray and EUV Flux, *AGU Fall Meeting Abstracts*, *13*, 3974.

5. Watkins, B. J., C. T. Fallen, and J. A. Secan (2014), Large-Scale Ionospheric Effects Related to Electron-Gyro Harmonics: What We Have Learned from HAARP, *AGU Fall Meeting Abstracts*, *32*, 03.

6. Fallen, C. T. (2014), Radio-wave interactions with the ionosphere: Understanding the physics of artificial plasma ionization and airglow at HAARP, presented at *Air Force Office of Scientific Research (AFOSR) Young Investigator Program (YIP) Meeting 2014*, Washington, D. C., 24-25 June 2014.

7. Fallen, C. T., W. A. Bristow, and M. J. Nicolls (2014), Observations and simulations of the Poker Flat, Alaska ionosphere response to the X4.9 Solar Flare on 25 Feb 2014, paper presented at CEDAR Workshop 2014, Seattle, Washington, 22-26 June 2013.

8. Fallen, C. T., and B. J. Watkins (2014), Calculations of 4278 Å artificial auroral airglow emissions resulting from powerful HF radio transmissions, paper presented at Radio Science Meeting (USNC-URSI NRSM), 2014 US National Committee of URSI National, 8-11 Jan. 2014.

9. Watkins, B. J., C. T. Fallen, and J. A. Secan (2014), UHF Radar observations at HAARP with HF pump frequencies near electron gyro-harmonics and associated ionospheric effects, presented at *COMMITTEE ON SPACE RESEARCH (COSPAR) SCIENTIFIC ASSEMBLY 2014*, Moscow, Russia, 7 August 2014.

10. Fallen, C. T., and B. J. Watkins (2013), HF-enhanced 4278-Å airglow: evidence of accelerated ionosphere electrons?, *AGU Fall Meeting Abstracts*, *23*, 07.

11. Watkins, B. J., C. T. Fallen, and J. A. Secan (2013), Artificial Ionization and UHF Radar Response Associated with HF Frequencies near Electron Gyro-Harmonics (Invited), *AGU Fall Meeting Abstracts*, *23*, 02.

12. Fallen, C. T. (2013), RFII tutorial: Ionosphere Modeling Techniques, Part 1, presented at *RF Ionosphere Interactions Workshop*, Arecibo Observatory, Arecibo, Puerto Rico, USA, April 2013.

13. Fallen, C. T., and B. J. Watkins (2013), Electron heat flux calculations associated with auroral precipitation events, paper presented at *CEDAR Workshop 2013*, Boulder, Colorado, 23 June 2013.

14. Fallen, C. T. (2013), Calculations of low-intensity auroral electron flux over Poker Flat, Alaska during PINOT 2012, presented at *CEDAR Workshop 2013*, Boulder, Colorado, USA, 22-28 June 2013.

15. Fallen, C. T., and B. J. Watkins (2013), Airglow enhancements from electron heating calculated with a self-consistent ionosphere model, paper presented at *RF Ionospheric Interactions Workshop*, Arecibo Observatory, Arecibo, Puerto Rico, USA, 21-24 April 2013.

16. Watkins, B. J., and C. T. Fallen (2013), UHF Radar Scattering of HF-Enhanced Plasma Waves: HF Frequency Dependence Near the Fourth Electron Gyro-Harmonic, presented at *RF Ionospheric Interactions Workshop*, Arecibo, Puerto Rico, 21-24 April 2013.

17. Watkins, B. J., C. T. Fallen, and M. J. McCarrick (2013), UHF Radar Scattering of HF-Enhanced Plasma Waves: First Results for UP-DOWN HF Power Ramp Experiments, presented at *RF Ionospheric Interactions Workshop*, Arecibo, Puerto Rico, 21-24 April 2013.

18. Fallen, C. T., and B. J. Watkins (2013), Diurnal and seasonal variation of electron heat flux measured with the Poker Flat Incoherent-Scatter Radar, *Journal of Geophysical Research: Space Physics, 118*(8), doi:10.1002/jgra.50485.

19. Watkins, B. J., and C. T. Fallen (2013), Spectral characteristics of HF-enhanced ion-line signals detected during the initial response and extended heating phase at the HAARP facility, presented at *URSI National Radio Science Meeting (January 2013)*, Boulder, Colorado.

7.0 REFERENCES

Baker, D. J. (1974), Rayleigh, the Unit for Light Radiance, *Applied Optics*, *13*(9), 2160-2163.

Baker, D. J., and G. J. Romick (1976), The Rayleigh: interpretation of the unit in terms of column emission rate or apparent radiance expressed in SI units, *Applied Optics*, *15*(8), 1966-1968.

Bernhardt, P., C. Tepley, and L. Duncan (1989), Airglow enhancements associated with plasma cavities formed during ionospheric heating experiments, *J. Geophys. Res.*, *94*(A7), 9071-9092.

Bernhardt, P. A., L. M. Duncan, and C. A. Tepley (1988), Artificial Airglow Excited by High-Power Radio Waves, *Science*, *242*(4881), 1022-1022.

Bilitza, D., and B. W. Reinisch (2008), International Reference Ionosphere 2007: Improvements and new parameters, *Adv. Space Res.*, *42*(4), 1845-1950.

Broadfoot, A. L. (1967), Resonance scattering by N2+, *Planet. Space Sci., 15*(12), 1801-1815, doi: 10.1016/0032-0633(67)90017-7.

Broadfoot, A. L., and D. M. Hunten (1966), N2+ emission in the twilight, *Planet. Space Sci., 14*(12), 1303-1319, doi: 10.1016/0032-0633(66)90083-3.

Carlson, H. C., V. B. Wickwar, and G. P. Mantas (1982), Observations of fluxes of suprathermal electrons accelerated by HF excited instabilities, *J. Atmos. Terr. Phys., 44*(12), 1089-1100, doi: 10.1016/0021-9169(82)90020-4.

Chamberlain, J. W. (Ed.) (1961), *Physics of the aurora and airglow*, Academic Press, Royal Belgian Meteorological Institute, Uccle, Belgium.

Chamberlain, J. W. (1995), Auroral Spectroscopy and Photometry, in *Physics of the Aurora and Airglow*, edited, pp. 151-216, American Geophysical Union.

Drob, D. P., et al. (2008), An empirical model of the Earth's horizontal wind fields: HWM07, *J. Geophys. Res.*, *113*(A12), A12304.

Evans, W. F. J., E. J. Llewellyn, J. C. Haslett, and L. R. Megill (1970), Preliminary Results from the 1.27-Micron Measurements in the Boulder Ionospheric Modification Experiment, *J. Geophys. Res.*, *75*(31), 6425-6428.

Fallen, C. T. (2010), Applications of a time-dependent polar ionosphere model for radio modification experiments, Ph.D. thesis, 213 pp, Univ. of Alaska Fairbanks, Fairbanks, Alaska.

Fallen, C. T. (2013), Calculations of low-intensity auroral electron flux over Poker Flat, Alaska during PINOT 2012, in *CEDAR Workshop 2013*, edited, Boulder, Colorado, USA.

Fallen, C. T., and B. J. Watkins (2010), Time variations of the HF-enhanced ion-line and airglow emission altitudes, in *RF Ionosphere Interactions Workshop*, edited, Sante Fe, New Mexico.

Fallen, C. T., and B. J. Watkins (2013a), Airglow enhancements from electron heating calculated with a self-consistent ionosphere model, paper presented at RF Ionospheric Interactions Workshop, Arecibo Observatory, Arecibo, Puerto Rico, USA, 21-24 April 2013.

Fallen, C. T., and B. J. Watkins (2013b), Diurnal and seasonal variation of electron heat flux measured with the Poker Flat Incoherent-Scatter Radar, *Journal of Geophysical Research: Space Physics, 118*(8), 5327-5332, doi: 10.1002/jgra.50485.

Fallen, C. T., and B. J. Watkins (2013c), Electron heat flux calculations associated with auroral precipitation events, paper presented at CEDAR Workshop 2013, Boulder, Colorado, 23 June 2013.

Fallen, C. T., and B. J. Watkins (2013d), HF-enhanced 4278-Å airglow: evidence of accelerated ionosphere electrons?, *AGU Fall Meeting Abstracts*, *23*, 07.

Fallen, C. T., and B. J. Watkins (2014), Calculations of 4278 Å artificial auroral airglow emissions resulting from powerful HF radio transmissions, paper presented at Radio Science Meeting (USNC-URSI NRSM), 2014 US National Committee of URSI National, 8-11 Jan. 2014.

Fallen, C. T., J. A. Secan, and B. J. Watkins (2011), In-situ measurements of topside ionosphere electron density enhancements during an HF-modification experiment, *Geophys. Res. Lett., 38*(8), L08101, doi: 10.1029/2011gl046887.

Gurevich, A. V., Y. S. Dimant, G. M. Milikh, and V. V. Vas'kov (1985), Multiple acceleration of electrons in the regions of high-power radio-wave reflection in the ionosphere, *J. Atmos. Terr. Phys., 47*(11), 1057-1070, doi: 10.1016/0021-9169(85)90023-6.

Gustavsson, B., T. B. Leyser, M. Kosch, M. T. Rietveld, A. Steen, B. U. E. Brandstrom, and T. Aso (2006), Electron gyroharmonic effects in ionization and electron acceleration during High-Frequency pumping in the ionosphere, *Phys. Rev. Lett.*, *97*(19), 195002-195004.

Gustavsson, B., B. U. E. Brandstrom, A. Steen, T. Sergienko, T. B. Leyser, M. T. Rietveld, T. Aso, and M. Ejiri (2002), Nearly simultaneous images of HF-pump enhanced airglow at 6300 Å and 5577 Å, *Geophys. Res. Lett.*, *29*(24), 2220.

Gustavsson, B., et al. (2001), First tomographic estimate of volume distribution of HF-pump enhanced airglow emission, *J. Geophys. Res., 106*(A12), 29105-29123, doi: 10.1029/2000JA900167.

Gustavsson, B., et al. (2005), The electron energy distribution during HF pumping, a picture painted with all colors, *Ann. Geophys., 23*, 1747-1754, doi: 10.5194/angeo-23-1747-2005.

Haslett, J. C., and L. R. Megill (1974), A model of the enhanced airglow excited by RF radiation, *Radio Sci.*, *9*(11), 1005-1019.

Henriksen, K. (1984), N2+ emissions in sunlit cusp and night-side aurora, *Ann. Geophys.*, *2*(4), 457-462.

Holma, H., K. U. Kaila, M. J. Kosch, and M. T. Rietveld (2006), Recognizing the blue emission in artificial aurora, *Adv. Space Res.*, *38*(11), 2653-2658.

Huba, J., G. Joyce, and J. Fedder (2000), Sami2 is Another Model of the Ionosphere (SAMI2): A new low-latitude ionosphere model, *J. Geophys. Res., 105*(A10), 23035-23053, doi: 10.1029/2000JA000035.

Hysell, D. L., R. H. Varney, M. N. Vlasov, E. Nossa, B. Watkins, T. Pedersen, and J. D. Huba (2012), Estimating the electron energy distribution during ionospheric modification from spectrographic airglow measurements, *Journal of Geophysical Research: Space Physics, 117*(A2), doi: 10.1029/2011JA017187.

Hysell, D. L., R. J. Miceli, E. A. Kendall, N. M. Schlatter, R. H. Varney, B. J. Watkins, T. R. Pedersen, P. A. Bernhardt, and J. D. Huba (2014), Heater-induced ionization inferred from spectrometric airglow measurements, *Journal of Geophysical Research: Space Physics*, *119*(3), 2038-2045.

Kendall, E., R. Marshall, R. T. Parris, A. Bhatt, A. Coster, T. Pedersen, P. Bernhardt, and C. Selcher (2010), Decameter structure in heater-induced airglow at the High frequency Active Auroral Research Program facility, *Journal of Geophysical Research: Space Physics, 115*(A8), doi: 10.1029/2009JA015043.

Kosch, M. J., T. Pedersen, E. Mishin, M. Starks, E. Gerken-Kendall, D. Sentman, S. Oyama, and B. Watkins (2007), Temporal evolution of pump beam self-focusing at the High-Frequency Active Auroral Research Program, *J. Geophys. Res.*, *112*(A8), 1-9.

Min, Q.-L. (1993), A self-consistent time varying auroral model, Ph.D. thesis, University of Alaska, Fairbanks.

Mishin, E., and T. Pedersen (2011), Ionizing wave via high-power HF acceleration, *Geophys. Res. Lett., 38*(1), L01105, doi: 10.1029/2010gl046045.

Nagy, A., and P. Banks (1970), Photoelectron fluxes in the ionosphere, *J. Geophys. Res.*, *75*(31), 6260-6270.

Pedersen, T., B. Gustavsson, E. Mishin, E. Kendall, T. Mills, H. C. Carlson, and A. L. Snyder (2010), Creation of artificial ionospheric layers using high-power HF waves, *Geophys. Res. Lett., 37*(2), L02106, doi: 10.1029/2009gl041895.

Picone, J. M., A. E. Hedin, D. P. Drob, and A. C. Aikin (2002), NRLMSISE-00 empirical model of the atmosphere: Statistical comparisons and scientific issues, *J. Geophys. Res., 107*(A12), doi: 10.1029/2002JA009430.

Rees, M. H. (1989), *Physics and Chemistry of the Upper Atmosphere*, Cambridge Univ. Press, New York.

Rees, M. H., and D. Luckey (1974), Auroral Electron Energy Derived From Ratio of Spectroscopic Emissions, 1. Model Computations, *J. Geophys. Res.*, *79*(34), 5181-5186.

Rees, M. H., and D. Lummerzheim (1989), Characteristics of Auroral Electron Precipitation Derived from Optical Spectroscopy, *J. Geophys. Res.*, *94*(A6), 6799-6815.

Rees, M. H., D. Lummerzheim, R. G. Roble, J. D. Winningham, J. D. Craven, and L. A. Frank (1988), Auroral Energy Deposition Rate, Characteristic Electron Energy, and Ionospheric Parameters Derived From Dynamics Explorer 1 Images, *J. Geophys. Res.*, *93*.

Remick, K. J., R. W. Smith, and D. Lummerzheim (2001), The significance of resonant scatter in the measurement of N2+ first negative 0–1 emissions during auroral activity, *J. Atmos. Solar Terr. Phys., 63*(4), 295-308, doi: 10.1016/S1364-6826(00)00233-9.

Richards, P. G., J. A. Fennelly, and D. G. Torr (1994), EUVAC: A solar EUV flux model for aeronomic calculations, *J. Geophys. Res., 99*(A5), doi: 10.1029/94ja00518.

Rietveld, M. T., M. J. Kosch, N. F. Blagoveshchenskaya, V. A. Kornienko, T. Leyser, and T. K. Yeoman (2003), Ionospheric electron heating, optical emissions, and striations induced by powerful HF radio waves at high latitudes: Aspect angle dependence, *J. Geophys. Res., 108*(A4), doi: 10.1029/2002JA009543.

Robinson, R. M., S. B. Mende, R. R. Vondrak, J. U. Kozyra, and A. F. Nagy (1985), Radar and Photometric Measurements of an Intense Type A Red Aurora, *J. Geophys. Res.*, *90*(A1), 457-466.

Thomas, R. J. (1981), Analyses of atomic oxygen, the Green Line, and Herzberg Bands in the lower thermosphere, *Journal of Geophysical Research: Space Physics, 86*(A1), 206-210, doi: 10.1029/JA086iA01p00206.

Utlaut, W. F. (1970), An Ionospheric Modification Experiment Using Very High Power, High Frequency Transmission, *J. Geophys. Res.*, *75*(31), 6402-6405.

Varney, R. H., W. E. Swartz, D. L. Hysell, and J. D. Huba (2012), SAMI2-PE: A model of the ionosphere including multistream interhemispheric photoelectron transport, *J. Geophys. Res., 117*(A6), A06322, doi: 10.1029/2011ja017280.

Watkins, B. J., C. T. Fallen, and J. A. Secan (2013), Artificial Ionization and UHF Radar Response Associated with HF Frequencies near Electron Gyro-Harmonics (Invited), *AGU Fall Meeting Abstracts*, *23*, 02.

Watkins, B. J., C. T. Fallen, and J. A. Secan (2014a), Large-Scale Ionospheric Effects Related to Electron-Gyro Harmonics: What We Have Learned from HAARP, *AGU Fall Meeting Abstracts*, *32*, 03.

Watkins, B. J., C. T. Fallen, and J. A. Secan (2014b), UHF Radar observations at HAARP with HF pump frequencies near electron gyro-harmonics and associated ionospheric effects, in *COMMITTEE ON SPACE RESEARCH (COSPAR) SCIENTIFIC ASSEMBLY 2014*, edited, Moscow, Russia.

THIS PAGE INTENTIONALLY LEFT BLANK

1.

1. Report Type

Final Report

Primary Contact E-mail
Contact email if there is a problem with the report.

ctfallen@alaska.edu

Primary Contact Phone Number
Contact phone number if there is a problem with the report

907-450-8687

Organization / Institution name

University of Alaska Fairbanks

Grant/Contract Title
The full title of the funded effort.

Determining energy distributions of HF-accelerated electrons at HAARP

Grant/Contract Number
AFOSR assigned control number. It must begin with "FA9550" or "F49620" or "FA2386".

FA9550-12-1-0424

Principal Investigator Name
The full name of the principal investigator on the grant or contract.

Christopher Thomas Fallen

Program Manager
The AFOSR Program Manager currently assigned to the award

Kent Miller

Reporting Period Start Date

8/15/2012

Reporting Period End Date

8/14/2015

Abstract

The main objective of this project was to determine the energy distribution of ionosphere suprathermal electrons accelerated by powerful high frequency (HF) electromagnetic waves transmitted from the High-frequency Active Auroral Research Program (HAARP) facility in Gakona, Alaska. Available measurements from ground-based instruments include optical imager measurements of artificial airglow brightness at various wavelengths and radar measurements of plasma density. The main methods of estimating energetic electron events in the ionosphere are inversion techniques that use physics-based ionosphere models to calculate simulated ionosphere responses to parameterizations of accelerated electron sources. Simulation results are then matched against measurements to find the set of simulation input parameters that optimize agreement with measurements. These techniques can vary from rigorous mathematical solutions to ad hoc qualitative comparisons. This research used the latter approach. The accuracy of results from both approaches is limited by relatively sparse measurements and incomplete understanding of ionosphere physics. Descriptions of the measurements and model are provided to aid with interpreting the main results.

For a given fixed HF-plasma interaction altitude, results from this research show that a dual source of 20 eV electrons applied at 150 km and 200 km altitudes is sufficient to reproduce substantial airglow and plasma

density enhancements created above HAARP during March, 2009. These were among the brightest and most exceptional radio-induced airglow and plasma events ever observed. A new discovery resulting from this project is that significant artificial 427.8 nm wavelength airglow can result from thermal heating of the ionosphere plasma and hence is not necessarily an indicator of energetic electrons accelerated to energies exceeding 20 eV as previously assumed. Still, there are several unresolved science issues regarding the spatiotemporal evolution of HF-enhanced airglow and ionization structures. In particular, the apparent sensitive dependence of the artificial airglow and plasma structures on pump frequency relative to nearby electron gyroharmonic frequencies cannot yet be explained. Finally, the expected dependence on relative intensities of the airglow emission lines on emission altitude has not yet been apparent in measurements.

Distribution Statement

This is block 12 on the SF298 form.

Distribution A - Approved for Public Release

Explanation for Distribution Statement

If this is not approved for public release, please provide a short explanation. E.g., contains proprietary information.

SF298 Form

Please attach your SF298 form. A blank SF298 can be found here. Please do not password protect or secure the PDF The maximum file size for an SF298 is 50MB.

AFD-070820-035 - Fallen - AFOSR 2015 - FINAL 01.pdf

Upload the Report Document. File must be a PDF. Please do not password protect or secure the PDF . The maximum file size for the Report Document is 50MB.

AFOSR - FA9550-12-1-0424 - YIP - Final Performance Report - Chris Fallen - Print 20151112.pdf

Upload a Report Document, if any. The maximum file size for the Report Document is 50MB.

Archival Publications (published) during reporting period:

1. Fallen, C. T., and B. J. Watkins (2015), Altitude-power simulations of enhanced 427.8 nm wavelength airglow observed during ionosphere HF-modification experiments at HAARP and EISCAT, paper presented at CEDAR Workshop 2015, Seattle, Washington, 24 June 2015.
2. Fallen, C. T. (2015), The artificial blue 427.8 nm aurora: an indicator of enhanced N2+ ion densities but not necessarily of enhanced impact ionization, edited.
3. Hysell, D. L., M. J. McCarrick, C. T. Fallen, and J. Vierinen (2015), First artificial periodic inhomogeneity experiments at HAARP, Geophys. Res. Lett., 2015GL063064.
4. Fallen, C. T., W. A. Bristow, M. J. Nicolls, and R. A. Viereck (2014), Forecasting the Ionosphere Response to Solar Flares from Satellite Measurements of X-ray and EUV Flux, AGU Fall Meeting Abstracts, 13, 3974.
5. Watkins, B. J., C. T. Fallen, and J. A. Secan (2014), Large-Scale Ionospheric Effects Related to Electron-Gyro Harmonics: What We Have Learned from HAARP, AGU Fall Meeting Abstracts, 32, 03.
6. Fallen, C. T. (2014), Radio-wave interactions with the ionosphere: Understanding the physics of artificial plasma ionization and airglow at HAARP, presented at Air Force Office of Scientific Research (AFOSR) Young Investigator Program (YIP) Meeting 2014, Washington, D. C., 24-25 June 2014.
7. Fallen, C. T., W. A. Bristow, and M. J. Nicolls (2014), Observations and simulations of the Poker Flat, Alaska ionosphere response to the X4.9 Solar Flare on 25 Feb 2014, paper presented at CEDAR Workshop 2014, Seattle, Washington, 22-26 June 2013.
8. Fallen, C. T., and B. J. Watkins (2014), Calculations of 4278 Å artificial auroral airglow emissions resulting from powerful HF radio transmissions, paper presented at Radio Science Meeting (USNC-URSI NRSM), 2014 US National Committee of URSI National, 8-11 Jan. 2014.
9. Watkins, B. J., C. T. Fallen, and J. A. Secan (2014), UHF Radar observations at HAARP with HF pump frequencies near electron gyro-harmonics and associated ionospheric effects, presented at COMMITTEE ON SPACE RESEARCH (COSPAR) SCIENTIFIC ASSEMBLY 2014, Moscow, Russia, 7 August 2014.
10. Fallen, C. T., and B. J. Watkins (2013), HF-enhanced 4278-Å airglow: evidence of accelerated ionosphere electrons?, AGU Fall Meeting Abstracts, 23, 07.
11. Watkins, B. J., C. T. Fallen, and J. A. Secan (2013), Artificial Ionization and UHF Radar Response

Associated with HF Frequencies near Electron Gyro-Harmonics (Invited), AGU Fall Meeting Abstracts, 23, 02.
12. Fallen, C. T. (2013), RFII tutorial: Ionosphere Modeling Techniques, Part 1, presented at RF Ionosphere Interactions Workshop, Arecibo Observatory, Arecibo, Puerto Rico, USA, April 2013.
13. Fallen, C. T., and B. J. Watkins (2013), Electron heat flux calculations associated with auroral precipitation events, paper presented at CEDAR Workshop 2013, Boulder, Colorado, 23 June 2013.
14. Fallen, C. T. (2013), Calculations of low-intensity auroral electron flux over Poker Flat, Alaska during PINOT 2012, presented at CEDAR Workshop 2013, Boulder, Colorado, USA, 22-28 June 2013.
15. Fallen, C. T., and B. J. Watkins (2013), Airglow enhancements from electron heating calculated with a self-consistent ionosphere model, paper presented at RF Ionospheric Interactions Workshop, Arecibo Observatory, Arecibo, Puerto Rico, USA, 21-24 April 2013.
16. Watkins, B. J., and C. T. Fallen (2013), UHF Radar Scattering of HF-Enhanced Plasma Waves: HF Frequency Dependence Near the Fourth Electron Gyro-Harmonic, presented at RF Ionospheric Interactions Workshop, Arecibo, Puerto Rico, 21-24 April 2013.
17. Watkins, B. J., C. T. Fallen, and M. J. McCarrick (2013), UHF Radar Scattering of HF-Enhanced Plasma Waves: First Results for UP-DOWN HF Power Ramp Experiments, presented at RF Ionospheric Interactions Workshop, Arecibo, Puerto Rico, 21-24 April 2013.
18. Fallen, C. T., and B. J. Watkins (2013), Diurnal and seasonal variation of electron heat flux measured with the Poker Flat Incoherent-Scatter Radar, Journal of Geophysical Research: Space Physics, 118(8), doi:10.1002/jgra.50485.
19. Watkins, B. J., and C. T. Fallen (2013), Spectral characteristics of HF-enhanced ion-line signals detected during the initial response and extended heating phase at the HAARP facility, presented at URSI National Radio Science Meeting (January 2013), Boulder, Colorado.

Changes in research objectives (if any):

N/A

Change in AFOSR Program Manager, if any:

Dr. Cassandra Fesen was the original AFOSR Program Manager.
Dr. Kent Miller was the AFOSR Program Manager at the reporting period end date.

Extensions granted or milestones slipped, if any:

N/A

AFOSR LRIR Number

LRIR Title

Reporting Period

Laboratory Task Manager

Program Officer

Research Objectives

Technical Summary

Funding Summary by Cost Category (by FY, $K)

	Starting FY	FY+1	FY+2
Salary			
Equipment/Facilities			
Supplies			
Total			

Report Document

Report Document - Text Analysis

Report Document - Text Analysis

Appendix Documents

2. Thank You

E-mail user

Nov 12, 2015 19:50:59 Success: Email Sent to: ctfallen@alaska.edu